CHALMERS

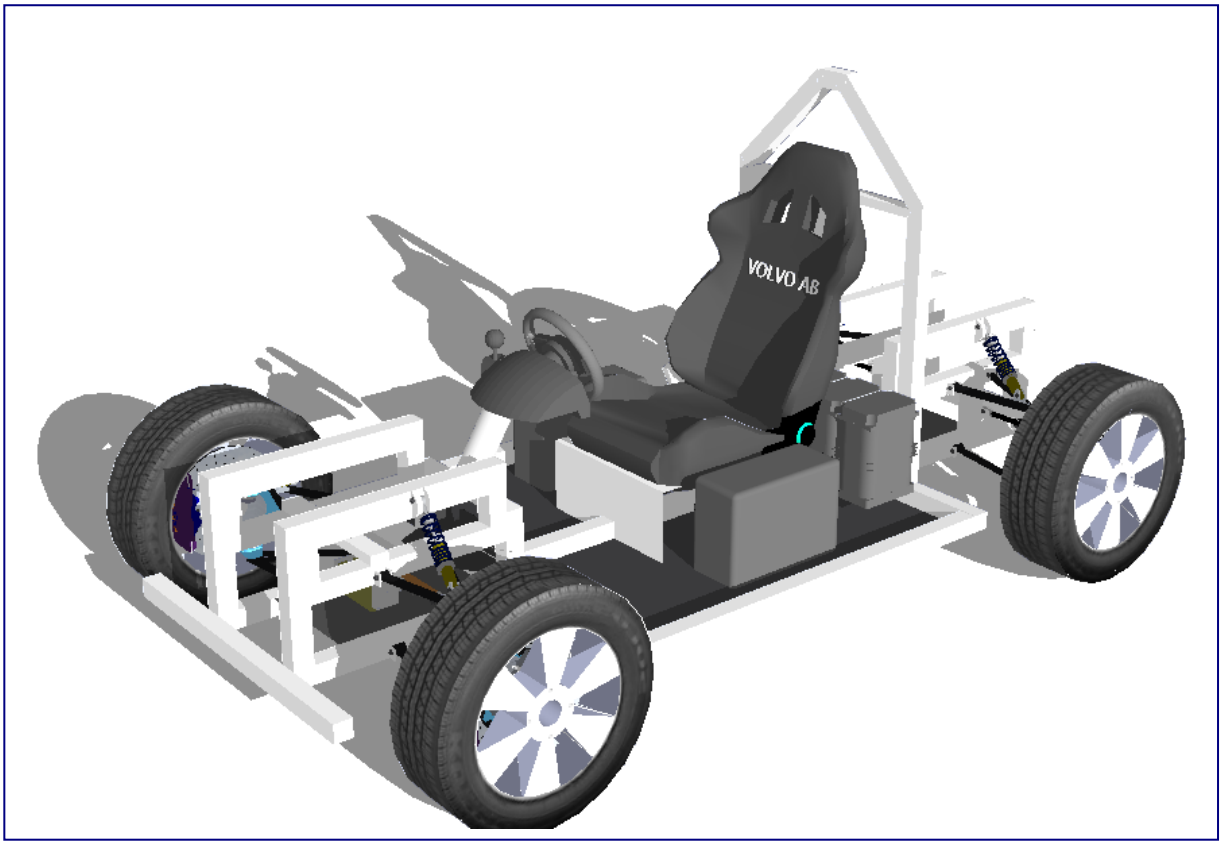

Steering actuator sizing of prototype electric one-seater

Master's Thesis

GREGOR WERUM

Department of Applied Mechanics
Division of Vehicle Engineering and Autonomous Systems
Vehicle Dynamics Research Group
CHALMERS UNIVERSITY OF TECHNOLOGY
Göteborg, Sweden 2013
Master's thesis 2013:45

MASTER'S THESIS

Steering actuator sizing of prototype electric one-seater

GREGOR WERUM

Department of Applied Mechanics
Division of Vehicle Engineering and Autonomous Systems
Vehicle Dynamics Research Group
CHALMERS UNIVERSITY OF TECHNOLOGY
Göteborg, Sweden 2013

Steering actuator sizing of prototype electric one-seater
GREGOR WERUM

Master's Thesis 2013:45
ISSN 1652-8557
Department of Applied Mechanics
Division of Vehicle Engineering and Autonomous Systems
Vehicle Dynamics Research Group
Chalmers University of Technology
SE-412 96 Göteborg
Sweden
Telephone: + 46 (0)31-772 1000

Commissioned by: Volvo Group Advanced Technology & Research
Department of Mechatronics and Software, BF40760
CTP, Volvo Group Trucks Technology
SE-412 88 Göteborg
Sweden

Cover:
CAD drawing of EDV proposed on June 2013

Chalmers Reproservice / Department of Applied Mechanics
Göteborg, Sweden 2013

Steering actuator sizing of prototype electric one-seater
Master's Thesis
GREGOR WERUM
Department of Applied Mechanics
Division of Vehicle Engineering and Autonomous Systems
Vehicle Dynamics Research Group
Chalmers University of Technology

ABSTRACT

This work describes the setting of power requirements of the steering actuator for an electric demonstration vehicle (EDV). The EDV is a small one-seater vehicle with mass of approximately ~ 400 kg and is equipped with a steer-by-wire system. The dimensioning of steering systems components other than the steering actuator is not discussed in this report.

An analytic method has been developed to estimate maximum expected steering torque in creep and high speed scenarios. Furthermore, the model allows the prediction of suspension geometry influence on steering torque amplitude.

The steering effort is analyzed by means of maximum expected tire forces, which are estimated by a simple physical tire model. In the tire model maximum tire-to-ground friction is estimated for various driving scenarios considering the physical limits of the tires. This approach allows the analysis to be performed independent of vehicle motion and without a detailed dynamic car model.

The general design of the steer-by-wire system and a steering control setup is presented in order to evaluate the proposed steering system with respect to control time and precision. This is accomplished for a given actuator setup.

As major outcome of this work the overall power requirements - such as torque, speed, power and energy demand - of the steering actuator are presented. The rough actuator requirements have been identified with $F_{m,max} = 5\,kN$, $v_{m,max} = 240\,mm/s$ and $P_{m,max} = 1.2\,kW$ for a linear actuator placed on the steering rack. This is equivalent to $T_{m,max} = 50\,Nm$, $\omega_{m,max} = 230\,rpm$ and $P_{m,max} = 1.2\,kW$ for a rotary actor with steering ratio $r_s = 11$.

Key words: Steering actuator, Steer-by-wire, Tire model, Suspension geometry model, Steering control

Dimensionering av styraktuator för elektriskt prototypfordon
Examensarbete
GREGOR WERUM
Institutionen för tillämpad mekanik
Avdelningen för fordonsteknik och autonoma system
Forskargruppen fordonsdynamik
Chalmers tekniska högskola

Contents

Preface

The work for this master thesis study has been carried out at Volvo Group Truck Technology (GTT) in the period from February till June 2013. As a part of the project of developing an Electric Demonstration Vehicle (EDV) within the department for Mechatronics and Software the studies for sizing the steering actuator have been accomplished within that department.

Academic supervisor for this work have been Prof. Bengt Jacobson and Kristoffer Tagesson, Phd Student in Active Steering at Volvo GTT. Working supervisor within the department at Volvo GTT has been Dr. Jonas Hellgren, Hybrid power system engineer.

My thanks go to all three of them for their helpful input and constructive feedback.

Göteborg June 2013

Gregor Werum

Notations

Abbreviations

ATV	all-terrain vehicle
DOF	degree of freedom
EDV	electric demonstration vehicle
EOM	equation of motion
CG	center of gravity
CS	coordinate system
SbW	Steer-by-wire

Roman upper case letters

$C_{F\alpha}$	cornering stiffness (side slip angle coefficient)
$C_{F\gamma}$	cornering stiffness (camber angle coefficient)
F_{st}	overall steering rack force
F_X	longitudinal wheel force
F_Y	lateral wheel force
F_Z	vertical wheel force
I_x, I_y, I_z	vehicle area moment of inertia around x-,y- and z-axis
$I_{xz}, I_{xy}, I_{yx}, etc.$	vehicle area moment of inertia for different rotating axis
M_X	overturning moment (wheel)
M_Y	rolling resistance moment (wheel)
M_Z	self-aligning torque (wheel)
M_φ	rolling moment
X_E, Y_E, Z_E	coordinates of earth-fixed CS
X_V, Y_V, Z_V	coordinates of vehicle-fixed CS
X_W, Y_W, Z_W	coordinates of wheel-fixed CS

Roman lower case letters

a_x	longitudinal acceleration
a_y	lateral acceleration
a_z	vertical acceleration
c_b	stiffness coefficient body
c_w	stiffness coefficient wheel
c_φ	rolling stiffness
d_b	damping coefficient body
d_w	damping coefficient wheel
k_φ	rolling axis damping
m	overall vehicle mass

m_b	body mass (sprung mass) per wheel
m_w	wheel mass (unsprung mass) per wheel
u	longitudinal velocity
$-v$	lateral velocity (negative with respect to ISO vehicle coordinate dir.)
v_x	longitudinal slip velocity of tire
$-v_y$	lateral slip velocity of tire (negative with respect to ISO CS)

Greek letters

α_1	front slip angle (bicycle model)
α_2	rear slip angle (bicycle model)
α_{max}	tire slip angle at maximum alignment torque
δ	steering angle at wheel
ψ	compliance steer angle
σ	kingpin inclination angle
τ	caster angle
λ_{eff}	effective kingpin angle
γ	camber angle
φ	roll angle
r	yaw angle
ε_T	toe angle
$\varepsilon_{Br,t}$	brake support angle
$\varepsilon_{Tr,i}$	traction support angle
$\varepsilon_{B,i}^{opt}$	optimal brake support angle
$\varepsilon_{Tr,i}^{opt}$	optimal traction support angle
ω	wheel rotation speed
θ	pitching angle
θ_{roll}	roll axis inclination angle

Steering system parameters

$\overline{D_r}$	lumped damping coefficient of total steering system about actuator rotor axis $[Nm\ s/rad]$
D_r	rotor damping $[Nm\ s/rad]$
D_w	rack and tire damping about steering axis $[Nm\ s/rad]$
J_{rotor}	actuator rotor inertia $[Nm\ s^2/rad]$
J_{gear}	actuator gear box inertia (about rotor axis) $[Nm\ s^2/rad]$
J_{coup}	coupling (steering) shaft inertia $[Nm\ s^2/rad]$
J_{wheel}	wheel inertia $[Nm\ s^2/rad]$
$\overline{J_r}$	lumped inertia of total steering system about rotor axis $[Nm\ s^2/rad]$
J_r	lumped inertia of rotor, gear box and coupling shaft about rotor shaft

	$[Nm\ s^2/rad]$
$\boldsymbol{J_w}$	lumped inertia of steering rack and wheels about steering axis $[Nm\ s^2/rad]$
$\overline{\boldsymbol{K_r}}$	lumped stiffness of steering system about rotor axis$[Nm\ s/rad]$
$\boldsymbol{K_w}$	rack and tire damping about steering axis $[Nm\ s/rad]$
$\boldsymbol{T_L}$	load torque of steering actuator $Nm]$
$\boldsymbol{T_M}$	output rotor torque steering actuator (before gear transmission) $[Nm]$
$\boldsymbol{T_w}$	lumped wheel torque about kingpin axis for both front wheels $[Nm]$
$\boldsymbol{x_r}$	steering rack displacement $[m]$
$\boldsymbol{m_r}$	steering rack mass $[kg]$
$\boldsymbol{r_{st}}$	effective steering arm length $[m]$
$\boldsymbol{r_s}$	steering ratio [-]
$\boldsymbol{r_g}$	gear ratio [-]
$\boldsymbol{\theta_{hw}}$	hand-wheel angle $[rad]$
$\boldsymbol{\theta_{sens}}$	hand-wheel sensor/actuator angle $[rad]$
$\boldsymbol{\theta_r, \omega_r}$	rotor angle/rate $[rad]$/$[\ rad/s]$
$\boldsymbol{\theta_p, \omega_p}$	pinion angle/rate $[rad]$/$[\ rad/s]$
$\boldsymbol{\delta, \dot{\delta}}$	road wheel angle/rate $[rad]$/$[\ rad/s]$

Vehicle parameters

$\boldsymbol{l}$	wheel base
$\boldsymbol{a}$	distance front axis to CG
$\boldsymbol{b}$	distance rear axis to CG
$\boldsymbol{s_1, s_2}$	front and rear track width
$\boldsymbol{h_{cg}}$	center of gravity height
$\boldsymbol{h_1, h_2}$	front and rear roll center height
$\boldsymbol{h'}$	vertical distance between CG and rolling axis
$\boldsymbol{S}$	neutral steer point
$\boldsymbol{\bar{s}}$	distance from CG to neutral steer point S
$\boldsymbol{e}$	caster length/ trail, also referred to mechanical trail
$\boldsymbol{e_w}$	caster offset on wheel center height
$\boldsymbol{r_c}$	kingpin offset/ scrub radius
$\boldsymbol{r_w}$	kingpin offset on wheel center height
$\boldsymbol{t}$	pneumatic trail
$\boldsymbol{k}$	radius of gyration
$\boldsymbol{q}$	length equal to average moment arm
$[\ ]_{ss}$	subscript for steady-state
$[\ ]_{1/2}$	subscript for front/rear
$[\ ]_{l/r}$	subscript for left/right

1 Introduction

This chapter gives a short overview on motivation for this work, the approach to the problem set, the structure of the report and its most important outcomes.

1.1 Background

The motivation to this work is to support the department for Mechatronics and Software at Volvo Group Truck Technology (GTT) in building a prototype electric one-seater. This electric demonstration vehicle (EDV) serves as a platform for testing different control strategies on electric cars, such as battery management, independent rear wheel propulsion and handling control. One feature of the EDV is a steer-by-wire (SbW) system, for which adequate actuators have to be chosen. The sizing of those actuators is the major outcome of this report.

1.2 Report contributions

The aim with the models presented in this report is to provide a basis for the estimation of performance requirements on the steering actuator for a steer-by-wire system. Based on those performance requirements a suitable actuator for the EDV will be chosen. The most important outcomes for sizing the steering actuator, for both the wheel and the steering wheel actuator, are:

- Maximum, minimum and precision of actuator output torque
- Maximum angular speed
- Maximum power output
- Energy demand of actuator

The given parameters strongly depend on the chosen tires, suspension geometry and overall vehicle setup. Since the EDV is built from scratch, a variety of vehicle parameters have to be set loosely in the beginning to allow changes afterwards in a certain range. At this point of time the decision on a lot of components is not finally decided yet.

Therefore, the analysis of this report has been carried out in a more generalized way, so that results can be adapted for a change of vehicle parameters.

1.3 Vehicle parameters

This chapter states the vehicle parameters of the current setup (May 2013) of the electric demonstration vehicle (EDV). If not otherwise stated, these values are used throughout the following analysis.

Table 1: EDV geometric parameter (based on results in [1])

Parameter	**Value [unit]**
Vehicle length $\boldsymbol{l_v}$	2550 [mm]
Wheel track width $\boldsymbol{m_s}$	1300 [mm]
Wheel base $\boldsymbol{l}$	1950 [mm]
Distance front axle to CG $\boldsymbol{a}$	n/a [mm]
Distance rear axle to CG $\boldsymbol{b}$	n/a [mm]
Center of gravity height $\boldsymbol{h_{cg}}$	380 [mm]

Table 2: EDV weight parameter (based on results in [1])

Parameter	**Value [unit]**
Overall vehicle mass $\boldsymbol{m}$	300-400 [kg]
Sprung mass $\boldsymbol{m_s}$	n/a. [kg]
Unsprung mass $\boldsymbol{m_u}$	n/a [kg]
Battery weight $\boldsymbol{m_{bt}}$	n/a [kg]
Driver mass $\boldsymbol{m_d}$	80 [kg]
Weight distribution	35/65 [front/rear]

1.4 Scope

The scope of this work is to handle every aspect, which effects the power requirements of the steering actuator in a way. The analysis is done by means of suspension design, tire forces and steering system design. However, this work discusses only the effects of suspension and tire, no design proposition on those systems is presented.

A suitable steering system design and SbW control system is proposed. This steering system design focusses on the lower part of the system from steering actuator to steered wheels. No discussion on interpretation of driver steer intention and driver feedback force is included in this report.

The overall vehicle design, such as frame design, and an extensive vehicle dynamics analysis is not part of this report, since the steering force prediction in this can be understood as independent of the actual vehicle motion.

1.5 Structure of report

This section gives a short overview on the structure analysis throughout this report.

In chapter 2 the general setup of the steer-by-wire system will be introduced. The suspension setup of the EDV will be discussed and how it is modeled. Furthermore, a disturbance model is presented, which describes force transmission in unusual driving scenarios. Generally, this chapter discusses how forces act on the steering system and which parameters that influence the force transmission.

In chapter 3 the steering force amplitudes are analyzed. Four relevant driving scenarios, in which maximum steering forces are likely to occur, are identified and the tire forces are evaluated. From there, effective steering torque can be estimated using the evaluation of force lever arms from chapter 2.

In chapter 4 the setup of the steering control system is presented. The frequency and time response behavior of the steering system is analyzed for all relevant driving scenarios. From there, the actuator requirements such as torque, rotor speed, power output and energy demand are given.

Chapter 5 presents the results and overall outcomes of this work.

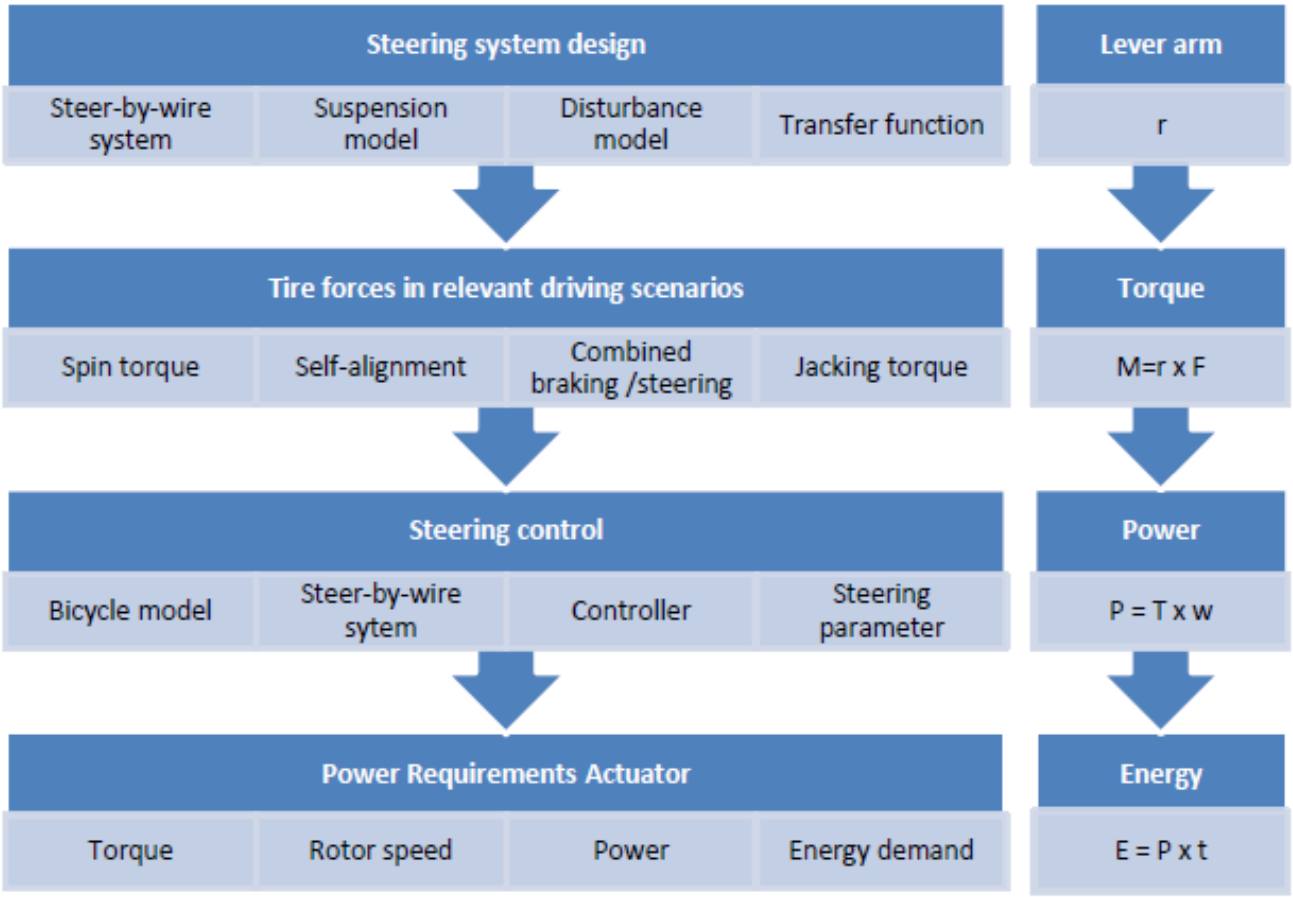

Figure 1. Analysis structure actuator sizing

Figure 1 illustrates the overall approach of the problem set. Each box represents one chapter and its subchapters. The subchapters of chapter 3 for tire forces represent each one relevant driving scenario. As can be seen on the right-hand side, the motivation for each chapter is rather straight forward, such as every chapter has one important outcome for defining the power requirements of the steering actuator.

1.6 Coordinate systems

In order to understand the outcomes of this report it is important to know which coordinate systems have been used throughout the analysis. Two coordinate systems are of major importance, the vehicle coordinate system and the wheel coordinate system , both based on SAE standards.

The vehicle chassis motion is described by six degrees of freedom (DOF) as can be seen in Figure 2: three DOF for translational motion (*jerk, push* and *lift*), such as three DOF for rotational motion (*roll, pitch* and *yaw*). The vehicle-fixed CS and its coordinates X_V, Y_V, Z_V have its origin in the COG of the car and the z-axis points upwards.

The wheel-fixed coordinate system X_W, Y_W, Z_W is shown in Figure 3 with the SAE standard tire coordinate system. Differently to the vehicle-fixed CS, it has its origin on the wheel centerline but at the contact point between tire and road with the z-axis pointing downwards. Tire torques and forces are always referred to this coordinate system.

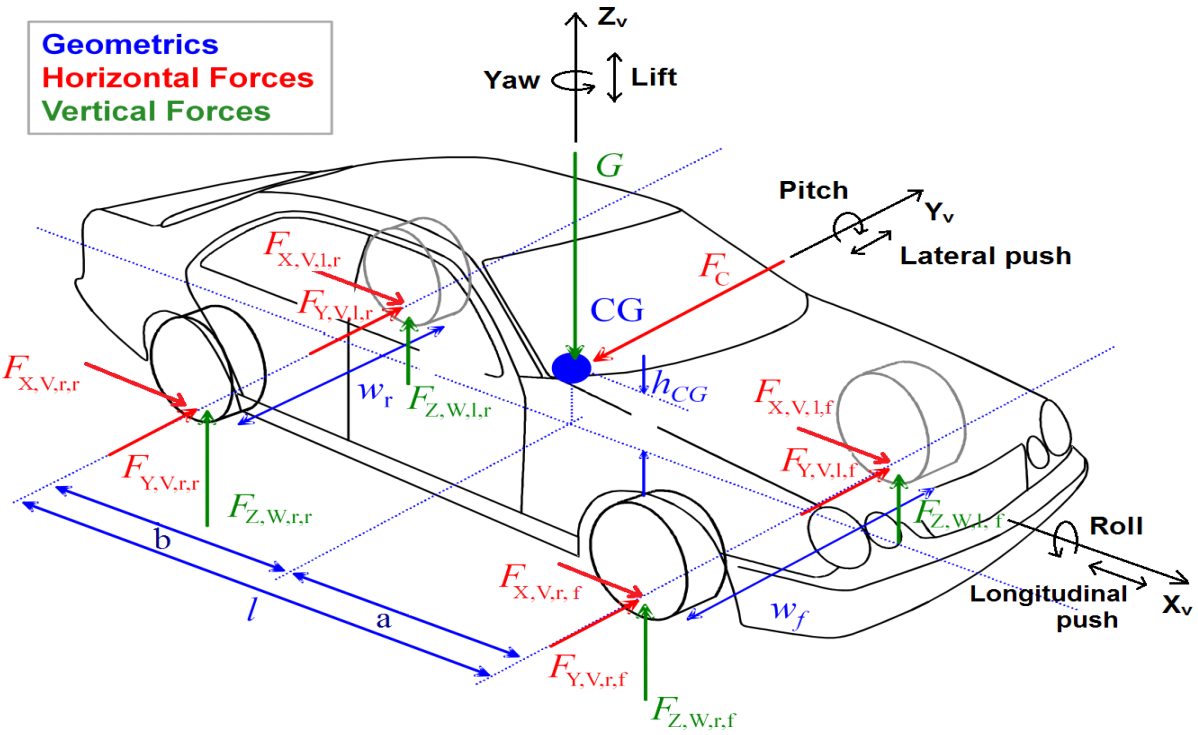

Figure 2. Vehicle forces and motion, modified from [2]

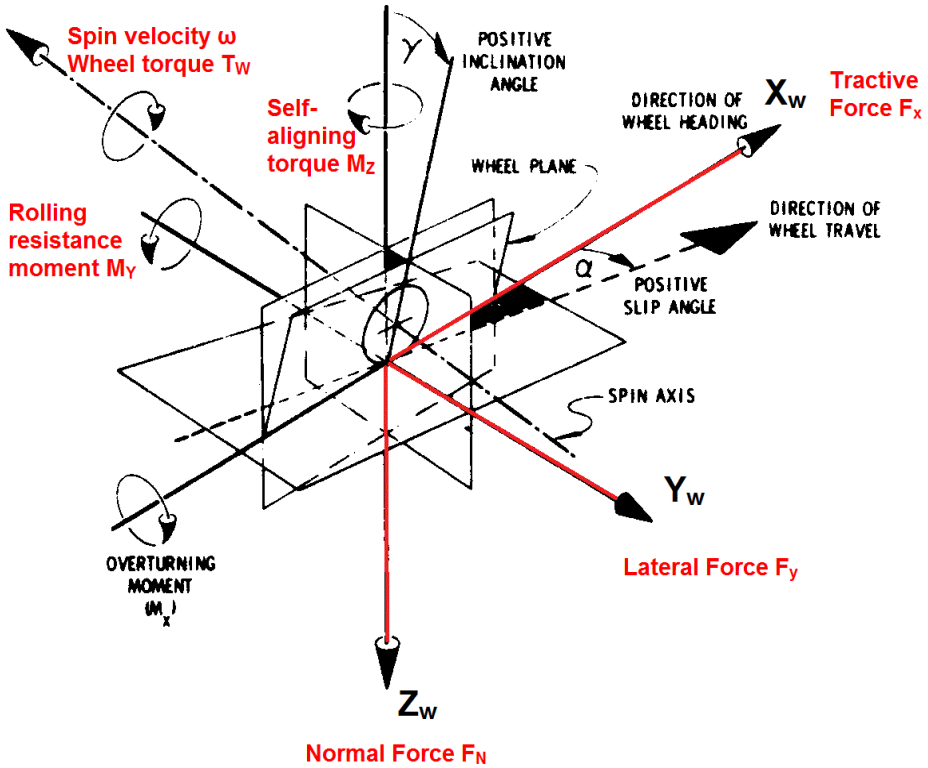

Figure 3. SAE standard tire coordinate system, modified from [3]

2 Steering system design

In this chapter the design of the overall steering system is presented. Covered is the whole system from steering shaft, steering rack, rotational-linear transmissions etc. This covers mainly research on existing systems and how they can be implemented/ adjusted to the EDV car.

Specific terms and abbreviations

$\boldsymbol{\theta_{hw}}$	handwheel angle $[rad]$
$\boldsymbol{\theta_{sens}}$	handwheel sensor/actuator angle $[rad]$
$\boldsymbol{\theta_r, \omega_r}$	rotor angle/rate $[rad]$/$[\ rad/s]$
$\boldsymbol{\theta_p, \omega_p}$	pinion angle/rate $[rad]$/$[\ rad/s]$
$\boldsymbol{\delta, \dot{\delta}}$	road wheel angle/rate $[rad]$/$[\ rad/s]$
$\boldsymbol{x_r}$	steering rack displacement $[m]$
$\boldsymbol{m_r}$	steering rack mass $[kg]$
$\boldsymbol{r_{st}}$	effective steering arm length $[m]$
$\boldsymbol{r_s}$	steering ratio [-]
$\boldsymbol{r_g}$	gear ratio [-]
$\boldsymbol{k_t}$	torsion bar stiffness $[Nm/rad]$
$\boldsymbol{J_r}$	lumped inertia of rotor and coupling shaft about rotor shaft $[Nm\ s^2/rad]$
$\boldsymbol{J_w}$	lumped inertia of steering rack and wheels about steering axis $[Nm\ s^2/rad]$
$\boldsymbol{T_M}$	output rotor torque steering actuator (before gear transmission) $[Nm]$
$\boldsymbol{T_w}$	lumped wheel torque about kingpin axis for both front wheels $[Nm]$
$\boldsymbol{d_r}$	rotor damping $[Nm\ s/rad]$
$\boldsymbol{d_w}$	rack and tire damping about steering axis $[Nm\ s/rad]$

2.1 Steer-by-wire setup

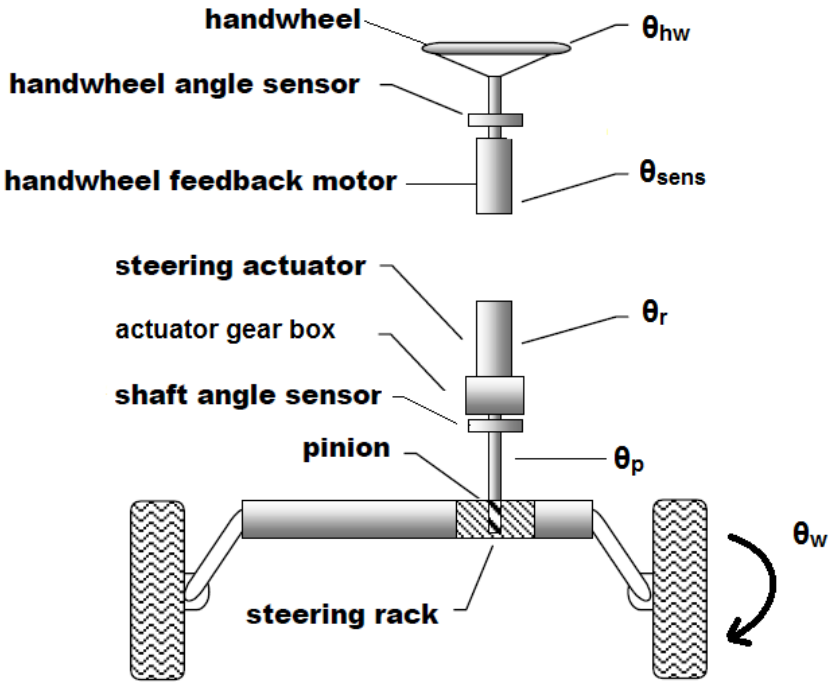

Figure 4. Steer-by-wire steering system design, modified from [4]

Figure 4 shows the setup of the steer-by-wire-system with rotary steering actuator. The driver input δ_{ref} is sensed and results (amplified) in a voltage input U to the actuator, which produces a motor output torque T_m at rotor speed $\dot{\theta}_r$. The electro-dynamic behavior of this partial system is described more in detail in chapter 4.

The steer-by-wire setup with linear steering actuator is generally not different to the one shown in Figure 4, but with replaced linear steering actuator so that the driver input is directly transferred into linear motion. In the following we will focus on the setup with rotary actuator. The considerations, however, can be easily transferred to the linear actuator setup.

Mechanical steering system

The dynamics of the steering system in Figure 2 can be described by the equations in the following. Equation (2-1) and (2-2) describe the mechanical steering system with lumped inertias about the rotor shaft J_r (2-4) and about the steering axis J_w (2-5) (kingpin axis). The motor output torque is transferred to the wheels by a gear box with ratio r_g and the rack-and-pinion-system with steering ratio r_s (2-3).

$$J_r\ddot{\theta}_r + d_r\dot{\theta}_r = T_M - T_L \tag{2-1}$$

$$J_w\ddot{\theta}_w + d_w\dot{\theta}_w = -T_w + T_L r_g r_s \tag{2-2}$$

$$\theta_p = r_s\theta_w \text{ and } \theta_r = r_g\theta_p \tag{2-3}$$

$$J_r = J_{rotor} + J_{gear} + J_{coup}/r_g \tag{2-4}$$

$$J_w = J_{wheel} + m_r r_{st,eff}^2 \tag{2-5}$$

The evaluation of wheel torque T_w, as the effective steering torque about the kingpin axis, is one of the major tasks of this thesis work and a function of suspension geometry and tire forces. The influence of suspension geometry on steering torque will be discussed in the upcoming sections. The tire forces are result of vehicle motion and, thus, a precise modeling of vehicle dynamics and tires is necessary, which is accomplished in chapter 3.

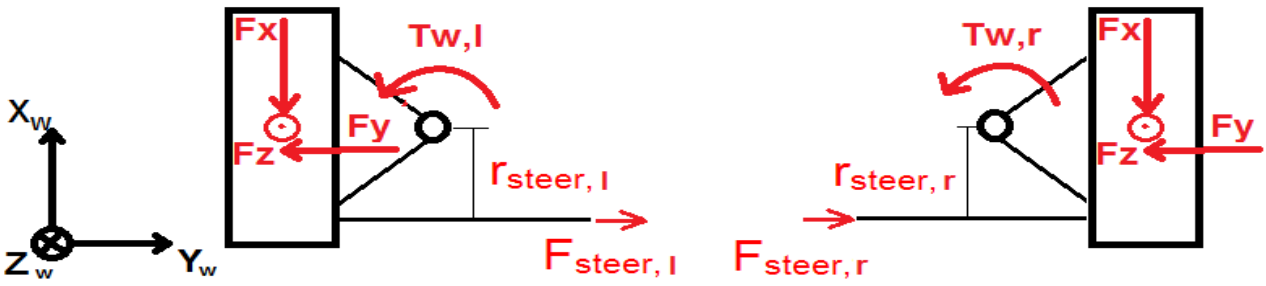

Figure 5. Steering torque as function of left and right kingpin moment in SAE coordinates

The wheel torque T_w (2-11) has to be understood as a lumped torque of left and right wheel steering torque (2-6 and 2-7). As can be seen from equation 2-8, due to symmetry longitudinal and vertical wheel forces cancel each other out for $F_{x,l} = F_{x,r}$ and $F_{z,l} = F_{z,l}$.

$$T_{w,l} = -F_{x,l}\, r_x - F_{y,l}\, r_y - F_{z,l}\, r_z \quad (2\text{-}6)$$

$$T_{w,r} = -F_{x,r}(-r_x) - F_{y,r}\, r_y + F_{z,r}\, r_z \quad (2\text{-}7)$$

$$T_w = T_{w,l} + T_{w,r} = \left(F_{x,r} - F_{x,l}\right) r_x - \left(F_{y,l} + F_{y,r}\right) r_y - \left(F_{z,l} - F_{z,r}\right) r_z \quad (2\text{-}8)$$

The wheels support each other, provided that there is a connecting steering rack between left and right side. The wheel torque due to lateral forces, however, always add up. The relations stated above are discussed more in detail throughout this work.

2.2 Suspension model

This chapter explains the general suspension geometry and how its parameter influence the wheel torque T_w. There are different suspension types, but they can all be described by same geometry parameters. For the EDV the double-wish-bone suspension type has been chosen [5].

Abbreviations and specific terms

$\boldsymbol{\sigma}$	kingpin inclination
$\boldsymbol{\tau}$	caster angle
$\boldsymbol{\lambda}$	effective kingpin angle
$\boldsymbol{e}$	caster trail
$\boldsymbol{t}$	pneumatic trail
$\boldsymbol{e_w}$	caster offset on wheel center height
$\boldsymbol{r_c}$	kingpin offset/ scrub radius
$\boldsymbol{r_w}$	kingpin offset on wheel center height
$\boldsymbol{\gamma}$	camber angle
$\boldsymbol{\varepsilon_T}$	toe angle
$\boldsymbol{\delta}$	wheel steer angle

Term	Description
kingpin axis	also referred to steering axis; this axis defines the wheel turning center when changing the steering angle.
kingpin inclination $\boldsymbol{\sigma}$	inclination of steering axis in y-z-plane (see Figure 7)
caster angle $\boldsymbol{\tau}$	steering axis inclination in x-z-plane (see Figure 6)
effective kingpin angle $\boldsymbol{\lambda}$	effective three-dimensional kingpin angle as sum of inclination and caster angle $\boldsymbol{\lambda} = \sqrt{\sigma^2 + \tau^2}$
caster trail $\boldsymbol{e}$	the longitudinal distance between where the steering axis hits the ground and the wheel center
pneumatic trail $\boldsymbol{t}$	the longitudinal distance between wheel center and lateral force acting point on tire contact patch plane
kingpin offset/ scrub radius $\boldsymbol{r_c}$	the lateral distance between where the steering axis hits the ground and the wheel center (negative if on outside of the wheel)
camber angle $\boldsymbol{\gamma}$	inclination of wheels y-z-plane (see Figure 7)
toe angle $\boldsymbol{\varepsilon_T}$	tilt of wheels in x-y-plane (see Figure 6)
uprights	uprights are the mounting parts, which connect wheels with suspension parts and steering system. The brake system is also mounted on the uprights.
wishbones	Wishbones are part of the suspension system and connect uprights with the vehicle chassis. They allow the wheels to move in vertical direction during bumping and define the degrees of freedom of the wheel.

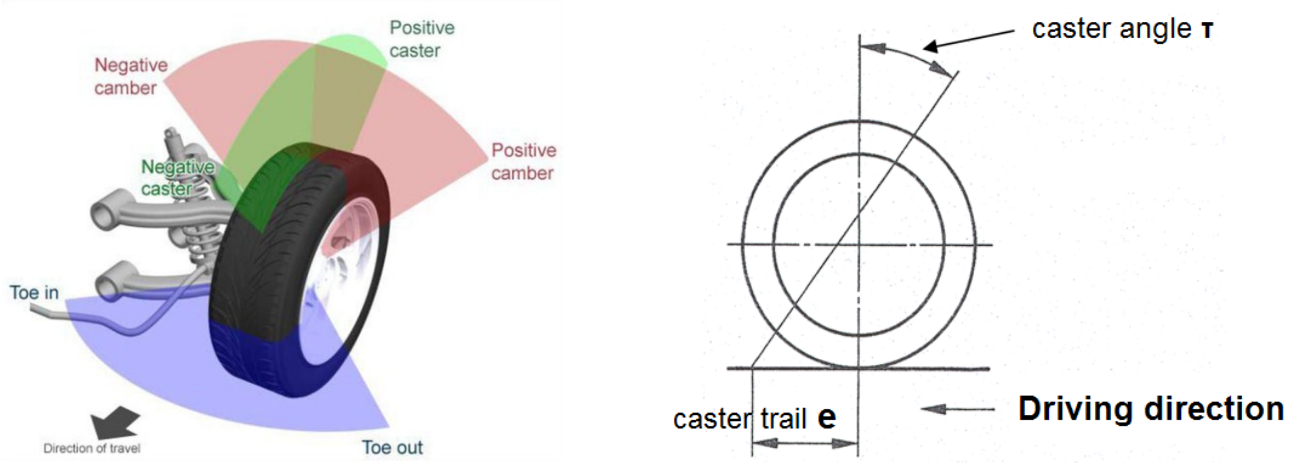

Figure 6. Left: Determination of wheel angles, from [2], Right: Caster angle and caster trail, from [6]

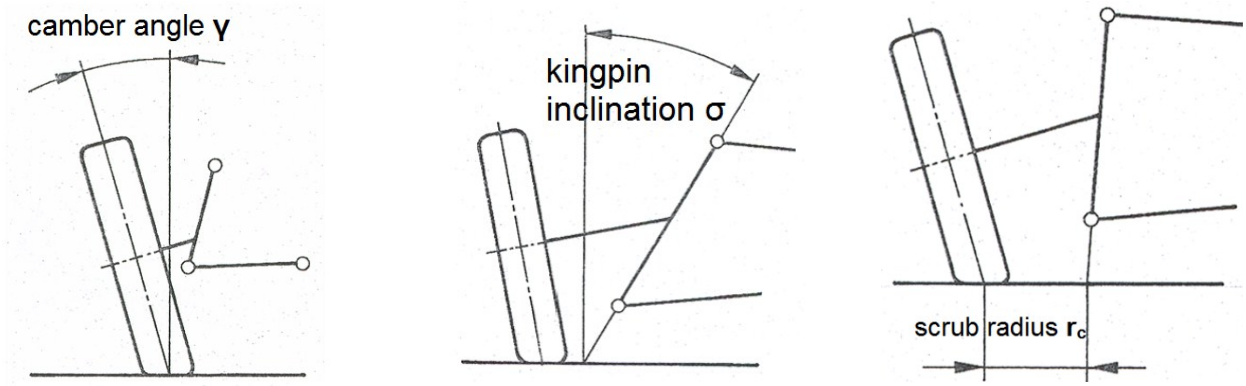

Figure 7. Left: Camber angle , from [6], Middle: Kingpin inclination, from [6], Right: Kingpin offset/ scrub radius, from [6],

Suspension geometry model

The suspension geometry plays a major role in defining the forces on the steering rack. The relative position of the kingpin axis to the wheel- as the rotating axis of the wheel with fixed relative position to vehicle chassis - is described in this model. However, the assumption of a fixed relative position of kingpin axis to vehicle chassis is not completely correct. Especially during vertical wheel motion due to road bumps the relative position changes considerably. This fact is taken into account by varying the geometrical parameters.

Forces in longitudinal, lateral and vertical direction produce a moment around the kingpin axis, which results in the steering rack force (see *Figure 8*). Once, the forces acting on the wheel are properly defined the steering rack force can be easily calculated. The model presented in the following is based on the work of Cho [7].

Limitations of model

- rigid suspension components
- no motion induced changes: thus, no change of caster angle and kingpin inclination (as mentioned before, dynamics changes are considered by variance of suspension parameter)
- strictly speaking, this model is only valid for quasi-static motion, since it only describes the geometric relations. However, assuming rigid suspension components, negligible damping and inertia of suspension $J_{susp} \ll J_w \ll J_{car}$, dynamics forces of the suspension system during wheel turn can be neglected and, thus, the model can be also used for dynamic case scenarios

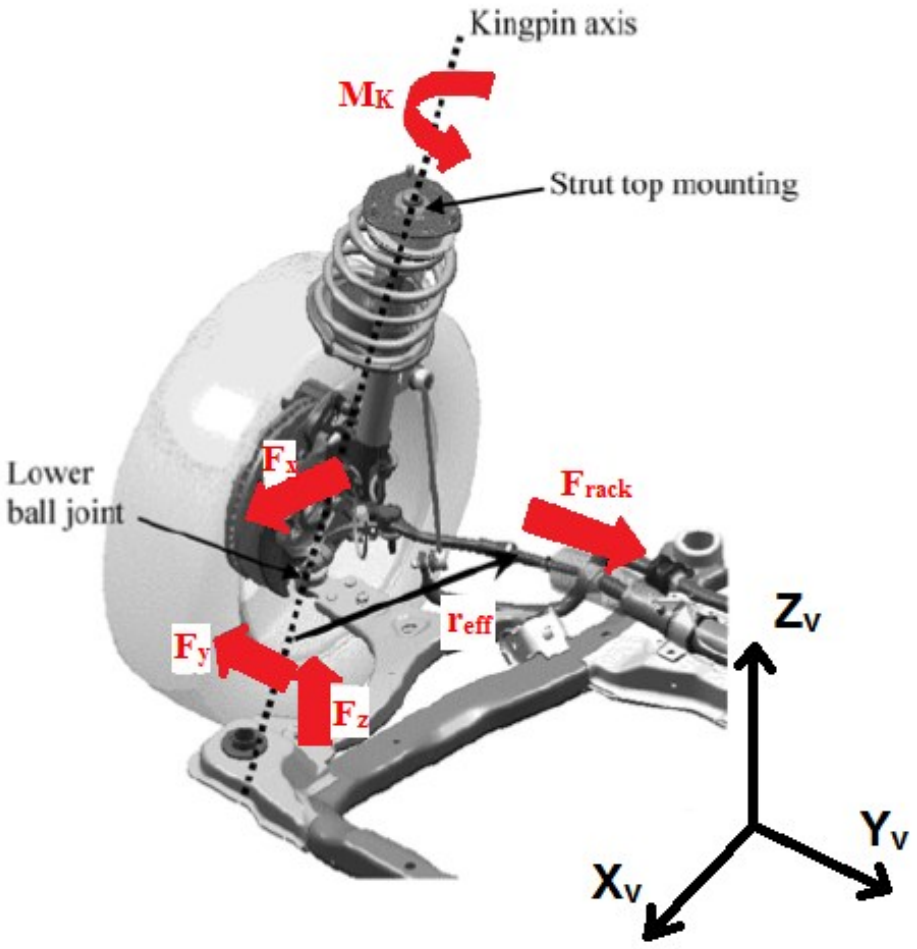

Figure 8. Steering forces on suspension, modified from [7]

Model description

By subdividing the coordinate system into three sub coordinate systems for kingpin axis, wheel and contact patch plane on the road, as it has been done in Figure 9, one can describe the geometric relations between its components and the degrees of freedom of the whole system.

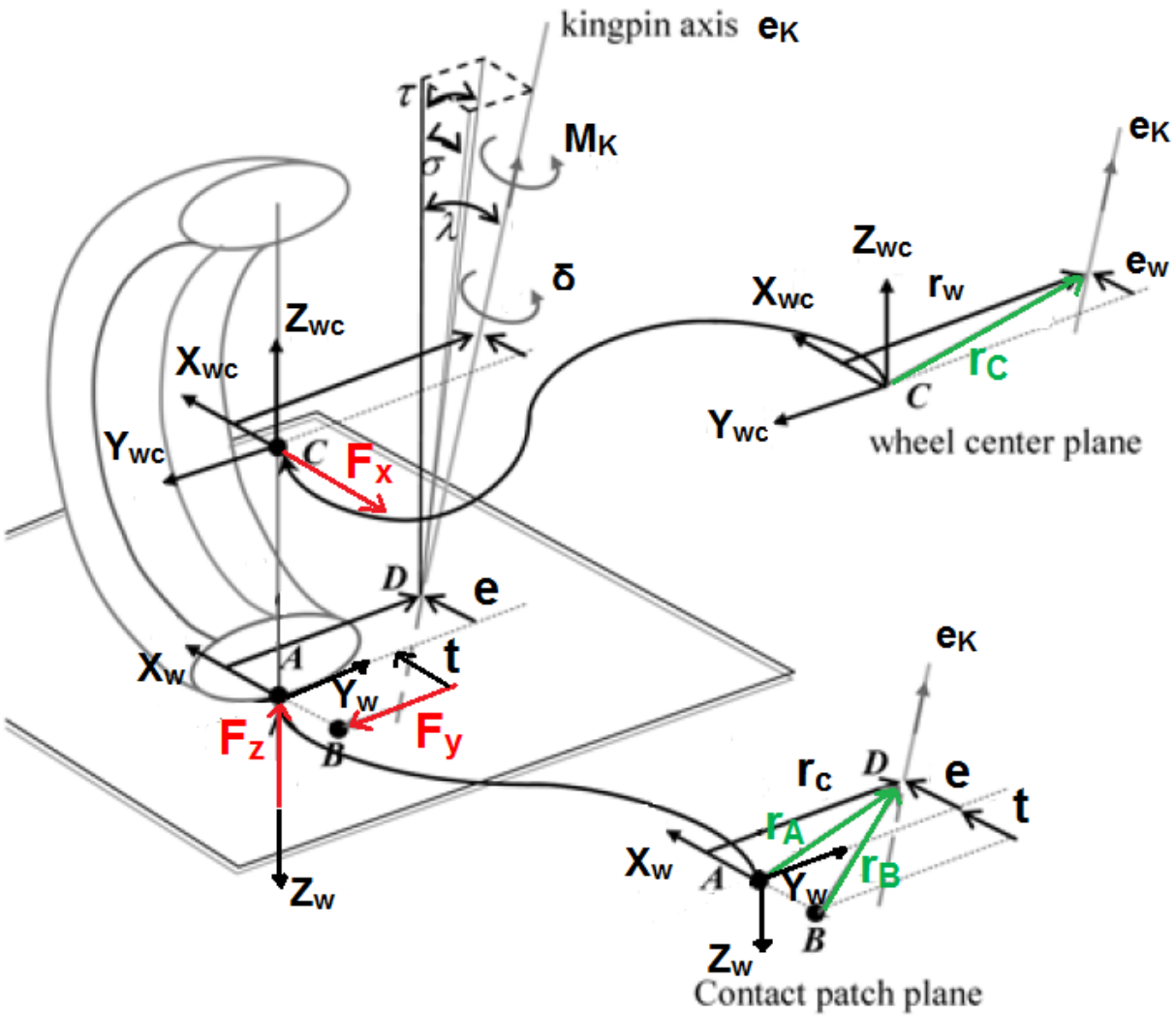

Figure 9. , Suspension coordinate system, modified from [7]

Despite the three sub-coordinate-systems, displacement vectors r_i, tire forces F_i and kingpin vector e_k are in the vehicle coordinate system X_V, Y_V, Z_V in equation 2-9 to 2-11. Since tire forces F_i are generally described in tire coordinates they have to be transferred in vehicle coordinates.

$$\boldsymbol{M_{KX}} = (\boldsymbol{r_C} \times \boldsymbol{F_X}) \cdot \boldsymbol{e_K} \qquad \text{with } \mathbf{r_A} = -\begin{pmatrix} \mathbf{e}\cos\delta + \mathrm{r_C}\sin\delta \\ \mathbf{e}\sin\delta - \mathrm{r_C}\cos\delta \\ 0 \end{pmatrix} \qquad \text{2-9}$$

$$\boldsymbol{M_{KY}} = (\boldsymbol{r_B} \times \boldsymbol{F_Y}) \cdot \boldsymbol{e_K} \qquad \text{with } \boldsymbol{r_B} = -\begin{pmatrix} (\mathrm{e}+\mathrm{t})\cos\delta + r_C\sin\delta \\ (\mathrm{e}+\mathrm{t})\sin\delta - r_C\cos\delta \\ 0 \end{pmatrix} \qquad \text{2-10}$$

$$\boldsymbol{M_{KZ}} = (\boldsymbol{r_A} \times \boldsymbol{F_Z}) \cdot \boldsymbol{e_K} \qquad \text{with } \boldsymbol{r_C} = -\begin{pmatrix} e_w\cos\delta + r_W\sin\delta \\ e_w\sin\delta - r_W\cos\delta \\ 0 \end{pmatrix} \qquad \text{2-11}$$

The longitudinal force F_X can be sufficiently described by the force acting on the wheel center. Differently to vertical and lateral force, does the wheel radius not affect the kingpin moment due to longitudinal forces. For the side slip force F_Y and vertical force F_Z the force acting point at the tire-

to-ground contact patch has to be considered. For each force acting point, the displacement vector r_i (as can be seen in equation 2-9 to 2-11**)** is defined, from which the moment around the kingpin axis is calculated.

Equation 2-12 shows the transformation between forces in the vehicle coordinate system X_V, Y_V, Z_V and wheel coordinate system X_W, Y_W, Z_W using transformation matrix. The kingpin axis vector e_K is given in equation 2-13 for vehicle coordinates.

$$\begin{pmatrix} F_X \\ F_Y \\ F_Z \end{pmatrix}_V = \begin{pmatrix} cos\,\delta & sin\,\delta & 0 \\ -sin\,\delta & cos\,\delta & 0 \\ 0 & 0 & 1 \end{pmatrix} \begin{pmatrix} F_X \\ F_Y \\ F_Z \end{pmatrix}_W \qquad 2\text{-}12$$

$$\text{kingpin axis unit vector } \boldsymbol{e_K} = \begin{pmatrix} \tan\tau\cos\lambda \\ tan\,\sigma\cos\lambda \\ -\cos\lambda \end{pmatrix} \qquad 2\text{-}13$$

Using those relations, the kingpin moments due to longitudinal, lateral and vertical tire forces can be simplified to 2-14, 2-15 and 2-18.

$$M_{kx} = \boldsymbol{M_x} \cdot \boldsymbol{e_K} = F_x\, r_w\, cos\,\lambda \qquad 2\text{-}14$$

$$M_{ky} = \boldsymbol{M_y} \cdot \boldsymbol{e_K} = F_y\,(e + t) cos\,\lambda \qquad 2\text{-}15$$

$$M_{kz} = \boldsymbol{M_z} \cdot \boldsymbol{e_K} = F_z\,(-e\sin\delta + r_c\cos\delta)\tan\tau\cos\lambda + F_z\,(e\cos\delta + r_c\sin\delta)\tan\sigma\cos\lambda \qquad 2\text{-}16$$

As can be seen from equation 2-14 to 2-16, does only the kingpin moment M_{kz} due to vertical forces change with steering angle δ. This effect is known as car-lifting-effect. The lever arms of lateral and longitudinal force are kept constant. One can see from equation 2-16, that the car-lifting-effect only applies for $\sigma \neq 0$ and $\tau \neq 0$.

Influence of effective kingpin angle $\boldsymbol{\lambda}$

The kingpin moment due to longitudinal, lateral and vertical tire forces is affected by caster angle σ and kingpin inclination τ, expressed by the effective kingpin angle $\lambda = \sqrt{\sigma^2 + \tau^2}$. The influence of effective kingpin angle is described in equation 2-17 and 2-18.

$$\mathrm{M_k} = \mathbf{M_{z,i}} \cdot \mathbf{e_k} = -\cos\lambda\, \mathrm{M_{z,i}} \qquad 2\text{-}17$$

$$\mathrm{M}_{k,\mathrm{steer}} = \frac{1}{-\cos\lambda}\, \mathrm{M_{z,i}} \qquad 2\text{-}18$$

Equation 2-17 and 2-18 show primarily the effects of effective kingpin inclination on torque transmission between wheel torque and kingpin torque (steering torque). This means, the impact of wheel forces and the steering effort to maintain force equilibrium on the wheels is reduced. Simultaneously steering effort necessary to turn the wheels is increased. For a range of $0 \leq \lambda \leq 24°$ is this effect not much with steering effort change of roughly $\mathrm{M_{steer}} \pm 10$ %. However, we will see in chapter 3, that the variation of caster and kingpin inclination also influences the forces and wheel torque amplitude itself, which leads to considerable increment of steering effort.

Figure 10 below illustrates the geometric parameter of the kingpin axis. One should take in mind, that the kingpin axis is a virtual axis, which is defined by the two mounting at the uprights and, thus, scrub radius can be also negative, which can change sign of M_{kx} and M_{kz}.

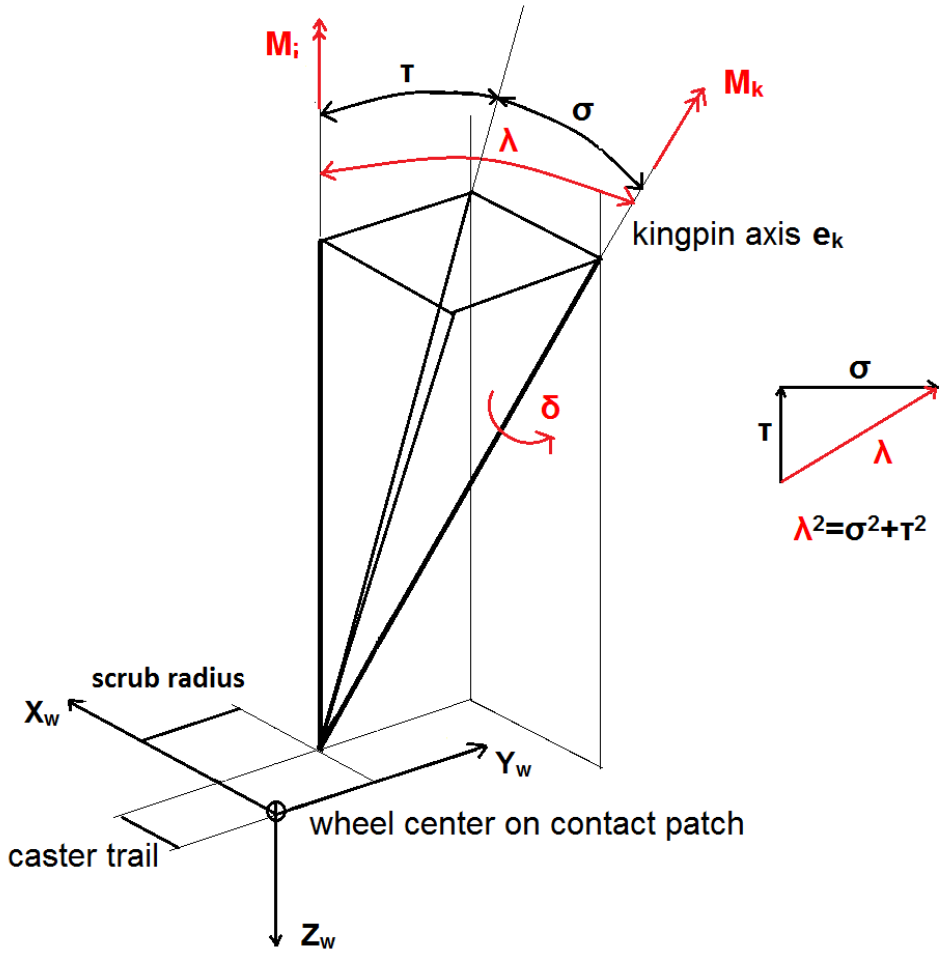

Figure 10. Kingpin axis coordinates

2.3 Disturbance model

The disturbance model considers a change of lever arms due to the change of the force acting points on the wheel. This can have crucial impact on the steering effort, since the suspension geometry is generally designed for reducing the steering effort. This means, that the distance of kingpin axis to force acting points is designed to be as small as possible for standard driving situations. As we will see later in chapter 3 the change of force acting points on the wheel results also in considerable change of tire forces and, hence the kingpin moment.

Figure 11 shows the change of force acting points on the tire due to disturbance for longitudinal, lateral and vertical tire forces.

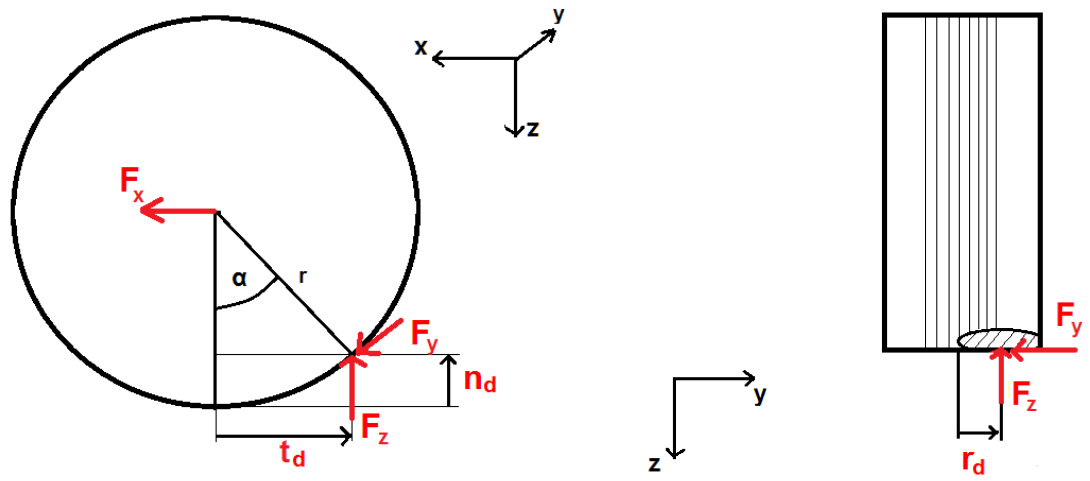

Figure 11. *Left: Vertical and longitudinal shift of force acting point, Right: Lateral shift of force acting point*

Equation 2-19, 2-20 and 2-21 show that the decrease of contact patch area doesn't increase steering effort.

$$\mathbf{r_A} = -\begin{pmatrix} (\mathrm{e} + \mathrm{t_d})\cos\delta + (\mathrm{r_C} + \mathrm{r_d})\sin\delta \\ (\mathrm{e} + \mathrm{t_d})\mathrm{csin}\,\delta - (\mathrm{r_C} + \mathrm{r_d})\cos\delta \\ 0 \end{pmatrix} \qquad M_{kx} = \boldsymbol{M_x} \cdot \boldsymbol{e_K} = F_x\,(r_W + r_d)\cos\lambda \qquad 2\text{-}19$$

$$\boldsymbol{r_B} = -\begin{pmatrix} (e + t + t_d)\cos\delta + (r_C + r_d)\sin\delta \\ (e + t + t_d)\sin\delta - (r_C + r_d)\cos\delta \\ 0 \end{pmatrix} \qquad M_{ky} = \boldsymbol{M_y} \cdot \boldsymbol{e_K} = F_y\,(e + t + t_d)\cos\lambda \qquad 2\text{-}20$$

$$\boldsymbol{r_C} = -\begin{pmatrix} e_w\cos\delta + (r_W + r_d)\sin\delta \\ e_w\sin\delta - (r_W + r_d)\cos\delta \\ 0 \end{pmatrix}$$

$$M_{kz} = \boldsymbol{M_z} \cdot \boldsymbol{e_K} = F_z\,(-(\mathrm{e} + \mathrm{t_d})\sin\delta + (\mathrm{r_C} + \mathrm{r_d})\cos\delta)\tan\tau\cos\lambda + F_z\,((\mathrm{e} + \mathrm{t_d})\cos\delta + (\mathrm{r_C} + \mathrm{r_d})\sin\delta)\tan\sigma\cos\lambda$$

2-21

We can see again that the change of lever arm is independent of steering angle for M_{kx} and M_{ky}. Despite the fact of the force shift (in the right-hand figure of *Figure 11*), one should also consider the reduction of contact patch size during disturbance in *Figure 12*. The contact patch becomes important when it comes to turning the wheel, as we will see in chapter 3. However, we can already show at this point, that the reduction of contact patch area results also in a reduction of steering torque, considering that tire forces stay the same due to unchanged wheel load (see equation *2-22* to *2-24*).

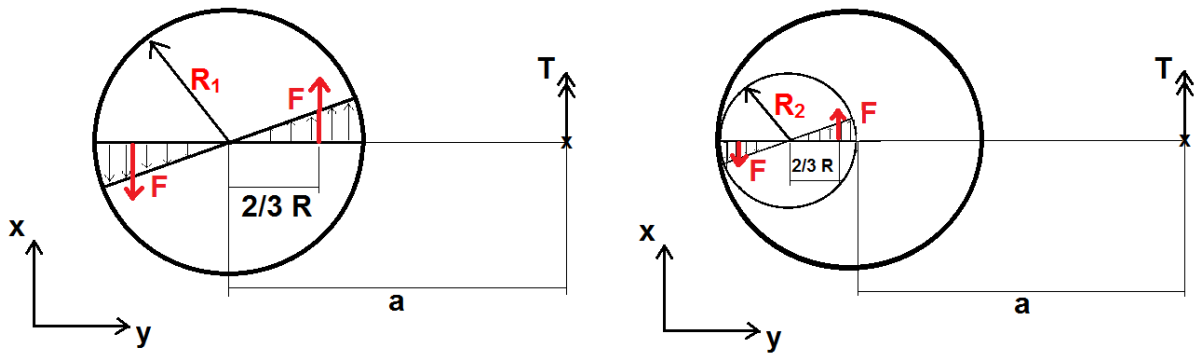

Figure 12. Effects of lateral shift on static torque

Equation 2-22, 2-23 and 2-24 show that the decrease of contact patch area doesn't increase steering effort.

$$T_{\text{steer}} = -F\left(a - {}^{2}/_{3}\, R_1\right) + F\left(a + {}^{2}/_{3}\, R_1\right) = {}^{4}/_{3}\, FR_1 \qquad 2\text{-}22$$

$$T_{\text{steer,d}} = -F\left(a + {}^{1}/_{3}\, R_2\right) + F\left(a + {}^{5}/_{3}\, R_2\right) = {}^{4}/_{3}\, FR_2 \qquad 2\text{-}23$$

$R = R_1 \geq R_2$: $$T_{\text{steer,d}} \leq T_{\text{steer}} = {}^{4}/_{3}\, FR \qquad 2\text{-}24$$

2.4 Transfer function of suspension model

For the aims of simplification one can linearize the equations 2-14 to 2-16. This is especially helpful when considering high speed scenarios, in which small steering angles can be considered and, thus, we can assume $\sin\delta \approx \delta$ and $\cos\delta \approx 1$.

With 2-25, 2-26 and 2-27 the linearized torque equations are given.

$$T_{\text{w,x}} = \left(F_{x,fl} - F_{x,fr}\right) r_w \cos\lambda \qquad 2\text{-}25$$

$$T_{\text{w,y}} = \left(F_{y,fl} + F_{y,fr}\right)(e+t)\cos\lambda = F_{y,f}(e+t)\cos\lambda \qquad 2\text{-}26$$

$$\begin{aligned} T_{w,z} &= \left\{F_{z,fl}[(-e\delta + r_c)\tan\tau + (e + r_c\delta)\tan\sigma]\right. \\ &\quad \left. - F_{z,fl}\left[(-e(-\delta) + r_c)\tan\tau + \left(e + r_c(-\delta)\right)\tan\sigma\right]\right\}\cos\lambda \\ T_{w,z} &= \left(F_{z,fl} + F_{z,r}\right)(r_c\tan\sigma - e\tan\tau)\delta\cos\lambda \\ &\quad + \left(F_{z,fl} - F_{z,r}\right)(r_c\tan\tau + e\tan\sigma)\cos\lambda \end{aligned} \qquad 2\text{-}27$$

For the symmetric case with $1/2\, F_{x,f} = F_{x,fl} = F_{x,fr}$, $1/2\, F_{y,f} = F_{y,fl} = F_{y,fr}$ and $1/2\, F_{z,f} = F_{z,fl} = F_{z,fr}$ equations 2-25, 2-26 and 2-27 can be rewritten to 2-28, 2-29 and 2-30.

$$\frac{T_{\text{w,x}}(s)}{F_{x,f}(s)} = 0 \qquad 2\text{-}28$$

$$\frac{T_{\text{w,y}}(s)}{F_{y,f}(s)} = (e+t)\cos\lambda \qquad 2\text{-}29$$

$$\frac{T_{\text{w,y}}(s)}{F_{z,f}(s)\ \delta(s)} = (r_c\tan\sigma - e\tan\tau)\cos\lambda \qquad 2\text{-}30$$

2.5 Suspension setup

As we have seen, the steering effort necessary to turn the wheel depends on suspension geometry. For this reason, three different setups (see *Table 3*) have been chosen. The analysis of steering power requirements will be accomplished for those three setups.

The data for conventional cars can't be accessed easily from car manufacturers. Thus, it is based on data found on internet forums, received by individual measurements made on different car types. Same applies for the ATV, for which the measurements have been made at a local ATV supplier in Göteborg (see [5]).

Table 3 shows the detailed suspension geometry setup used in the simulation, including derivation from the median value. This change of parameters is on the one hand due to a certain inaccuracy and different suspension setups, but also takes into account the parameter change during dynamic conditions, such as vertical movement

Table 3. Analyzed suspension geometry setups (parameter are explained in section 2.2)

Parameter	Conventional car	ATV	"Zero angle" setup
caster angle $\boldsymbol{\tau}$	$\boldsymbol{\tau} = 5 \pm 10\ deg$	$\boldsymbol{\tau} = 11 \pm 3.0\ deg$	$\boldsymbol{\tau} = 0 \pm 1.0\ deg$
kingpin offset $\boldsymbol{r_c}$	$\boldsymbol{r_c} = 10 \pm 10\ mm$	$\boldsymbol{r_c} = -28 \pm 50\ mm$	$\boldsymbol{r_c} = 40 \pm 40\ mm$
kingpin incl. $\boldsymbol{\sigma}$	$\boldsymbol{\sigma} = 12.5 \pm 2.5\ deg$	$\boldsymbol{\sigma} = 18 \pm 2.0\ deg$	$\boldsymbol{\sigma} = 0 \pm 3.0\ deg$
eff. kingpin angle $\boldsymbol{\lambda}$	$\boldsymbol{\lambda} = 13.5° - 21.0°$	$\boldsymbol{\lambda} = 21.0° - 24.5°$	$\boldsymbol{\lambda} = 0.0° - 3.0°$

Figure 13 shows the CAD of the EDV suspension with the assigned suspension parameter discussed in chapter 2. The proportions in this figure are not as in reality, but to clarify some parameters are shown in enlarged size. One can see, that position of the kingpin axis (red line) for this double-wishbone setup is defined by the upper and lower pivot point (outer-ball joints) on the upright (blue part). The scrub radius r_c should be reduced as much as possible to reduce steering efforts, which can be achieved by either shortening the distance between outer-ball joints and wheel center line and/or kingpin inclination σ.

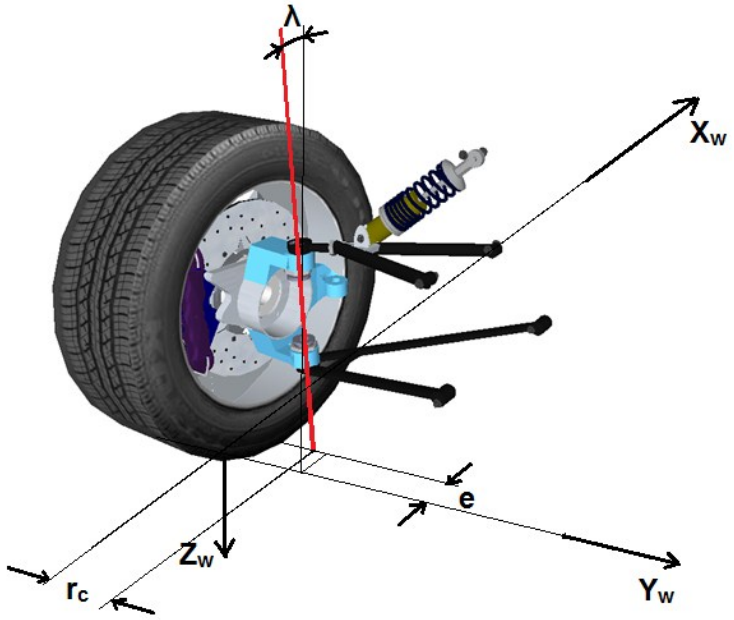

Figure 13. Suspension geometry of EDV, modified from [1]

3 Tire forces

This chapter provides the analysis of tire forces in relevant driving situations. Better speaking, the following chapter considers various load case scenarios for which maximum power requirements on steering actuator are expected. This is accomplished by analyzing the tire forces in specific driving scenarios. Hence, the following subchapters can be each seen as a separate driving scenario.

3.1 Driving scenarios

Relevant for defining critical driving scenarios is understanding of the relation between steering torque on right and left steered wheel. Generally speaking for longitudinal and vertical wheel forces, the steering effort is proportional to the difference between resulting kingpin moments on left and right wheel. The kingpin moments due to lateral forces, however, add up due to the same acting direction of lateral forces during cornering.

Thus, driving situations have to be identified, in which forces on right and left wheel counter-act or the great difference between left and right wheel kingpin moment occur.

1. **Spin torque in parking conditions:** Steering effort to turn the wheels in stand-still conditions is increased due to the relaxation length of the tire and, thus, maximum steering torque to spin the wheels, occurs at $v = 0$. This effect is further explained in the upcoming section and the evaluation of maximum static torque is shown in section 3.3.

2. **Lateral tire forces in high-speed cornering:** As has been described before, lateral tire forces differ from the impact of longitudinal and vertical tire forces, since their kingpin moments generally add up due to the same acting direction of F_y. F_y increases with increased lateral acceleration a_y and, thus, with increased cornering speed. The kingpin moment $M_{z,y}$ due to lateral forces is often referred to the term *self-alignment-torque*, since it results in the wheels keeping straight-line direction. However, it will be shown in chapter 3.4, that there is a peak value before F_y reaches its maximum due to a reduction of pneumatic trail.
   The influence of caster trail on kingpin moment $M_{z,y}$ has been discussed in chapter 2 already in terms of suspension geometry. In relation to self-alignment torque it is worth it looking into it again, since the presence of constant caster trail leads to a considerable change of the alignment torque characteristic. The standard model shows that alignment torque becomes zero when the tires are saturated. The saturated tire still produces lateral tire forces, though, which is why with caster trail still a high alignment torque is present at high slip angles.

3. **Combined steering and braking:** Combined steering and braking is a common driving scenario, especially in emergency braking. Kingpin moment $M_{z,x}$ and $M_{z,y}$ occur at the same instant of time, which increases the overall steering torque. Nevertheless, in this scenario the tire saturation has major impact, since sum of longitudinal and lateral tire forces is restricted by the physical limits of the tire.

4. **Dynamic wheel load on bumpy roads:** During driving on bumpy road considerably high vertical wheel loads occur. Those forces are strongly influenced by the vehicle parameters, such as suspension stiffness and damping, tire properties, sprung- to unsprung-mass ratio, etc. For defining the forces a detailed analysis of vertical dynamics is necessary, which can be found in APPENDIX A. The influence of different suspension geometry setups can be found in chapter 3.7

3.2 Relaxation length and spin torque

Two effects are important to understand steering effort. One is the so-called spin torque, which has to be overcome to turn (spin) the wheels. In high speed driving high forces act on the tires and produce a moment about the kingpin axis. To maintain steering angle $\delta = const.$ steering torque is necessary to maintain torque equilibrium about the kingpin axis. The latter case is described in detail in the upcoming section.

The spin torque has major impact in creep speed driving, which is mainly influenced by the relaxation length of the tire. Due to the elasticity of the tire, tire forces (especially lateral tire forces) will not directly build up, but take a certain time to reach steady-state. Thus, there is a certain time lag for the forces to build up. This time lag is a function of wheel rotation speed ω and, hence, the cruising speed v of the car. This time lag again can be expressed as damping coefficient, depending on wheel rotation speed ω. G. Rill [8] presents a model to describe those dynamic tire forces F_y^D as a first-order system (3-1).

$$\underbrace{F_y(v_y + \dot{y}_e)}_{F_y^D} \approx \underbrace{F_y(v_y)}_{F_y^S} + \frac{\partial F_y}{\partial v_y}\dot{y}_e \qquad 3\text{-}1$$

$$\frac{\partial F_y}{\partial v_y} = \frac{\partial F_y}{\partial s_y}\cdot\frac{\partial s_y}{\partial v_y} = \frac{\partial F_y}{\partial s_y}\cdot\frac{-1}{r_D|\Omega|} \qquad 3\text{-}2$$

$$s_y = \frac{-v_y}{r_D|\Omega|} \qquad \alpha = \arctan s_y \qquad 3\text{-}3$$

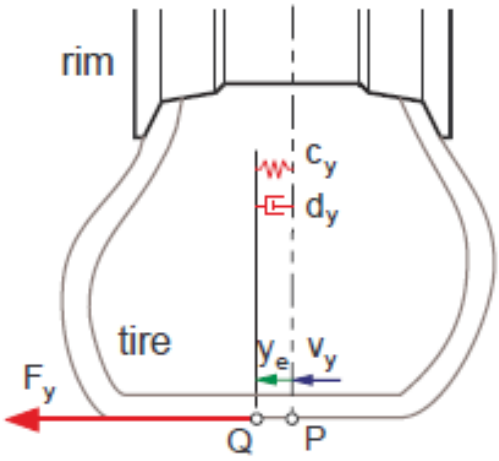

Figure 14. Lateral tire deflection [8]

Without going too much into detail at this point, it can be shown that the dynamic tire force F_y^D can be written as function of lateral deflection y_e of the tire itself (3-4), with lateral stiffness c_y and the lateral damping property of the tire d_y (see also APPENDIX B).

$$F_y^D = c_y y_e + \underbrace{\left(d_y + \frac{\partial F_y}{\partial s_y}\cdot\frac{1}{r_D|\Omega|}\right)}_{\hat{d}_y}\dot{y}_e \qquad 3\text{-}4$$

We can see, that the new damping coefficient $\overline{d_y}$ is now also a function of cornering stiffness $\frac{\partial F_y}{\partial s_y}$ and wheel rotation speed Ω and will decrease with increasing velocity. Equation 3-5describes the force equilibrium in point Q in Figure 14.

$$F_y^D = C_{F\alpha}\alpha + D_{F\alpha}\dot{\alpha} \qquad 3\text{-}5$$

From there, the kingpin torque due to lateral force T_y^D can be calculated. Basically, this explains why spin torque decreases with increased velocity and why wheel turn in parking situation requires the most steering effort.

To explain this effect, it was necessary to approach the problem form wheel dynamics perspective with the lateral deflection of the tire. In the following sections dynamic tire forces are described in terms of tire slip and the forces between tire and ground. The relation between both is given by equilibrium in point Q in. From now on the tire itself will be assumed to be stiff and tire deflection y_e will be considered by cornering stiffness $C_{F\alpha}$ and damping $D_{F\alpha}$.

3.3 Spin torque in static conditions

R.Sc. Sharp and R. Granger [9] developed an empirical formula for static torque prediction around the kingpin axis in stand-still situations. It is based on a model in physical macro-scale and integrates friction forces over a circular contact patch.

Specific terms	Description
tire friction	the effect of tire slip forces in longitudinal and lateral direction due to shear stress as a result of deformation of tire and profile elements
tire stiction	the effect of sudden reduction of friction forces due to tire saturation

Limitations of model

The model restricted by the following assumptions and limitations:

- Perfectly circular contact patch
- Pressure is equally distributed over contact patch (correction factor n in equation 3-9)
- Torque center coincides with contact patch center
- No stiction effects considered (friction based on experimentally obtained coefficient)
- Zero caster angle and zero kingpin inclination: lever arms stay constant during wheel turn

Model

The model of R.Sc. Sharp and R. Granger [9] considers a circular contact patch, as can be seen in Figure 15.

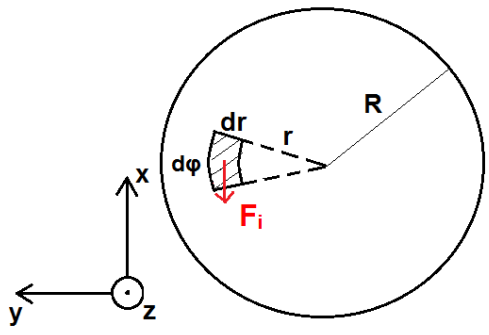

Figure 15. Static torque due to friction forces in circular contact patch plane

The model evaluates the static torque by analyzing the tire-to-ground friction over the whole contact patch. In equation 3-6 the tire friction forces are summed up over the contact patch. The parameters are given in Table 4.

$$T_{stat} = \int_0^{2\pi} \int_0^{R} \mu p_0 r^2 dr d\varphi = \int_0^{2\pi} \frac{\mu p_0 R^3}{3} d\varphi = \frac{2\pi}{3} \mu p_0 R^3 \qquad 3\text{-}6$$

$$F_{z,stat} = \mathrm{p_0 \pi R^2} \qquad 3\text{-}7$$

Table 4. Static tire model parameters

Term	Description
$\boldsymbol{R}$	contact patch radius
$\boldsymbol{F_i}$	friction force of infinite contact patch element $dA = rdrd\varphi$
$\boldsymbol{F_{z,stat}}$	static wheel load $[N]$
$\boldsymbol{p_0}$	internal tire pressure $[bar]$
$\boldsymbol{p}$	effective tire-to-ground pressure $[bar]$
$\boldsymbol{n}$	empirical correction factor (R. Granger suggest $n = 0.78$;depends on tire type)

The friction force $F_i = \mu_i p_i dA$ and its resulting static torque $T_{stat,i} = F_i \cdot r_i$ of each infinite small element $dA = rdrd\varphi$ of the contact patch plane is integrated about the whole contact surface in Equation 3-6. By equation 3-7 the contact patch center radius R can be eliminated, which leads to expression 3-8. Equation 3-8 is independent of the size of the contact patch, since it is assumed that the pressure is evenly distributed on the patch.

$$T_{\mathrm{stat}} = \frac{2\mu}{3} \frac{{F_{z,stat}}^{1.5}}{\sqrt{\pi \mathrm{p_0}}} \qquad 3\text{-}8$$

$$T_{\mathrm{stat}} = {p_0}^{n-0.5} \frac{2\mu}{3\sqrt{\pi}} \frac{{F_{z,stat}}^{1.5}}{p^n} \qquad 3\text{-}9$$

Equation 3-9 contains an empirical correction factor n since for low tire pressures, the tire-to-ground contact pressure will be greater at the edges of the contact area and lesser in the middle. The converse will be true for high inflation pressures.

The given formula is a function of the three parameters tire inflation pressure, wheel load and tire-to-road friction. The authors could experimentally show that it builds up the reality in good approximation for normal stand-still conditions and that the static torque is independent of the scrub radius. This is due to the compensation of the lever arm increment with the ability of the wheel to roll with increased lever arm r_C, which has been shown in [9]. This is only valid for the non-locked wheel case, as described in the following.

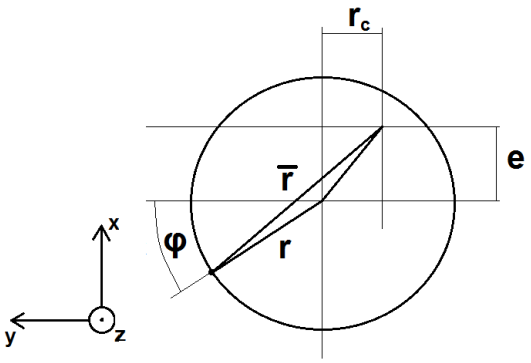

Figure 16. Change of static torque lever arm due to caster trail and scrub radius

Equation 3-8 considers only zero caster trail. To show the effect of spin center offset equation 3-8 has to be slightly modified. If we consider both, caster trail $e$and scrub radius r_c, it can be seen in *Figure 16*, that the effective lever arm changes from r (3-10) to $\bar{r}$ (3-11).

$$r^2 = \underbrace{r^2 sin^2\varphi}_{r_x} + \underbrace{r^2 cos^2\varphi}_{r_y} \qquad 3\text{-}10$$

$$\begin{aligned}\bar{r}^2 &= (r_x + e)^2 + \left(r_\mathrm{y} + r_\mathrm{c}\right)^2 = \cdots \\ &= r^2\left[1 + 2(k_e \sin\varphi + k_{rc}\cos\varphi) + \left({k_e}^2 + {k_{rc}}^2\right)\right]\end{aligned} \qquad 3\text{-}11$$

The static spin torque equation can then be rewritten to 3-12:

$$\bar{T}_{stat} = \int_0^{2\pi}\int_0^{R} \mu p_0 \bar{r} r dr d\varphi = \cdots = \frac{2\pi}{3}\mu p_0 R^3\sqrt{1 + \left({k_e}^2 + {k_{rc}}^2\right)} \qquad 3\text{-}12$$

Hence, static spin torque $\bar{T}_{\mathrm{stat}}$ changes by the factor k (equation 3-13), with $e = k_e R$ and $r_c = k_{rc} R$.

$$\bar{T}_{\mathrm{stat}} = k \cdot \frac{2\mu}{3}\frac{{F_{z,stat}}^{1.5}}{\sqrt{\pi \mathrm{p}_0}} = \sqrt{1 + \left({k_e}^2 + {k_{rc}}^2\right)} \cdot \frac{2\mu}{3}\frac{{F_{z,stat}}^{1.5}}{\sqrt{\pi \mathrm{p}_0}} \qquad 3\text{-}13$$

For free rolling wheels factor k reduces to $k = k_{free} = \sqrt{1 + {k_e}^2}$, so that spin torque is independent of scrub radius r_c. However, if we consider locked wheels, the change of scrub radius has impact on static spin torque and we have to use $k = k_{lock} = \sqrt{1 + \left({k_e}^2 + {k_{rc}}^2\right)}$.

If we consider further the locked wheel case or driving up a curb, one could consider longitudinal tire force as a function of motor torque. However, if we consider that motor torque is $T_{max} = 150\ Nm$, we can show that $F_{x,max,motor} = T_{max}/r_{dyn} \approx 900\ N < \mu F_z$. In section 3.6 the case of tire force $F_i = \mu F_z$ will be considered, so that no additional considerations are necessary at this point.

Results

Figure 17 shows the prediction of static steering torque based on the modified model of R. Granger for free rolling wheels. As can be seen, the result is strongly influenced by the change of inflation pressure. The effective kingpin inclination λ has minor impact, which is why the plot is given for different wheel load scenarios. *W*. R. Granger experimentally identified the tire-to-road friction coefficient for dry road conditions to $\mu = 0.66$ [9]. However, for the given plot a friction coefficient of $\mu = 1.5$ has been considered. This coefficient is higher than in reality, but offers a certain security margin, which is why this value will be considered from now on.

In normal conditions an inflation pressure of 2 bar is assumed, so that the static spin torque is $\bar{T}_{stat,free} \approx 52 - 75\ Nm$ for both wheels for the given load scenarios and $e = 20\ mm$. This result considers the wheels to be free rolling in case of scrub radius $r_c \neq 0$.

If we consider locked wheels, however, scrub radius r_c has influence on static spin torque so that for $r_c = e = 20\ mm$ a static spin torque of $\bar{T}_{stat,lock} \approx 55 - 88\ Nm$ can be estimated.

Table 5. Static torque prediction for inflation pressure p=2 bar

Parameter	**1**	**2**	**3**	**4**	**5**	**6**	**7**	**8**	**9**
caster trail $\boldsymbol{e}$ $[\boldsymbol{mm}]$	0	0	0	20	20	20	50	50	50
scrub radius $\boldsymbol{r_c}$ $[\boldsymbol{mm}]$	0	20	50	0	20	50	0	20	50
$\boldsymbol{F_z = 700}$ $[\boldsymbol{N}]$	48	52	66	52	55	69	66	25	81
$\boldsymbol{F_z = 800}$ $[\boldsymbol{N}]$	59	63	81	63	67	84	81	63	99
$\boldsymbol{F_z = 900}$ $[\boldsymbol{N}]$	70	75	97	75	88	101	97	69	118

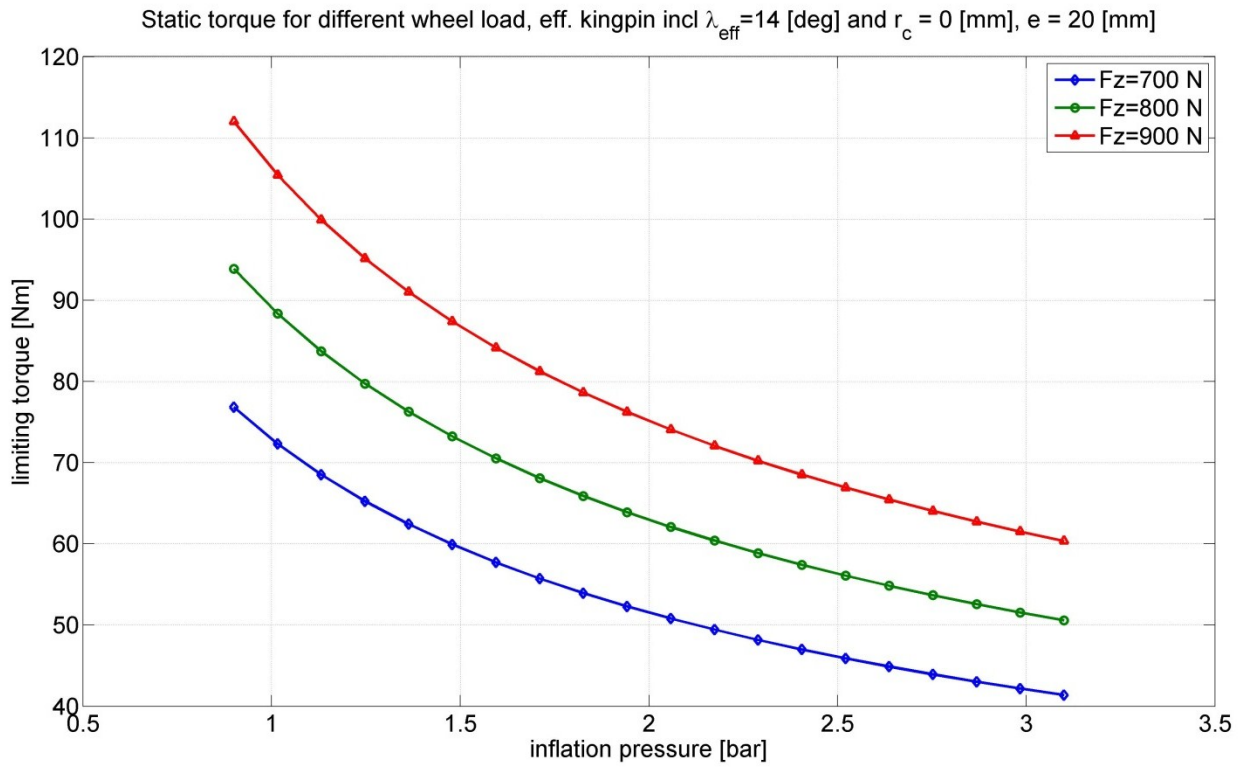

Figure 17. Results of static torque prediction for both free rolling wheels with $e = 20\ mm$

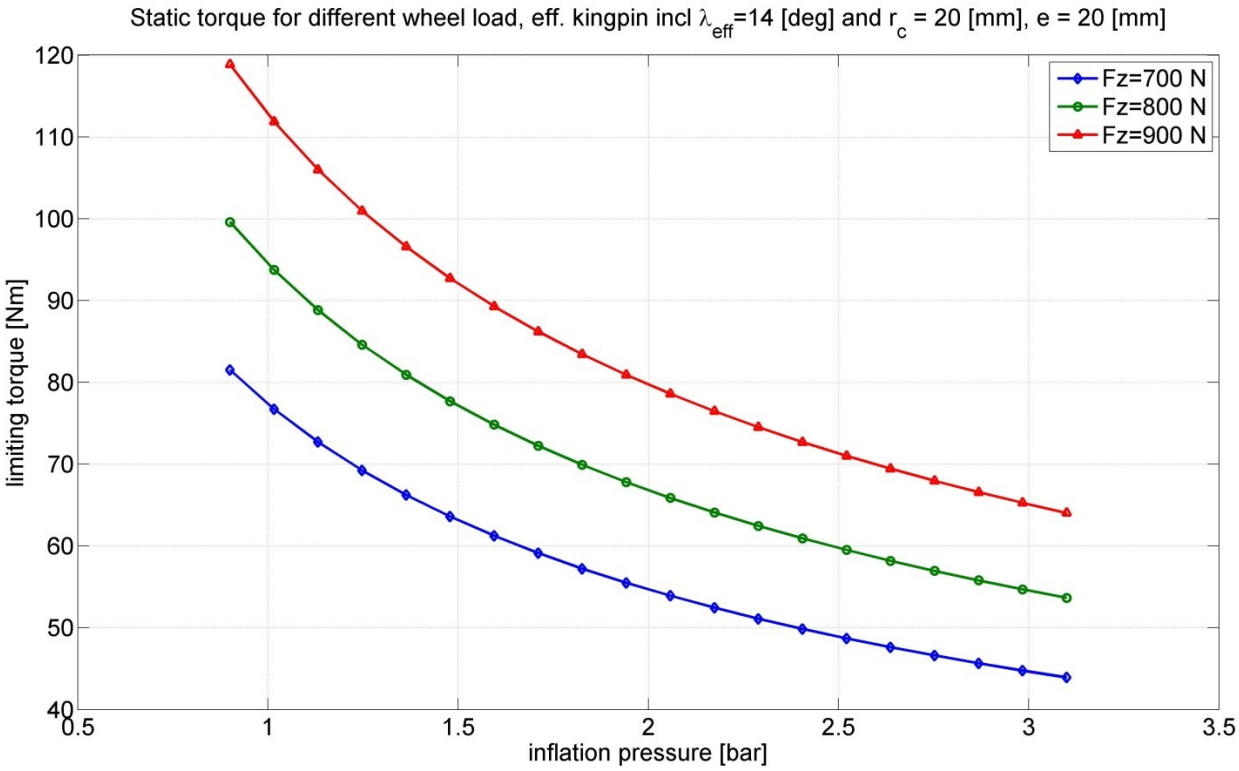

Figure 18. Results of static torque prediction for both locked wheels with $e = r_c = 20\ mm$

3.4 Lateral tire forces at high speed

The biggest difference between high speed and low speed scenarios is the influence of lateral acceleration a_y on tire forces. In high speed driving the force necessary to maintain equilibrium state of the wheel to (stationary conditions with constant wheel angle $\delta = const.$) is the greatest. The spin torque decreases with increased speed due to increase of relaxation length. Of course, dynamic (non-stationary) conditions play a major role for defining the dynamic steering actuator forces necessary for a certain reaction time. However, for describing just the tire forces in high speed driving the stationary case is sufficient.

Longitudinal and lateral tire forces are mostly described by friction coefficient μ, which is a function of tire slip and is defined as tire force F_i over normal load F_n, which is shown in (3-14). The tire slip s is defined as tire slip velocity v_i over tire peripheral speed $r_D|\Omega|$ (3-15).

$$\mu_x = \mu_x(s_x) = \frac{F_x}{F_n} \qquad \mu_y = \mu_y(s_y) = \frac{F_y}{F_n} \tag{3-14}$$

$$s_x = \frac{v_x}{r_D|\Omega|} \qquad s_y = \frac{-v_y}{r_D|\Omega|} = \sin\alpha \tag{3-15}$$

Lateral slip is usually expressed with slip angle α. Figure 19 shows a typical µ-slip-curve for longitudinal tire force.

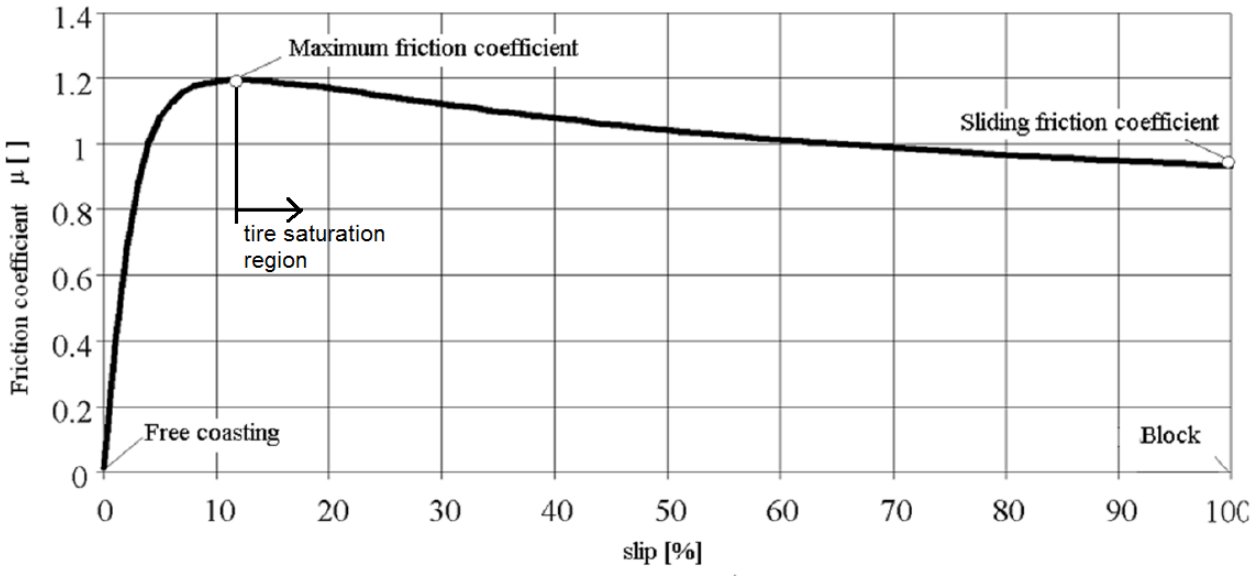

Figure 19. μ-slip-curve, modified from [2]

The curve shape for lateral tire force is slightly different, but the characteristic is the same. The tire force reaches its maximum at comparably low slip and then decreases with further slip increase. The zone after maximum tire friction is referred to as tire saturation zone, since the tire saturates and is not able to build up greater tire force.

For the purpose of simplification the µ-slip-curve for lateral tire force is often linearized in the zone below peak friction. This is by introducing cornering stiffness $C_{F\alpha}$ so that lateral tire force $F_{y,w}$ can be expressed as function slip angle α (3-16). The cornering stiffness is only valid for small slip angles (3-17).

$$F_{y,w} = C_{F\alpha}\,\alpha \tag{3-16}$$

$$C_{F\alpha} = \left.\frac{F_y}{\alpha}\right|_{\alpha<1°} \tag{3-17}$$

For high speed driving it is often only of interest to analyze vehicle behavior at small slip angles only until maximum tire force and, hence, the μ-slip-curve is linearized in that region. The cornering stiffness $C_{F\alpha}$ is defined as the gradient of the μ-slip-curve at zero. In the upcoming sections we will use the cornering stiffness to describe lateral tire force.

Brush tire model

For the estimation of performance requirements of the steering actuators for the EDV we are interested in a simple tire model, which allows us to estimate peak forces and velocities. For this purpose, no complex thermo-mechanical or FEM tire model is necessary. Besides that, it is extremely difficult and expensive to acquire precise tire data from the manufacturers. Thus, the decision was taken to use the so-called brush tire model based on physical macro-scale, which requires longitudinal and lateral stiffness only and some assumption on geometric dimensions of the contact patch, as has been done already in the creep-speed evaluation. Formulas and picture of the standard tire brush model in the following are taken from Paceijka [10].

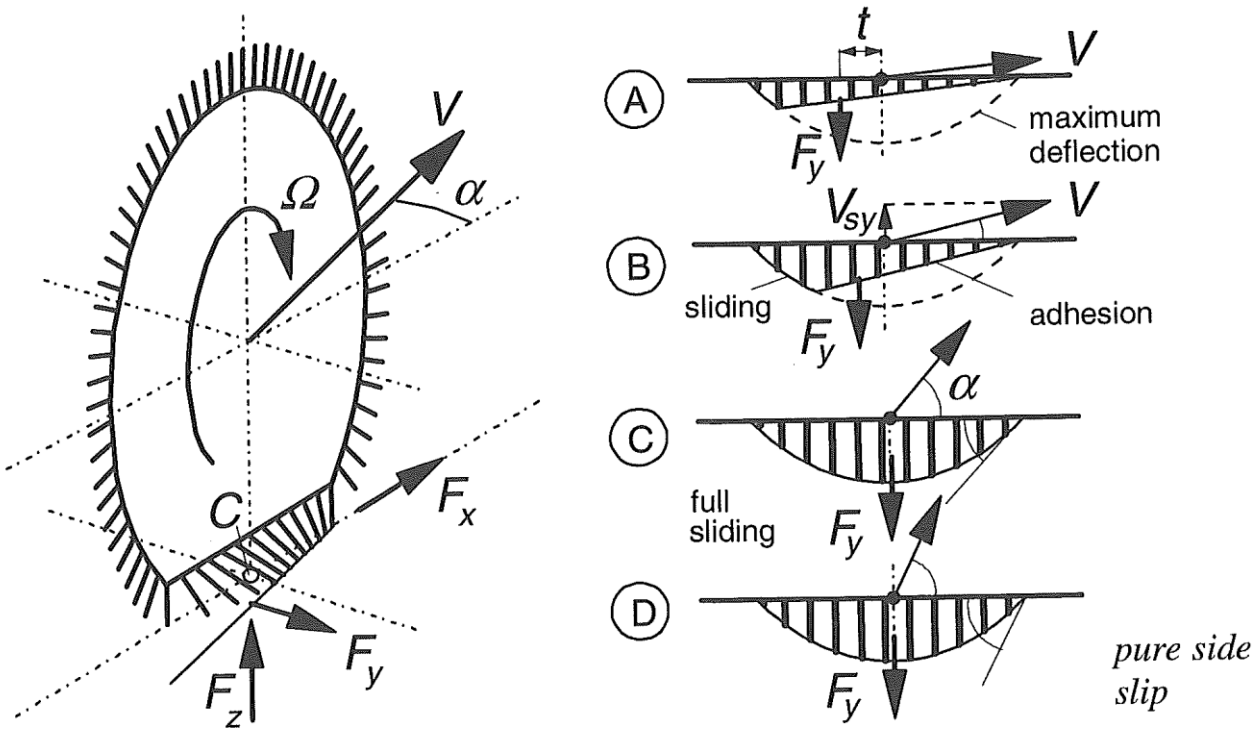

Figure 20. Brush model principle (pure side slip), from [10]

The brush tire model describes the tire as a circular row of elastic bristles, which when touching the road plane, deflect in a direction parallel to the road surface (see left-hand side Figure 20). The basic principle is that it differentiates between an adhesion region and a sliding region of the contact patch. In the adhesion region maximum deflection is not reached yet and friction force still increases linearly with increased deflection. In the sliding region maximum deflection is already reached and a further increase of tire force is not possible due to physical capacity of the tire. The brush model assumes the pressure distribution over the contact patch and, thus, the maximum deflection v_{max} to vary according to a parabola. Starting with the rear part of the contact patch to slide (case A right-hand side of Figure 20), the sliding region will increase with increasing longitudinal slip σ_x or side slip α until the tire is finally saturated and the total contact patch slides (case D right-hand side of Figure 20).

Brush model for pure lateral slip

Since we're mainly interested in lateral tire force F_y due to mayor impact on kingpin moment in high-speed, we will focus first on the pure side slip case. In Figure 21 the maximum possible lateral deformation $v_{max} = q_{y,max}/c_{py}$ is indicated, with lateral force distribution q_y and lateral stiffness c_{py}.

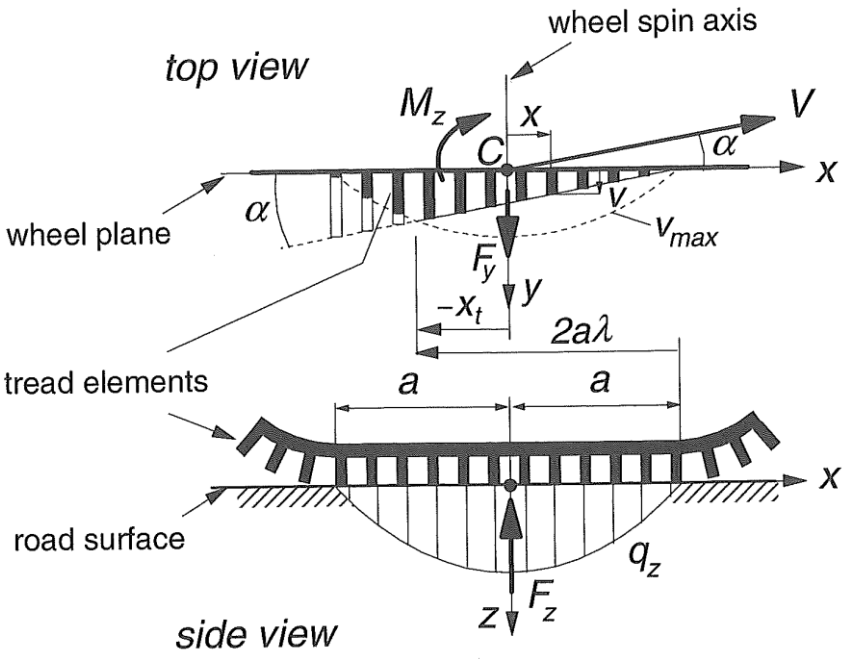

Figure 21. Brush model moving at pure side slip, from [10]

With the lateral stiffness c_{py} of the tread elements per unit length and lateral deformation v for vanishing sliding $\alpha \to 0$ and $\mu \to \infty$ (3-18), one can define cornering force F_y (3-19) and self-aligning torque M_z (3-20) and consequently cornering stiffness $C_{F\alpha}$ (3-21) and aligning stiffness $C_{M\alpha}$ (3-22).

$$v = (a - x)\, tan\, \alpha \tag{3-18}$$

$$F_y = c_{py} \int_{-a}^{a} v\, dx = 2\, c_{py} a^2 \alpha \tag{3-19}$$

$$M_z = c_{py} \int_{-a}^{a} v\, x dx = -\frac{2}{3}\, c_{py} a^3 \alpha \tag{3-20}$$

$$C_{F\alpha} = \left(\frac{\partial F_y}{\partial \alpha}\right)_{\alpha=0} = 2\, c_{py} a^2 \tag{3-21}$$

$$C_{M\alpha} = -\left(\frac{\partial M_z}{\partial \alpha}\right)_{\alpha=0} = \frac{2}{3}\, c_{py} a^3 \tag{3-22}$$

For the case of finite μ and greater slip angle α, the sliding region will appear and the largest possible side force is limited. As mentioned before, the brush model assumes a parabolic distribution of the vertical force per unit length q_z (3-23) and, hence, the largest possible side force distribution $q_{y,max}$ (3-24).

$$q_z = \frac{3F_z}{4a} \cdot \left\{1 - \left(\frac{x}{a}\right)^2\right\} \quad 3\text{-}23$$

$$\left|q_{y,max}\right| = \mu\, q_z = \frac{3}{4}\mu F_z \frac{(a^2 - x^2)}{a^3} \quad 3\text{-}24$$

The brush model now differentiates between the adhesion and sliding region by defining the point x_t at which the deflection of the adhesion region becomes equal to that of the sliding region. The equation are normalized by introducing the composite tire model parameter θ_y. By introducing the variable λ, by using equation equilibrium at $x = x_t$ (3-18, 3-23, 3-25) the slip angle α_{sl} at which total sliding starts ($\lambda = 0$) can be defined (3-27).

$$\theta_y = \frac{2c_{py}a^2}{3\mu F_z} \quad 3\text{-}25$$

$$\lambda = 1 - \theta_y |\tan\alpha| \quad 3\text{-}26$$

$$\tan\alpha_{sl} = \frac{1}{\theta_y} \quad 3\text{-}27$$

From there, using $\sigma_y = \tan\alpha$ for the side slip, cornering force F_y (3-28), aligning torque M_z (3-29) and pneumatic trail t (3-30) can be defined. The pneumatic trail for vanishing slip (3-19, 3-20) is given by $t = t_0 = -\left(M_z/F_y\right)_{\alpha\to 0} = (1/3)\, a$. Pacejka [10] adds, that the introduction of an elastic carcass will more likely improve this value to $t \approx 0.5a$.

$$F_y = \begin{cases} \mu F_z\,(1-\lambda^3)\; sgn\,\alpha = 3\,\mu F_z \theta_y \sigma_y \left\{1 - \left|\theta_y\sigma_y\right| + \frac{1}{3}\left(\theta_y\sigma_y\right)^2\right\} & (|\alpha| \le \alpha_{sl}) \\ \mu F_z\; sgn\,\alpha & (\alpha_{sl} \le |\alpha| \le \pi/2) \end{cases} \quad 3\text{-}28$$

$$M_z = \begin{cases} -\mu F_z \lambda^3 a\,(1-\lambda)\; sgn\,\alpha = \\ -\mu F_z a\;\theta_y\sigma_y \left\{1 - 3\left|\theta_y\sigma_y\right| + 3\left(\theta_y\sigma_y\right)^2 - \left|\theta_y\sigma_y\right|^3\right\} & (|\alpha| \le \alpha_{sl}) \\ 0 & (\alpha_{sl} \le |\alpha| \le \pi/2) \end{cases} \quad 3\text{-}29$$

$$t = \begin{cases} -\frac{M_z}{F_y} = \frac{1}{3}a \frac{1 - 3\left|\theta_y\sigma_y\right| + 3\left(\theta_y\sigma_y\right)^2 - \left|\theta_y\sigma_y\right|^3}{1 - \left|\theta_y\sigma_y\right| + \frac{1}{3}\left(\theta_y\sigma_y\right)^2} & (|\alpha| \le \alpha_{sl}) \\ 0 & (\alpha_{sl} \le |\alpha| \le \pi/2) \end{cases} \quad 3\text{-}30$$

From equation 3-29 the peak value $M_{z,max}$ (3-31) can be found.

$$M_{z,max} = \left(\frac{27}{256}\right) a\mu\, F_z \quad (\text{at } \sigma_y = \tfrac{1}{4\theta_y}) \quad 3\text{-}31$$

This value is of interest for the sizing of steering actuators for the EDV. Due to normalizing, those results can be generalized and applied to the EDV tires by defining wheel load F_z, contact patch length $2a$ composite tire model parameter θ_y and friction coefficient μ. The lateral stiffness c_{py} can be defined by a given cornering stiffness using equation 3-21. Pacejka [10] uses the correlation 3-32 between contact patch and vertical load, based on the assumption that 2a changes by the power of two with radial tire deflection ρ and the linear dependency to wheel load $\rho \sim F_z$. Then the peak value $M_{z,max}$ can be written as (3-33).

$$a^2 = \frac{1}{3} F_z \times 10^{-5} \qquad 3\text{-}32$$

$$M_{z,max} = \left(\frac{9\sqrt{3}}{256}\right) \mu \, {F_z}^{1.5} \times 10^{-5/2} \qquad 3\text{-}33$$

Comparing the maximum alignment torque $M_{z,max}$ with the static torque $T_{stat,2\ bar}$ for 2 bar inflation pressure from equation 3-8, we can see that the estimated magnitude of alignment torque is about one third of the static torque magnitude (3-34).

$$\frac{T_{stat,2\ bar}}{M_{z,max}} \approx \frac{256}{81} = 3.27 \qquad 3\text{-}34$$

Pacejka itself states and shows experimentally, that the magnitude of the tire brush model is at about four fifth of the actual self-alignment torque $|M_{z,max}| \approx \frac{4}{5} \cdot |M_{z,meas}|$ [10]. Comparing with real tire measurements available from the website of Avonracing (compare [11] and APPENDIX D), which have been accomplished for formula student racing tires with wheel load $m_w = 150 - 350\ kg$, we can see that the calculated relative magnitude $|M_{z,max}|$ in is ~70 % of magnitude of those measurements.

Figure 22 shows the graphical representation of side force, aligning torque and pneumatic trail characteristic as function of slip angle.

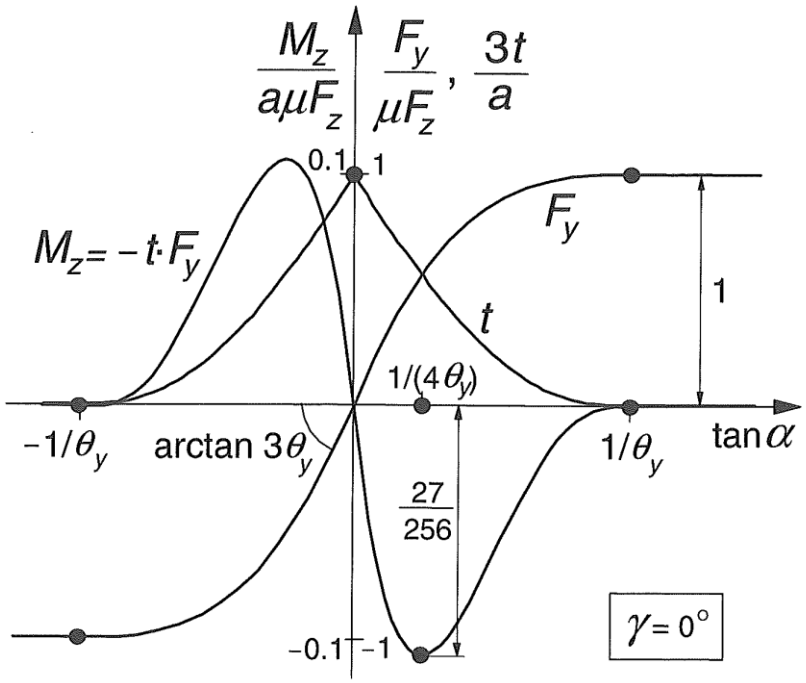

Figure 22: Brush model characteristics: side force, aligning torque and pneumatic trail vs. slip angle, from [10]

Taken into account that the measurements have been accomplished for slightly higher wheel loads and racing tires, which shown generally higher cornering stiffness, the values calculated below seem rather reasonable. However, as has been shown in equation 3-34, the maximum static torque will be greater than the expected maximum alignment torque so that the later one will be actuator dimension in terms of torque requirements. The calculations for slip angle and stiffness values are

based on tire brush model formulas and the cornering stiffness value for low wheel load tire from Nicholas D. Smith [3], which evaluated the used reference tire data from [11].

Table 6. Dynamic tire properties

Symbol	description	value
$\lvert M_{z,max}\rvert$	maximum alignment torque, single wheel $[Nm]$	8.7
$C_{M\alpha}\lvert_{\alpha=0}$	alignment torque stiffness $[Nm/rad]$	1950
$\lvert F_{y,max}\rvert$	maximum lateral force, single wheel $[N]$	1250
$C_{F\alpha}\lvert_{\alpha=0}$	cornering stiffness $[N/rad]$	37000 [3]
α_{sl}	slip angle at which enters saturation region $[deg]$	5.79
$\alpha_{max\,M}$	slip angle at maximum alignment torque $[deg]$	1.45
$\alpha_{max\,F}$	slip angle at maximum lateral force $[deg]$	5.79
$2a$	contact patch length $[m]$	0.105
μ	tire-to-road friction coefficient [-]	1.5
F_z	wheel load, $m_w = 85kg$ $[N]$	834

3.5 Influence of caster trail on self-alignment torque

The brush model for pure lateral slip, which has been presented above doesn't take into account the effect of mechanical trail e (caster). By assuming that the center of rotation of the tire coincides with the center of the tire on the contact patch, the alignment torque M_z becomes zero with pneumatic trail $t = 0$. However, the lateral force F_y is unequal to zero and a constant caster trail $e \neq 0$, which is independent of t still produces a moment about the kingpin axis. Moreover, F_y reaches its maximum for pneumatic trail $t = 0$ and, thus, can results in even higher torques.

Equation 3-35 shows the equation 3-30 for pneumatic trail t as a function of variable $\lambda = 1 - \theta_y|\tan\alpha|$. This equation can be extended by caster trail e (as a function of contact patch length $2a$), so that we end up with equation 3-36 for the effective lever arm t_e of the lateral force F_y.

$$t = -\frac{M_z}{F_y} = a\frac{\lambda^3(1-\lambda)}{(1-\lambda^3)} \tag{3-35}$$

$$t_e = t + e = a\left\{\frac{\lambda^3(1-\lambda)}{(1-\lambda^3)} + k\right\} = \frac{-a}{(1-\lambda^3)}\{\lambda^4 + (k-1)\lambda^3 - k\} \tag{3-36}$$

$$with\ e = k \cdot a$$

Consequently, the self-alignment torque can be now defined as in 3-37.

$$M_z = -F_y \cdot t_e = \mu a F_z(\lambda^4 - (1-k)\lambda^3 - k) \tag{3-37}$$

From there, maximum values can be defined using the derivative dM_z/dt (3-38 and 3-39).

$$\frac{dM_z}{dt} = \mu a F_z \lambda^2\big(4\lambda - 3(1-k)\big) \tag{3-38}$$

$$\frac{dM_z}{dt} = 0 \leftrightarrow \lambda_1 = \lambda_2 = 0 \quad \lambda_3 = \frac{3(1-k)}{4} \tag{3-39}$$

Equation 3-37 then can be expressed as function of slip angle α (3-40 and 3-41).

$$\sigma_{y,max} = |\tan \alpha_{max}| = \frac{1+3k}{4\theta_y} \qquad 3\text{-}40$$

$$|M_{z,max}| = \mu a F_z \left(\frac{27}{256}(1-k)^4 + k\right) \qquad 3\text{-}41$$

One can see, that for zero caster trail e $(k = 0)$ we end up with the original expressions $|M_{z,max}|$ and α_{max} (compare 3-31).

The plot in Figure 23 shows the effects of increasing caster trail e, which results in both, an increasing alignment torque M_z and the increment of α_{max}, at which maximum $M_{z,max}$ occurs.

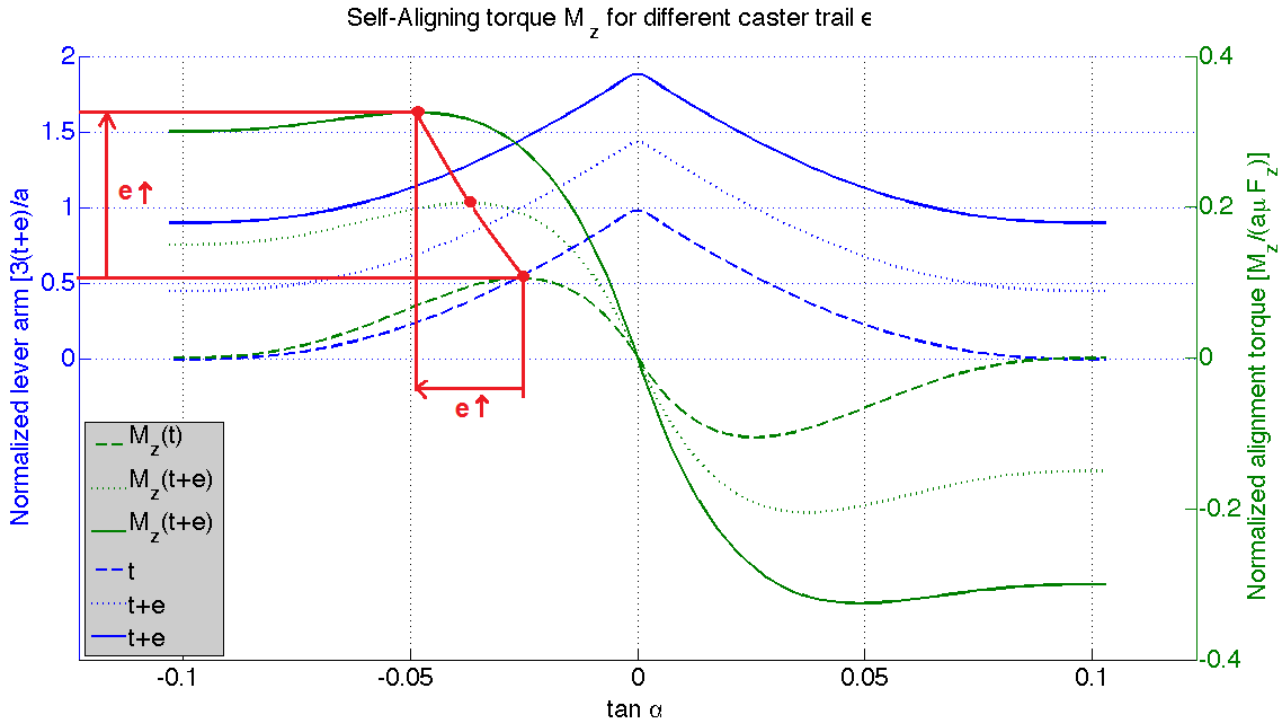

Figure 23. Normalized curves of self-alignment torque M_z and effective lever arm t_e for increasing caster trail e

Blue shows the normalized lever arm $[3t_e/a]$ and green the normalized alignment torque $[M_z/(a\mu F_z)]$. As reference, blue and green dashed lines show the curves of Figure 22 for zero caster trail.

Figure 24 on the next page shows the effect of increasing caster trail $e = 0 \cdots 50\ mm$ on the peak torque $|M_{z,max}|$ and the shift of α_{max} to higher slip angles in effective numbers. While peak torque changes nonlinear for small caster trail, α_{max} changes almost linear over the whole range. It can be seen that the impact of the consideration of caster trail is tremendous, which becomes obvious when we consider that pneumatic trail at $M_{z,max}(e = 0)$ is only $t_{max} = (27/148)a \approx 10\ mm$.

The maximum value for the caster trail is not randomly chosen. What we can see is, that for $e = 50\ mm$ the angle, at which the peak torque occurs, is $\alpha_{max} \approx 5.8\ deg$, which equals the tire saturation slip angle $\alpha_{max} = \alpha_{sl}$. This means, for higher values of caster, the alignment torque will still increase due to lever arm increment, but the tire force can't increase anymore so that the torque can't increase so much anymore. However, greater caster trail is strongly not recommended. For 13 inch tires 50 mm caster trail equals caster angle $\tau \approx 8.6\ deg$.

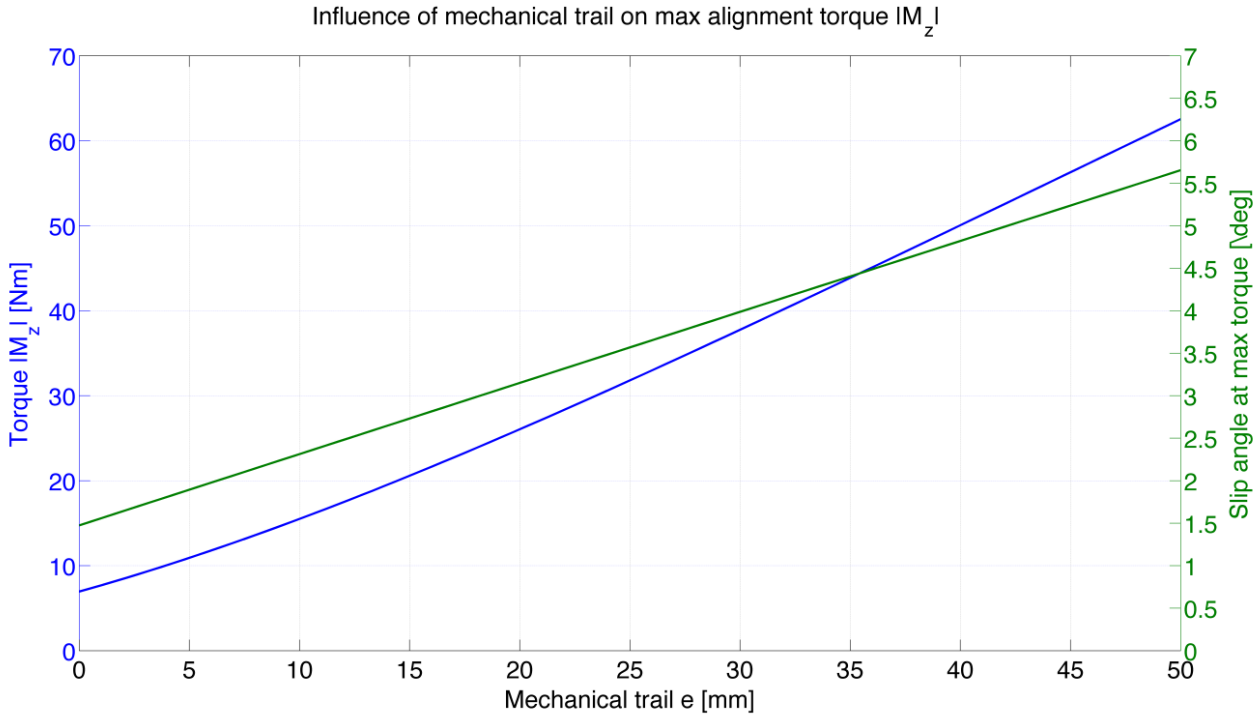

Figure 24. Maximum alignment torque $M_{z,max}$ as function of increasing caster trail e

Figure 25 shows exemplary the self-alignment torque as function of side slip angle for caster trail of $e = 20\ mm$.

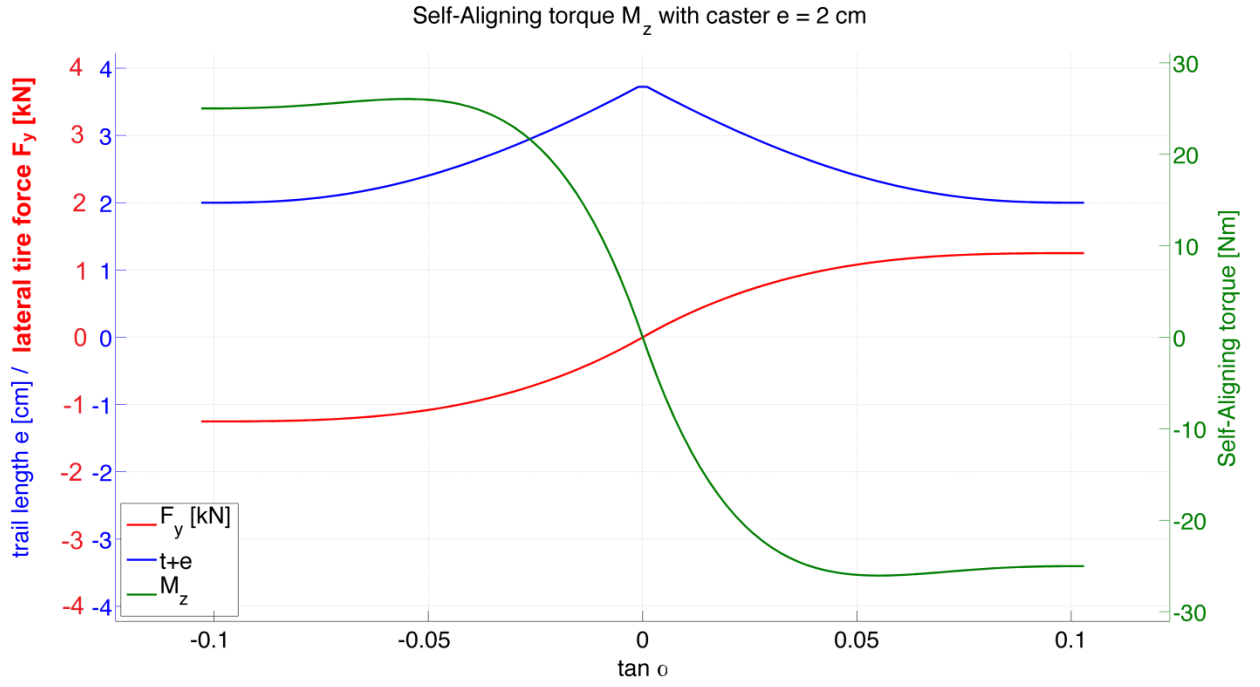

Figure 25. Self-alignment torque for caster e = 20 mm

3.6 Combined steering and braking

During combined steering and braking concurrently lateral forces and longitudinal braking force produce a moment about the kingpin axis. This can result in a reduction of the overall kingpin moment, but also result in the sum of both moments. This depends on the wheel side of the car and the steering direction, but also on the position of the kingpin axis, which defines whether a braking force produces a negative or positive kingpin moment. We will consider the "worst case" scenario at which both moments will sum up. For more information on this steering case, see also [2] and [12].

Equation 3-42 gives the summation of kingpin moment for one single wheel.

$$M_z = M_{z,x} + M_{z,y} = F_x r_c - F_y t_e \qquad 3\text{-}42$$

$$(F_x = F_{brake} < 0)$$

The kingpin moments will add up, the forces have different sign due to convention. In the combined steering and braking scenario are longitudinal force F_x and lateral force F_y dependent on each other. The combined resulting tire F_{res} can't be greater than the physical limitations of the tire (3-43).

$$F_{res} = \sqrt{F_x^2 + F_y^2} \leq \mu F_z \qquad 3\text{-}43$$

This effect is typically described by the Kamm friction circle in Figure 26.

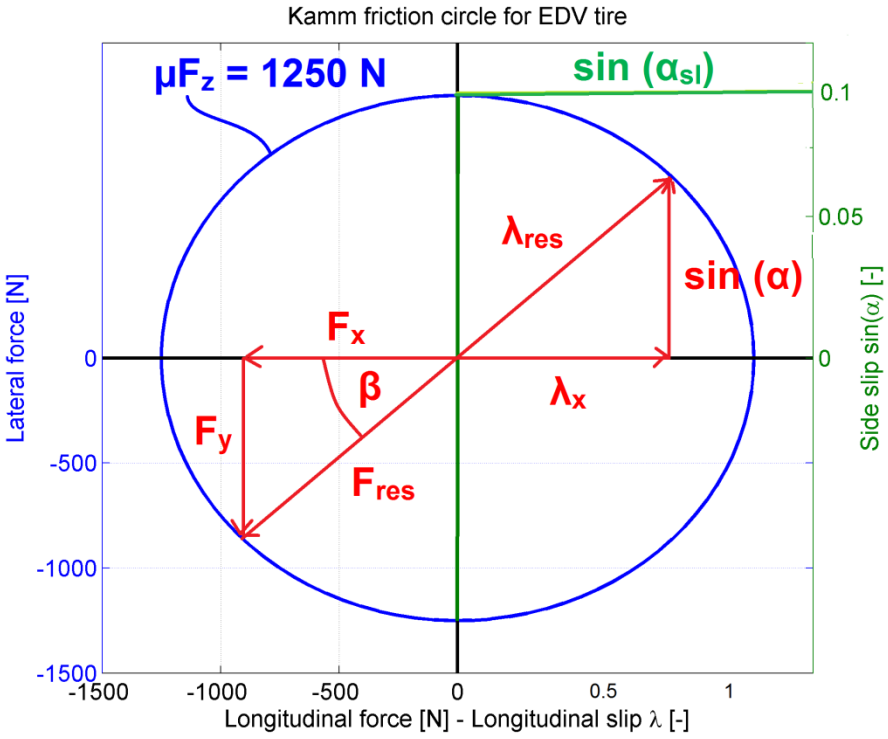

Figure 26. *Kamm friction circle for EDV car and tire*

The radius of the friction circle in Figure 26 can be shown normalized as one or can show the actual physical limitation of the tire $F_{tire,max} = \mu F_z = 1250\ N$ (for values of Table 6 on page 28). Both, slip vector λ_{res} and resulting force vector F_{res} can plotted as function of slip angle α (3-44 to 3-46).

$$\lambda_{res} = \sqrt{\lambda_x^2 + \sin^2 \alpha} \qquad 3\text{-}44$$

$$\tan\beta = \frac{\sin\alpha}{\lambda_x} = \frac{F_y}{F_x} \qquad 3\text{-}45$$

$$F_y = F_{res}\sin\beta \quad F_x = F_{res}\cos\beta \qquad 3\text{-}46$$

Measurements show that the relation between F_x and F_y is better described by a friction ellipse, but for the purpose of maximum steering forces the friction circle is sufficient since it just slightly overestimates the forces.

Using the friction circle one can also express the kingpin moment M_z as function of β (3-47).

$$M_z = M_{z,x} + M_{z,y} = F_x(\beta)\cdot r_c + F_y(\beta)\cdot t_e(\beta) \qquad 3\text{-}47$$

To achieve this one must also express lateral force lever arm $t_e = t(\alpha) + e$ as function of β, which changes due to the change of pneumatic trail t with slip angle α. For this purpose, equation 3-36 for t_e is linearized to change linear with $\tan\alpha$ and then for small angles $\tan\alpha \approx \alpha$ expressed as function of slip angle α (3-48).

$$t_e(\alpha) = e + t(\alpha) \approx ka + \frac{a}{3}\left[1 - \frac{\tan\alpha}{\tan\alpha_{sl}}\right] \approx ka + \frac{a}{3}\left[1 - \frac{\alpha}{\tan\alpha_{sl}}\right] \qquad 3\text{-}48$$

$$\sin\beta = \frac{\sin\alpha}{\sin\alpha_{sl}} \qquad 3\text{-}49$$

Using relation 3-49 between α and β, the lever arm t_e can then be expressed as function of β (3-50).

$$t_e(\beta) = e + t(\beta) = ka + \frac{a}{3}\left[1 - \frac{\sin\alpha_{sl}}{\tan\alpha_{sl}}|\sin\beta|\right] \qquad 3\text{-}50$$

Simulation shows a very close correlation function 3-50 with the function 3-36 for t_e of the brush model t_e becomes slightly overestimated, but since t can be comparibly small to e this doesn't take too much into account.

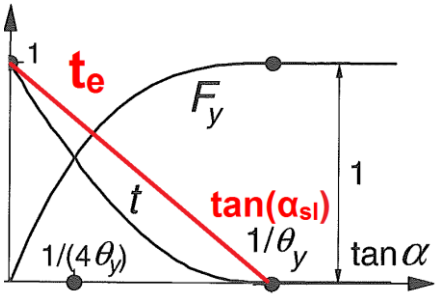

Figure 27. Linearization of lever armt_e

Figure 28 shows the results of the analysis of kingpin moment M_z for combined steering and braking, which has been done for different caster and kingpin angle setups.

The left-hand plot of Figure 28 shows $M_{z,x}$ plotted versus $M_{z,y}$, which makes it easy to evaluate kingpin moments on each wheel for different driving cases, such as right turn, left turn, traction, braking and their combinations. The right-hand plot shows the summation of both as function of β.

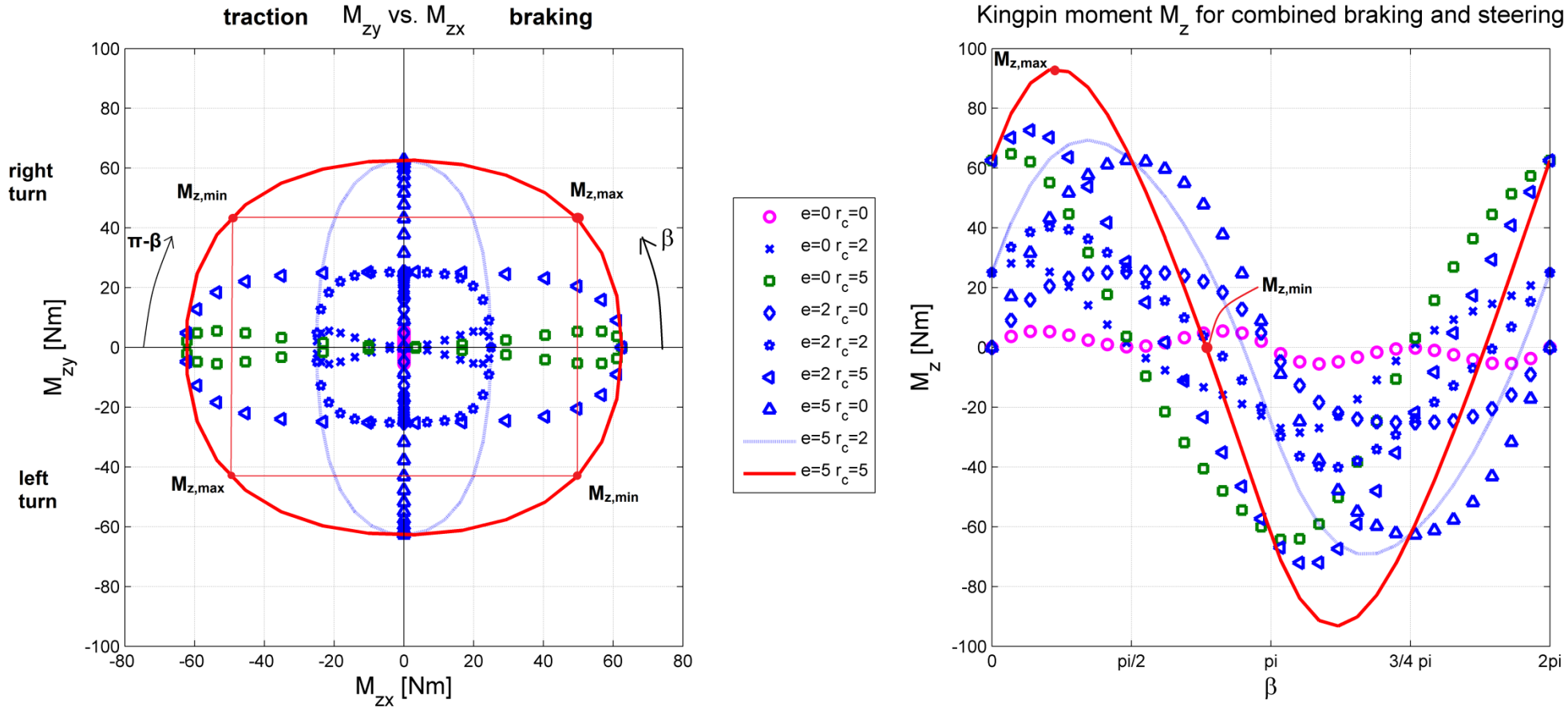

Figure 28. Results of steering torque effort in combined steering and braking for steered left wheel in ISO wheel coordinate system

The purple line (marked with 'o') shows kingpin moment for zero caster angle and zero scrub radius, which is different representation of standard alignment torque due to pneumatic trail only, presented in the previous chapter.

The plot gives results for nine different configurations with different caster trail e and scrub radius r_c, which are listed in Table 7.

Table 7. Combined steering and braking kingpin moment

Parameter \ Case	**1**	**2**	**3**	**4**	**5**	**6**	**7**	**8**	**9**
caster trail $\boldsymbol{e}$ $[\boldsymbol{mm}]$	0	0	0	20	20	20	50	50	50
scrub radius $\boldsymbol{r_c}$ $[\boldsymbol{mm}]$	0	20	50	0	20	50	0	20	50
$\lvert \boldsymbol{M_{z,x}} \rvert_{\boldsymbol{max}}$ $[\boldsymbol{Nm}]$	0	25	63	0	25	63	0	25	63
$\lvert \boldsymbol{M_{z,y}} \rvert_{\boldsymbol{max}}$ $[\boldsymbol{Nm}]$	6	5.5	5.5	25	25	25	63	63	63
$\lvert \boldsymbol{M_z} \rvert_{\boldsymbol{max}}$ $[\boldsymbol{Nm}]$	**6**	**28**	**65**	**25**	**40**	**73**	**63**	**69**	**93**

The results of Figure 28 and Table 7 show the kingpin moment for a single wheel only. Hence, for the evaluation of total steering torque we have to recall how left and right wheel influence each other. Due to symmetry longitudinal forces on left and right wheel are subtracted by each other, while lateral forces add up. The left-hand plot of Figure 28 shows the kingpin moment for the steered left wheel. For the steered right wheel braking and traction side are interchanged, like the mirror-inverted setup of the wheels. This can be easily adapted by setting variable $\beta_{in} = \pi - \beta_{out}$.

From there it can be shown (equation 3-51 to 3-58) that maximum steering torque $M_{z,max} \leq 2\lvert M_{z,single\ wheel} \rvert$, even for μ-split-braking situations (3-58) due to simultaneous decrease of $M_{z,y}$ and increase of $M_{z,x}$ with $dM_{z,x}(\beta,\mu)/d\mu \leq dM_{z,y}(\beta,\mu)/d\mu$ (for all β).

$$M_z = M_{z,in} + M_{z,out} \tag{3-51}$$

$$M_{z,x} = M_{z,x}(\beta) + M_{z,x}(\pi-\beta) = \mu_{in} F_z \cos\beta \cdot r_c + \mu_{out} F_z \cos(\pi-\beta) \cdot r_c \tag{3-52}$$

$$\begin{aligned} M_{z,y} &= M_{z,y}(\beta) + M_{z,y}(\pi-\beta) \\ &= \mu_{in} F_z \sin\beta \cdot t_e(\sin\beta) + \mu_{out} F_z \sin(\pi-\beta) \cdot t_e(\sin(\pi-\beta)) \end{aligned} \tag{3-53}$$

$$\cos(\beta) = -\cos(\pi-\beta) \qquad \sin(\beta) = \sin(\pi-\beta) \tag{3-54}$$

$$M_{z,x}(\beta) = (\mu_{in} - \mu_{out}) \cdot F_z \cos\beta \cdot r_c \tag{3-55}$$

$$M_{z,y}(\beta) = (\mu_{in} + \mu_{out}) \cdot F_z \sin\beta \cdot t_e(\beta) \tag{3-56}$$

$$\Rightarrow \boldsymbol{M_{z,max} = 2\lvert M_{z,single\ wheel} \rvert} \qquad (\boldsymbol{\mu_{in} = \mu_{out}}) \tag{3-57}$$

$$\begin{aligned} \Rightarrow \boldsymbol{M_{z,max}} &= \boldsymbol{\Delta\mu \cdot F_z \cos\beta \cdot r_c + (2\mu - \Delta\mu) \cdot F_z \sin\beta \cdot t_e(\beta)} \\ &\leq \boldsymbol{2\lvert M_{z,single\ wheel} \rvert} \quad (\boldsymbol{\mu_{in} \neq \mu_{out}}) \end{aligned} \tag{3-58}$$

Table 8. Overall steering torque for combined steering and braking incl. both wheels

Parameter \ Case	**1**	**2**	**3**	**4**	**5**	**6**	**7**	**8**	**9**
$\lvert \boldsymbol{M_{z,x}} \rvert_{\boldsymbol{max}}$ $[\boldsymbol{Nm}]$	0	25	63	0	25	63	0	25	63
$\lvert \boldsymbol{M_{z,y}} \rvert_{\boldsymbol{max}}$ $[\boldsymbol{Nm}]$	6	5.5	5.5	25	25	25	63	63	63
$\lvert \boldsymbol{M_z} \rvert_{\boldsymbol{max}}$ $[\boldsymbol{Nm}]$	**6**	**30.5**	**68.5**	**25**	**50**	**88**	**63**	**88**	**126**

3.7 Vertical wheel load and jacking torque

The vertical wheel load has to effects on the steering effort. On the one side it defines the longitudinal and lateral tire forces and on the other side produces it a kingpin moment $T_{w,z}$. The equation for kingpin moment $T_{w,z}$ has been already developed in chapter 2 (equation 2-27) and depends in comparison to the moment of longitudinal and lateral forces also on steering angle δ (3-59).

$$T_{w,z} = \left(F_{z,fl} + F_{z,fr}\right)(r_c \tan\sigma - e\tan\tau)\sin\delta\cos\lambda + \left(F_{z,fl} - F_{zf,r}\right)(r_c \tan\tau + e\tan\sigma)\cos\delta\cos\lambda \quad \text{3-59}$$

For symmetric load ($F_{z,fl} = F_{z,r}$) and driving ($\delta = 0$) case kingpin moment $T_{w,z}$ will be zero (3-60).

$$T_{w,z}\left(F_{z,fl} = F_{z,fr};\ \delta = 0\right) = 0 \quad \text{3-60}$$

The same applies for zero caster trail and zero scrub radius (3-61). Hence, the static load case can be neglected.

$$T_{w,z}(r_c = e = 0) = 0 \quad \text{3-61}$$

The greatest wheel load F_z occurs for dynamic conditions anyways. Defining those dynamic wheel forces is rather difficult, since it depends a lot on the suspension setup and the wheel weight. At this stage of the project the decision for components has not been finalized yet, which makes even more difficult. Also the considered driving scenario is important.

Generally, high vertical wheel loads occur during driving on bumpy roads. Peak forces occur when the car gets excited in its natural frequency, which leads to resonance and high acceleration and wheel load. Thus, hitting a single bump is a dimensioning driving scenario due to the wide frequency spectrum of the impulse like input. Estimating maximum vertical forces is described more in detail in APPENDIX A, in which the vertical dynamics analysis is performed. Vertical forces on the wheel can be considerably greater than those in longitudinal and lateral direction. The analysis showed that vertical forces up to $F_{z,max} \approx 10\ kN$ can be reached, which is in the same range as values stated in literature. A common thumb-rule is $F_{z,max} \approx 3.5\ VGW$ [1].

For high speed driving equation 3-59 can be simplified by setting steering angle $\delta = 0$, so that we get equation 3-62.

$$T_{w,z} = \left(F_{z,fl} - F_{z,fr}\right)(r_c \tan\tau + e\tan\sigma)\cos\lambda \quad \text{3-62}$$

For maximum torque a single-sided bump occurrence is considered with $F_{z,fl} = 10\ kN$ and $F_{z,fr} = 0$. Again, the same nine different configurations as in the previous section are considered.

In case of $M_{z,z}$ it is worth considering a negative scrub radius setup, since this can reduce the torque amplitude a lot. Hence, one should notice that in this case it's is not recommended to have *zero-trail-setup*. Figure 29 shows graphically those results for the nine different suspension configurations.

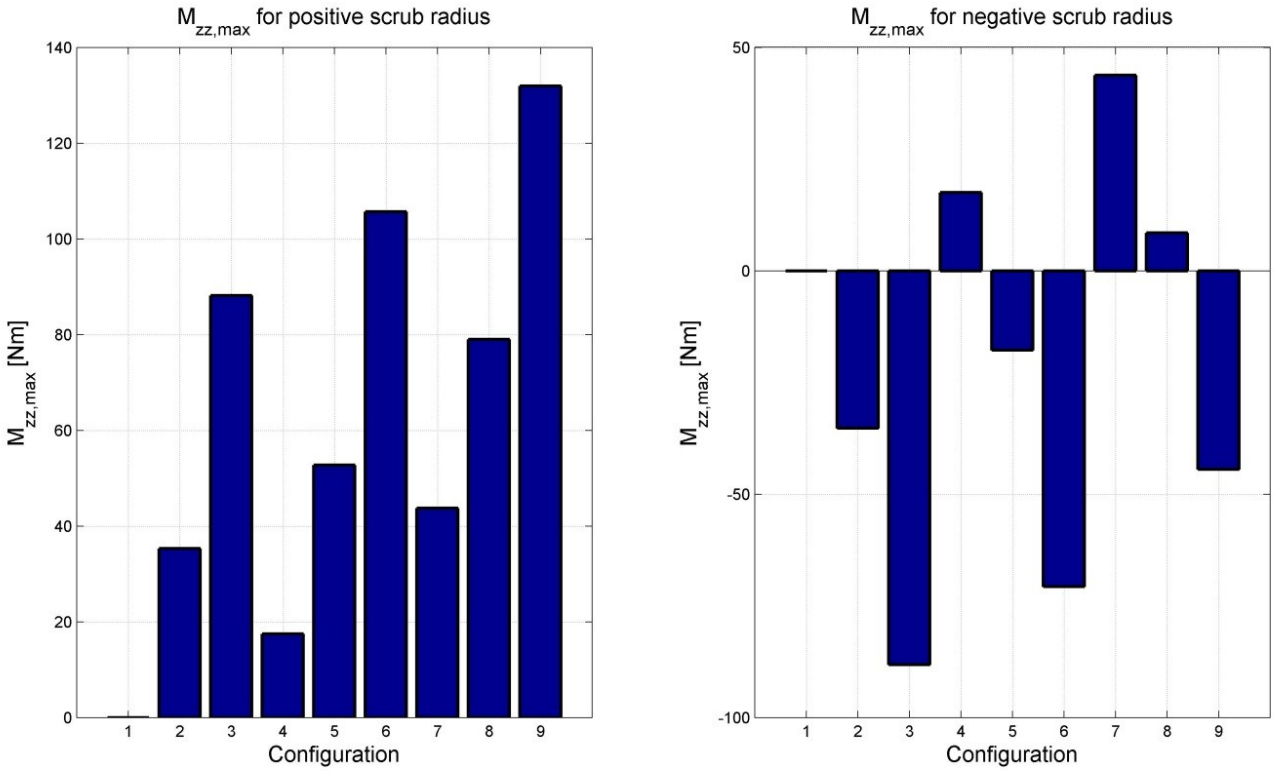

Figure 29. Kingpin moment $M_{z,z}$ due to vertical wheel forces

We can see that negative scrub radius r_c has considerable effect on the amplitude. Thus, a negative scrub radius is highly recommended. The numerical results are shown in Table 9.

Table 9. Overall steering torque for vertical force impact

Parameter	**1**	**2**	**3**	**4**	**5**	**6**	**7**	**8**	**9**
caster trail $\boldsymbol{e}$ $[\boldsymbol{mm}]$	0	0	0	20	20	20	50	50	50
scrub radius $\boldsymbol{r_c}$ $[\boldsymbol{mm}]$	0	20	50	0	20	50	0	20	50
$\boldsymbol{\lvert M_z \rvert_{max,}}$ $[\boldsymbol{Nm}]$	**0**	**35**	**88**	**17**	**53**	**106**	**44**	**79**	**132**
scrub radius $\boldsymbol{r_c}$ $[\boldsymbol{mm}]$	0	-20	-50	0	-20	-50	0	-20	-50
$\boldsymbol{\lvert M_z \rvert_{max,}}$ $[\boldsymbol{Nm}]$	**0**	**35**	**88**	**17**	**18**	**71**	**44**	**8**	**44**

3.8 Effects of vertical load transfer during cornering

Due to roll in high speed cornering vertical wheel load increases on outer wheels in same amount as it decreases on inner wheels, which leads at the same time to increase of tire force on outer wheel and decrease on inner wheel.

One can show, that this effect in terms of lateral tire forces doesn't increase steering effort, since cornering stiffness is linear proportional (for small F_z) to wheel load change. Thus, steering effort stays constant due to increase on outer wheel and decrease on the inside wheel. At higher wheel loads the relation between cornering stiffness and wheel load is nonlinear and, hence, steering effort even decreases (compare plots in APPENDIX C).

As has been shown before, steering effort due to longitudinal tire forces only occurs for different tire forces on left and right steered wheel. Thus, steering effort will increase with vertical load shift. However, one can show that this effect has less impact than the cases considered in the previous sections.

Same can be shown for vertical wheel impact. Since one-sided road disturbance with dynamic wheel load ($F_{z,max} \approx 3.5\ GVW!$) has been considered already, the impact of vertical load shift can be considered less.

3.9 Conclusions

The results of this analysis showed that the effect of suspension geometry has major impact on kingpin torque due to lateral, longitudinal and vertical tire forces. Static torque due to high spin torque requires generally greatest steering effort. However, due to combination of steering toque in high speed those forces can add up to even higher effort. Jacking torque can be quite high due to great vertical forces, but its amplitude can be reduced through negative scrub radius. Thus, this setup is strongly recommended.

For the modeling of steering control alignment torque can be modeled with different cornering stiffness $C_{F\alpha}$ $[\frac{N}{rad}]$ and alignment torque stiffness $C_{m\alpha}$ $[\frac{Nm}{rad}]$ for the evaluated suspension setups (refer to last rows of Table 10). In that case, the wheel torque changes linearly with increased slip angle. For spinning and jacking torque there is no slightly increase of kingpin moment, so that they can be modeled as steering step response.

4 Steering control

This chapter shows the design of the steering control system and which parameters that influence its performance.

4.1 General control design

In order to evaluate the power requirements of the steering actuator a steering control loop is necessary. Aim of the steering control is to make sure that time lag and amplitude difference in wheel angle δ is small. Hence, the wheel angle δ should follow the driver's steer intention, described with δ_{ref} as close as possible.

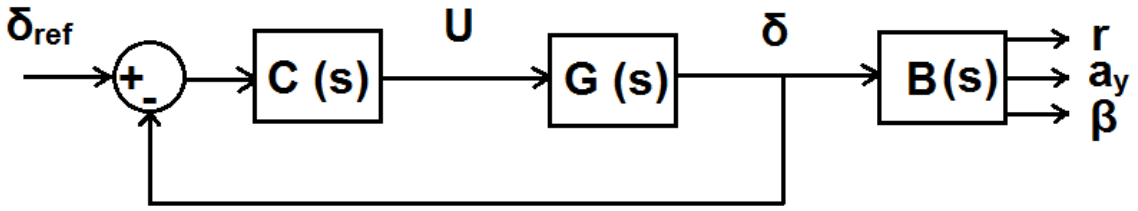

Figure 30. Steer-by-wire control system

Figure 30 shows the setup of the steer-by-wire control system, which can be described by two main transfer functions. $G(s)$ is the transfer function of the linearized electro-mechanical steering system, including steering actuator, rack-and-pinion system and tires, with actuator input voltage U and wheel angle δ as output. In control theory this transfer function is most often referred to as plant. $B(s)$ is the representation of the linearized bicycle model, which describes vehicle motion due to steered wheel angle input δ, with output yaw rate r, lateral acceleration a_y and slip angle β. $C(s)$ is the PID controller transfer function.

Equation 4-1 and 4-2 show the general expression for open- and closed-loop transfer function.

$$\left.\frac{\delta(s)}{\delta_{ref}(s)}\right|_{open} = C(s) \cdot G(s) \qquad 4\text{-}1$$

$$\left.\frac{\delta(s)}{\delta_{ref}(s)}\right|_{closed} = \frac{C(s) \cdot G(s)}{1 + C(s) \cdot G(s)} = T(s) \qquad 4\text{-}2$$

When designing the steering system one should make sure that the open-loop transfer function (4-1) already shows good frequency response behaviour, which can be achieved by choosing the right actuator with right gear and steering ratio. In this way one can reduce the overcompensation of the controller in the closed-loop (4-2).

The plant $G(s)$ can be subdivided into transfer function $G_1(s)$ of the electro-mechanical actuator system and $G_2(s)$ for the mechanical steering system (Figure 31).

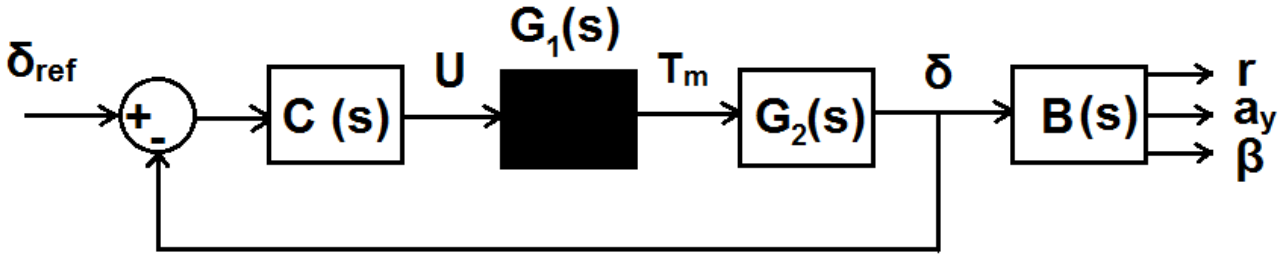

Figure 31. Steer-by-wire control system with unknown actuator transfer function

This separation is especially helpful since most manufactures present information about their actuators as black-box with the relation between input voltage U and output torque T_m. However, in the following sections the transfer function of the whole steering system will be developed to explain the influence of its parameters.

Obviously there is interaction between steering motion and vehicle motion $G(s) \Leftrightarrow B(s)$. For simplicity this interaction will be modeled in the following as inertia J_w, damping D_w and stiffness K_w of steering angle δ. With that simplification those subsystems can be handled more or less independent from each other. Using those parameters allows us to describe steering forces in driving scenarios, for which the bicycle model is not valid anymore.

4.2 Bicycle model transfer function $B(s)$

The bicycle model, also referred to as one-track model, represents a 2 DOF model of the car, in which the roll angle φ, pitch angle ϑ and their derivatives are set equal to zero. Thus, no vertical load shift due to roll or pitch is considered. The forward speed $u(\approx V)$ is assumed to be constant and the influence of the lateral component of the longitudinal forces F_{xi} is neglected. (compare [10] pages 23 ff.) The model has the following limitations:

1. limited to low frequency motion
2. only small deviations to undisturbed straight-ahead motion
3. slip angles are assumed to remain small enough to allow linearization of cornering characteristic

Figure 32 shows schematically all sizes, measures and motion parameters of the bicycle model.

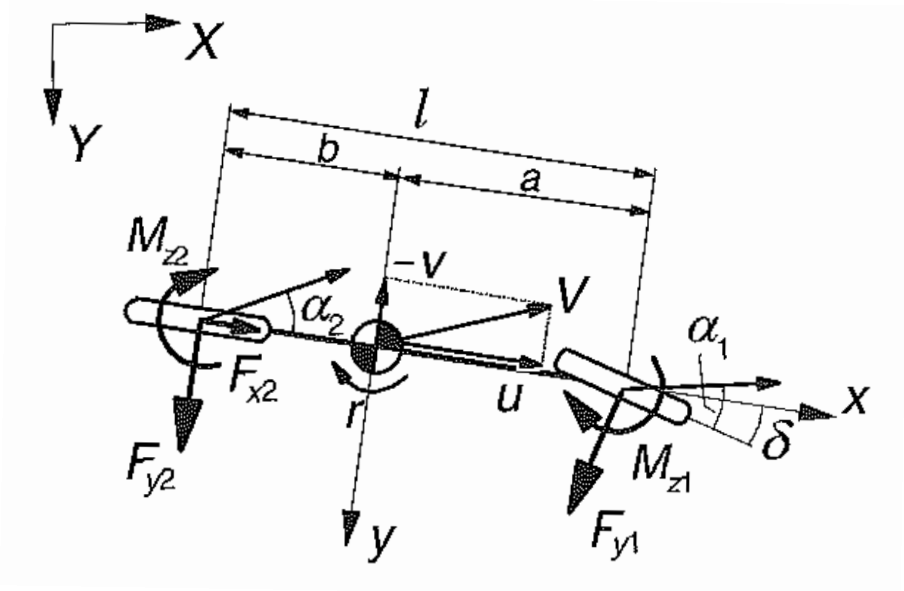

Figure 32. Bicycle model, from [10]

As been mentioned, the bicycle model is a linearized model so that the vehicle motion can be expressed by the equations 4-3, 4-4 and 4-5.

$$m(\dot{v} + ur) = F_{y1} + F_{y2} \qquad 4\text{-}3$$

$$m(\dot{u} - vr) = F_{x1} + F_{x2} \qquad 4\text{-}4$$

$$I\dot{r} = aF_{y1} - bF_{y2} \tag{4-5}$$

$$F_{yi} = C_i\alpha_i = C_{F\alpha i}\alpha_i \tag{4-6}$$

$$\alpha_1 = \delta - \beta - \frac{a\dot{r}}{u} = \delta - \frac{-v + a\dot{r}}{u} \qquad \alpha_2 = -\beta + \frac{b\dot{r}}{u} = \frac{v + b\dot{r}}{u} \tag{4-7}$$

The lateral forces in equation *4-3* and *4-5* are replaced by the expression *4-6*, introducing cornering stiffness C_i and lateral wheel slip angles α_i, leading to equation *4-8* and *4-9*.

(*4-6*) and (*4-3*):

$$m\dot{v} + \frac{1}{u}(C_1 + C_2)\, v + \left\{mu + \frac{1}{u}(aC_1 - bC_2)\right\} r = C_1\delta \tag{4-8}$$

$$I\dot{r} + \frac{1}{u}(a^2C_1 + b^2C_2)\, r + \frac{1}{u}(aC_1 - bC_2)\, v = aC_1\delta \tag{4-9}$$

By elimination of velocity v, one receives the second-order differential equation *4-10*.

(*4-8*) and (*4-9*):

$$\begin{aligned} Imu\,\ddot{r} + \{I(C_1 + C_2) + m(a^2C_1 + b^2C_2)\}\,\dot{r} \\ + \frac{1}{u}\{C_1C_2l^2 - mu^2(aC_1 - bC_2)\}\, r \\ = muaC_1\dot{\delta} + C_1C_2l\delta \end{aligned} \tag{4-10}$$

By introducing the terms *4-11* this can be further simplified to *4-12*.

$$\begin{aligned} C &= C_1 + C_2 \\ C\bar{s} &= C_1a - C_2b \\ Cq^2 &= C_1a^2 + C_2b^2 \\ mk^2 &= I \end{aligned} \tag{4-11}$$

$$m^2k^2u^2\,\ddot{r} + muC(q^2 + k^2)\,\dot{r} + (C_1C_2l^2 - mu^2C\bar{s})\, r = mu^2\, aC_1\dot{\delta} + uC_1C_2l\delta \tag{4-12}$$

Accordingly, the linearized bicycle model is of the form (4-26) with parameter (4-32).

$$\Rightarrow M\ddot{r} + D\dot{r} + Kr = D_1\dot{\delta} + K_1\delta \tag{4-13}$$

$$M = \frac{m^2k^2u}{C_2}\left[\frac{Nms^3}{rad}\right] \quad D = m\frac{C}{C_2}(k^2 + q^2)\left[\frac{Nms^2}{rad}\right] \quad K = \frac{1}{u}\left(C_1l^2 - mu^2\frac{C\bar{s}}{C_2}\right)\left[\frac{Nms}{rad}\right]$$

$$K_1 = C_1l\ [Nm/rad] \qquad D_1 = mua\frac{C_1}{C_2}\ [Nms/rad] \tag{4-14}$$

From there, the transfer function $B_1(s)$ (4-15) with K_1 and D_1 for yaw rate r can be directly received. Transfer functions $B_2(s)$ for a_y and $B_3(s)$ for β are given by *4-16* and *4-17*, whose parameter M_2, D_2, K_2, D_3 and K_3 are implemented more easily with a state-space model in Matlab.

$$B_1(s) = \frac{r(s)}{\delta(s)} = \frac{D_1s + K_1}{Ms^2 + Ds + K} \tag{4-15}$$

$$B_2(s) = \frac{a_y(s)}{\delta(s)} = \frac{M_2s^2 + D_2s + K_2}{Ms^2 + Ds + K} \tag{4-16}$$

$$B_3(s) = \frac{\beta(s)}{\delta(s)} = \frac{D_3 s + K_3}{Ms^2 + Ds + K} \qquad 4\text{-}17$$

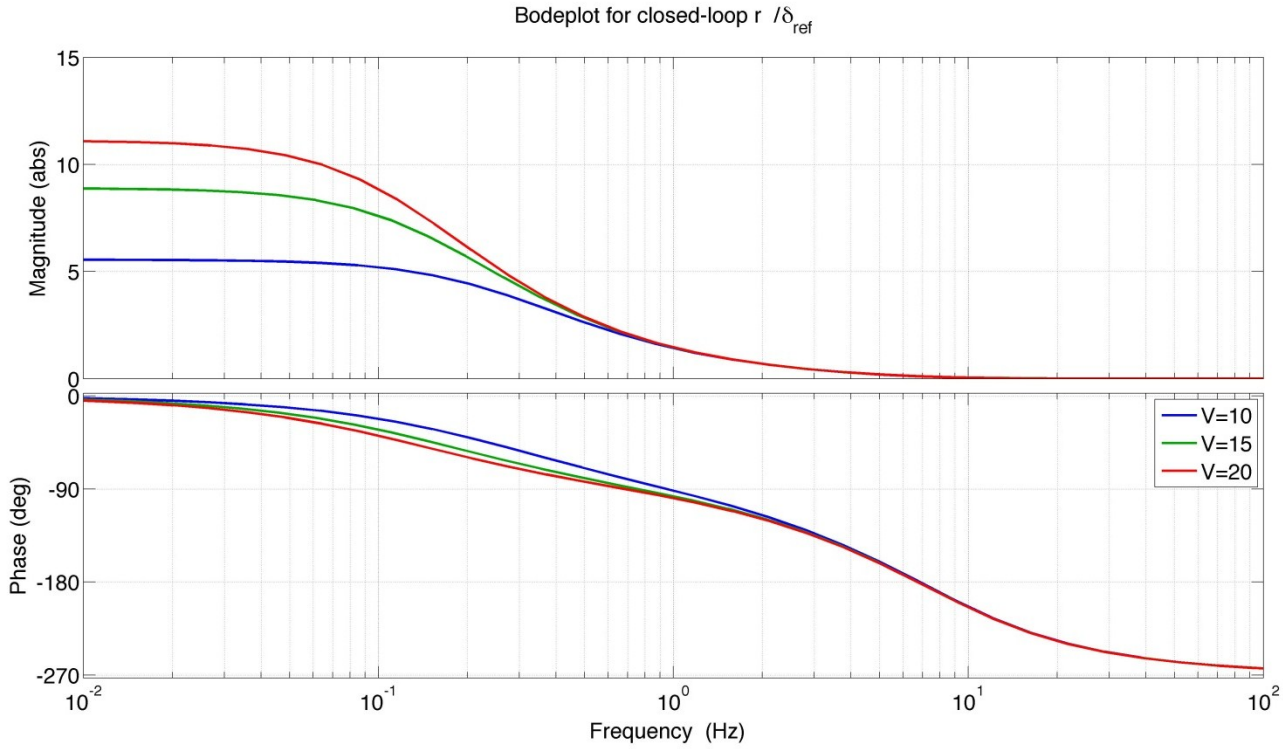

Figure 33. Bode plot of bicycle model transfer function $B_1(s)$ for yaw rate r for velocities $V = 10\ ^m/_s$, $V = 15\ ^m/_s$ and $V = 20\ ^m/_s$ and understeer coefficient $\eta = 0$

From the relation between steering angle δ and front slip angle α_1 in *4-7*, the transfer function 4-19 can be calculated using the bicycle transfer function *4-15* to *4-17*.

$$\frac{\alpha_1(s)}{\delta(s)} = 1 - B_3(s) - \frac{a}{V} s B_1(s) \qquad 4\text{-}18$$

$$\frac{\alpha_1(s)}{\delta(s)} = \frac{\left(M - \frac{a}{V} D_1\right) s^2 + \left(D - \frac{a}{V} K_1 - D_3\right) s + (K - K_3)}{Ms^2 + Ds + K} \qquad 4\text{-}19$$

Figure 34 shows the frequency response behavior of α_1 for the neutrally steered EDV vehicle ($\eta = 0$). One can see, that the amplitude of front slip angle α_1 strongly depends on the vehicle velocity and frequency of steering angle δ. Furthermore we can see, that for low frequencies and low speed the slip angle can be even greater than steering angle due to a negative slip angle β.

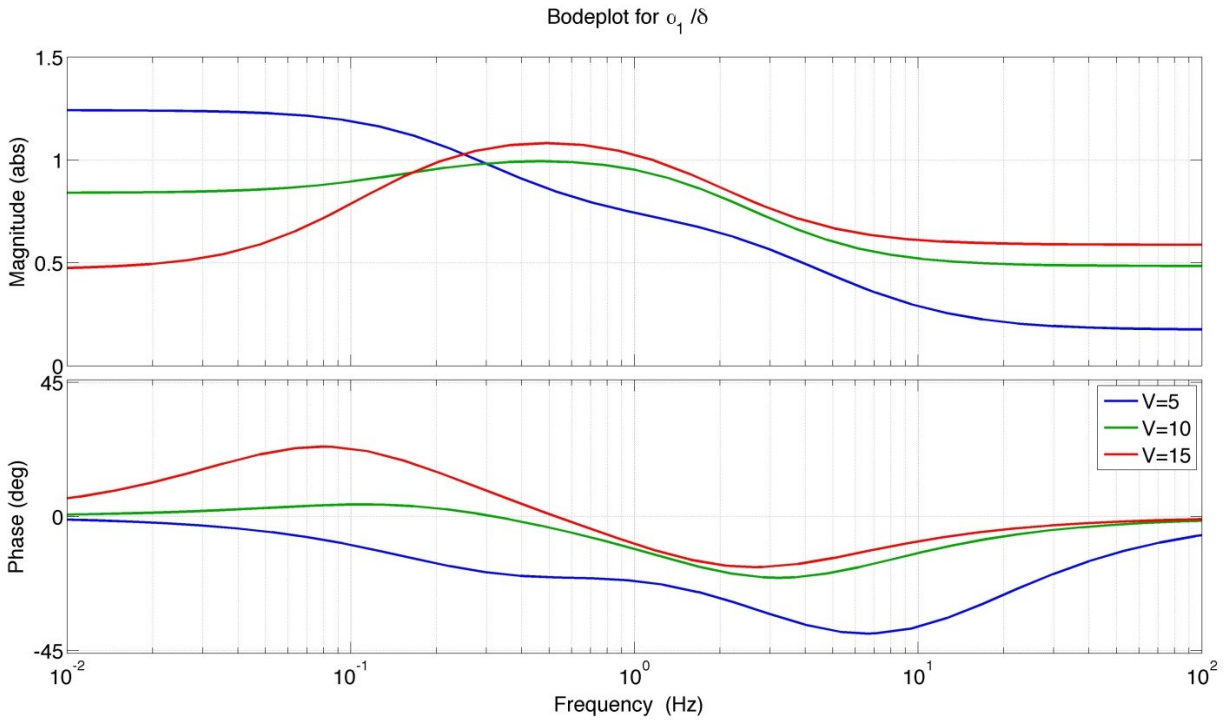

Figure 34. Bode plot for front slip angle transfer function $\alpha_1(s)/\delta(s)$

As mentioned previous, for simplicity we will handle vehicle motion and steering motion independent from each other. Since we are interested in great slip angles between 1-2 Hz for maximum tire forces, which are likely to occur at higher speeds, we can see from Figure 34 that it is a good approximation to assume slip angle equals steer angle (*4-20*).

$$\delta(s) = \alpha_1(s) \tag{4-20}$$

With that simplification we can describe the load torque T_L of steering system $G(s)$ as function of inertia J_w, damping D_w and stiffness K_w of steering angle δ.

4.3 Steering system transfer function $G(s)$

The equations 4-21 to 4-25 show the four basic equation of a DC motor for rotor mechanics (4-21), electrical circuit (4-22), motor torque (4-23) and back EMF (4-22). Equations taken from [13].

$$J_r\ddot{\theta}_r + d_r\dot{\theta}_r = T_M - T_L \tag{4-21}$$

$$L\frac{di}{dt} + i\,R = U - U_{ind} = U - k_m\omega_r \tag{4-22}$$

$$T_M = k_e\,i \tag{4-23}$$

$$U_{ind} = k_m\omega_r \tag{4-24}$$

$$k = k_E = k_M = BlrN \tag{4-25}$$

The load torque T_L in (4-26) is defined by inertia J_w, damping D_w and stiffness K_w for turning the wheels. The stiffness K_w (4-27) is direct outcome of the detailed force analysis in chapter 3 with torque stiffness $C_{m\alpha}$ as function of wheel load, pneumatic and mechanical trail.

$$J_r\ddot{\theta}_r + d_r\dot{\theta}_r = T_M \underbrace{-\frac{J_w}{r_g r_s}\ddot{\delta} - \frac{D_w}{r_g r_s}\dot{\delta} - \frac{K_w}{r_g r_s}\delta}_{-T_L} \quad 4\text{-}26$$

$$K_w = 2C_{m\alpha}(F_z, e, t)\cos\lambda \left[\frac{Nm}{rad}\right] \quad 4\text{-}27$$

$$D_w = 225^{1}\cos\lambda \left[\frac{Nms}{rad}\right] \quad 4\text{-}28$$

$$J_w = 5^{2}\cos\lambda \left[\frac{Nms^2}{rad}\right] \quad 4\text{-}29$$

One can show that damping D_w (4-28) is more influenced by damping of the rack-and-pinion-system, especially the bearings and knuckles. Thus, the influence of suspension geometry on damping is negligible. The value is based on the assumption of a similar project with steer-by-wire car performed at Stanford University [4]. This value is most likely to be smaller for the EDV due to smaller tire and simpler steering system, so that with this assumption load torque $T_L$will be overestimated. Same applies for lumped inertia J_w (4-29) of rack and wheels about the steering axis.

Since cornering stiffness $C_{F\alpha}$ is strictly speaking only valid for slip angles $\alpha < 1°$, we will define at this point the cornering stiffness slightly different to calculate $C_{m\alpha}$, so that it builds up maximum lateral tire force more precise (4-30). Otherwise maximum tire forces would be overestimated.

$$C_{F\alpha} = \left.\frac{F_{y,max}}{\alpha_{max}}\right|_{\alpha \le \alpha_{max}} \quad 4\text{-}30$$

Rotor inertia and damping can be lumped together with load torque (4-31) with the constant relation between rotor angle θ_r and wheel angle δ (4-32) so that we end up with a second-order equation for the mechanical part of the steering system (4-33).

$$\underbrace{\left(J_r + \frac{J_w}{(r_g r_s)^2}\right)}_{\overline{J_r}}\ddot{\theta}_r + \underbrace{\left(d_r + \frac{D_w}{(r_g r_s)^2}\right)}_{\overline{d_r}}\dot{\theta}_r + \underbrace{\left(\frac{K_w}{(r_g r_s)^2}\right)}_{\overline{k_r}}\theta_r = T_M \quad 4\text{-}31$$

$$\theta_r = r_g r_s\,\delta \quad 4\text{-}32$$

$$\overline{J_r}\,\ddot{\theta}_r + \overline{d_r}\,\dot{\theta}_r + \overline{k_r}\,\theta_r = k_e\,i \quad 4\text{-}33$$

Integrating mechanical circuit (4-33) and electrical circuit (4-22) in (4-34) and (4-35) we receive the transfer function for rotor speed ω_r over voltage input for the actuator (4-36).

$$(\overline{J_r}\,s^2 + \overline{D_r}\,s + \overline{K_r})\,\theta_r(s) = K\,I(s) \quad 4\text{-}34$$

[1] rack and tire damping about kingpin axis, value based on estimations made in [2], [15], [16], see also section 4.5

[2] rack and tire inertia about kingpin axis, value based on estimations made in [2], [15], [16], see also section 4.5

$$(Ls + R)I(s) = U(s) - Ks\theta_r(s) \quad 4\text{-}35$$

$$\frac{\omega_r(s)}{U(s)} = \frac{Ks}{(\overline{J_r}s^2 + \overline{D_r}s + \overline{K_r})(Ls + R) + K^2 s} \quad 4\text{-}36$$

By integrating we receive the transfer function for rotor angle θ_r over DC motor voltage U (4-38).

$$\frac{\theta_r(s)}{U(s)} = \frac{1}{s} \cdot \frac{\omega_r(s)}{U(s)} = \frac{K}{(\overline{J_r}s^2 + \overline{D_r}s + \overline{K_r})(Ls + R) + K^2 s} \quad 4\text{-}37$$

$$\frac{\theta_r(s)}{U(s)} = \frac{K\,\overline{J_r}\,L}{s^3 + \left(\frac{R}{L} + \frac{\overline{D_r}}{\overline{J_r}}\right)s^2 + \left(\frac{R\overline{D_r}}{\overline{J_r}L} + \frac{\overline{K_r}}{\overline{J_r}} + \frac{K^2}{\overline{J_r}L}\right)s + \left(\frac{R\overline{K_r}}{\overline{J_r}\,L}\right)} \quad 4\text{-}38$$

We can see that the transfer function for rotor speed ω_r (4-36) is of second order. Since we need to control rotor angle θ_r to control the wheel angle δ a third-order transfer function is necessary (4-38).

From equation 4-35 and 4-34 also the transfer function for DC motor current I (4-39) and, hence, the actuator output torque T_m (4-40) can be calculated.

$$\frac{I(s)}{U(s)} = \frac{\overline{J_r}s^2 + \overline{D_r}s + \overline{K_r}}{(\overline{J_r}s^2 + \overline{D_r}s + \overline{K_r})(Ls + R) + K^2 s} \quad 4\text{-}39$$

$$\frac{T_m(s)}{U(s)} = \frac{K\,(\overline{J_r}s^2 + \overline{D_r}s + \overline{K_r})}{(\overline{J_r}s^2 + \overline{D_r}s + \overline{K_r})(Ls + R) + K^2 s} \quad 4\text{-}40$$

Since the rack-and-pinion system is set to be rigid and, hence, linear relation between rotor and wheel angle can be assumed, the open-loop transfer function $G(s)$ (4-42) is of third order.

$$G(s) = \frac{\theta_r(s)}{U(s)} \cdot \frac{\delta(s)}{\theta_r(s)} = \frac{\delta(s)}{U(s)} \quad 4\text{-}41$$

$$G(s) = \frac{\delta(s)}{\delta_{ref}(s)} = \frac{1}{(r_g r_s)} \cdot \frac{(K\overline{J_r}L)}{s^3 + \left(\frac{R}{L} + \frac{\overline{D_r}}{\overline{J_r}}\right)s^2 + \left(\frac{R\overline{D_r}}{\overline{J_r}L} + \frac{\overline{K_r}}{\overline{J_r}} + \frac{K^2}{\overline{J_r}L}\right)s + \left(\frac{R\overline{K_r}}{\overline{J_r}\,L}\right)} \quad 4\text{-}42$$

One has to design the systems parameter already in such a way, that the open-loop characteristic doesn't show too much phase lag (time lag). Equation 4-43 shows the phase equation of transfer function $G(s)$. The poles of $G(s)$ are given in 4-44, 4-45 and 4-46. The best way to guarantee stable behavior is to increase their critical frequencies of the poles so that they don't fall into the working range in order to decrease phase lag.

$$\varphi = \arctan\left[\frac{\omega^3 - (\overline{D_r}R + \overline{K_r}L + K^2)\omega}{\overline{K_r}R - (\overline{J_r}R + \overline{D_r}L)\omega^2}\right] \quad 4\text{-}43$$

$$\omega_1 = 0 \quad 4\text{-}44$$

$${\omega_2}^2 = \frac{\overline{K_r}R}{\overline{J_r}R + \overline{D_r}L} \quad 4\text{-}45$$

$$\omega_3{}^2 = \overline{D_r}R + \overline{K_r}L + K^2 \quad (4\text{-}46)$$

Some parameters are fixed, so and can't be influenced. But through the right choice for an actuator the electro-dynamic parameter can be chosen and mechanical parameter of the steering system can be influenced by steer ratio r_s and gear ratio r_g of the actuator.

4.4 Controller transfer function $C(s)$

The steering angle input from the driver is measured by a wheel angle sensor, whose output voltage is nearly linear to steering wheel angle input δ_{ref}. This output voltage is than amplified to control the actor angle. Common sensors have a linear accuracy error of $e_{lin} \approx 1.5\ \%$. The transfer function cutoff frequency of the electric sensor is high compared to the mechanical transfer function so that a linear behavior for relevant frequencies can be assumed (4-49).

$$\frac{U_s(s)}{\delta_{ref}(s)} = k_{s,linear} + k_{s,nonlinear}\, s \approx k_s \quad (4\text{-}47)$$

$$k_{s,nonlinear} \ll k_{s,linear} = k_s \quad (4\text{-}48)$$

$$\frac{U(s)}{\delta_{ref}(s)} = k_s \cdot k_{amp} \quad (4\text{-}49)$$

The sensor transfer function is integrated into the controller transfer function $C(s)$ (4-51) of a simple PID-controller. The control parameter are optimized to guarantee stable response behavior with low power requirements of the closed-loop $T(s)$ (4-52).

$$C(s) = \frac{U(s)}{\delta_{ref}(s)} \cdot PID\ (s) \quad (4\text{-}50)$$

$$C(s) = \left(k_s \cdot k_{amp}\right) \cdot \left(k_P + k_I \frac{1}{s} + k_D s\right) \quad (4\text{-}51)$$

$$T(s) = \frac{C(s) \cdot G(s)}{1 + C(s) \cdot G(s)} \quad (4\text{-}52)$$

4.5 Control and steering system parameter

Table 10 shows the parameter, for which the steering system has been optimized. The last rows show different aligning torque stiffness $C_{m\alpha}$ and corresponding cornering stiffness $C_{F\alpha}$ for different suspension geometry setups, which results from the analysis in chapter 3.

Table 10. Steering system parameter [4] [3]

Symbol	Description [unit]	Value		
r_s	steering ratio $[-]$	11		
r_g	gear ratio $[-]$	5		
J_{rot}	inertia of rotor $[kgm^2 = Nm\,s^2/rad]$	0.004		
J_{gear}	inertia of gear box about rotor shaft $[kgm^2]$	0.000145		
J_{coup}	inertia of coupling shaft $[kgm^2]$	0.002		
J_r	lumped inertia of rotor, gear box and coupling shaft $[kgm^2]$	0.0045		
J_w	lumped inertia of steering rack and wheels about steering axis $[kgm^2]$	5[3]		
D_r	rotor damping $[Nm\,s/rad]$	0.0000035		
D_w	rack and tire damping about steering axis $[Nm\,s/rad]$	225[4]		
r_{st}	steering arm about kingpin axis $[m]$	0.1		
R_{act}	internal resistance of DC motor $[\Omega]$	1.2		
L_{act}	actuator induction $[mH]$	9.5		
k_M	DC motor moment constant $[Nm/A]$	0.544		
k_E	DC motor voltage constant $[V/rad/s]$	0.544		
k_{amp}	voltage amplification factor $[-]$	47.4		
k_s	sensor voltage constant $[V/rad]$	1		
k_P	Controller proportional constant $[-]$	15.41		
k_D	Controller derivative constant $[-]$	0.25		
k_I	Controller integrative constant $[-]$	31.08		
μ	tire-to-ground friction coefficient $[-]$	1.5		
	Stiffness parameter for tire friction force	$e = 0\ mm$	$e = 20\ mm$	$e = 50\ mm$
$T_{a,max}$	maximum aligning torque $[Nm]$	6	25	63
$C_{m\alpha}$	aligning torque stiffness $[Nm/deg]$	229	448	634
$C_{F\alpha}$	cornering stiffness $[N/deg]$	45000	19000	12000

[3] The assumption of inertia of the steering system for steering shaft, rack- and pinion-system and wheels is based on estimations made in [4], [15] and [16]. In these papers control concepts for similar cars are presented, such cars equipped with a steer-by-wire system or electric power assisted steering. One can see that still for those similar concepts the estimations vary considerably. Since the EDV can be expected to have a rather simple steering system the mean value of those presented has been taken from Li LIU [15]. The exact estimation of this value for the EDV is not possible at this point, since the steering system is not designed yet. However, for precise steering control those parameter are crucial and it is advisable to identify them experimentally when the EDV is set up.

[4] For the damping of the steering system same estimations have been made as described above, based on assumptions from [4], [15] and [16].

5 Results

5.1 Tire torque in relevant scenarios

The results of this work are strongly focussed on the tire friction torque prediction in relevant driving scenarios. Hence, Table 11 to Table 13 show again the results of chapter 3, which focus on the influence of suspension geometry – as function of caster trail and scrub radius - on the friction force amplitude. Those results can be used for different suspension setups.

Table 11. Static torque prediction for $p = 2\ bar$

Parameter	1	2	3	4	5	6	7	8	9
caster trail $e\ [mm]$	0	0	0	20	20	20	50	50	50
scrub radius $r_c\ [mm]$	0	20	50	0	20	50	0	20	50
$F_z = 700\ [N]$	48	52	66	52	55	69	66	25	81
$F_z = 800\ [N]$	59	63	81	63	67	84	81	63	99
$F_z = 900\ [N]$	70	75	97	75	88	101	97	69	118

Table 12. Combined steering and braking kingpin moment

Parameter	1	2	3	4	5	6	7	8	9
caster trail $e\ [mm]$	0	0	0	20	20	20	50	50	50
scrub radius $r_c\ [mm]$	0	20	50	0	20	50	0	20	50
$\lvert M_{z,x}\rvert_{max}\ [Nm]$	0	25	63	0	25	63	0	25	63
$\lvert M_{z,y}\rvert_{max}\ [Nm]$	6	5.5	5.5	25	25	25	63	63	63
$\lvert M_z\rvert_{max}\ [Nm]$ (one wheel)	**6**	**28**	**65**	**25**	**40**	**73**	**63**	**69**	**93**
$\lvert M_z\rvert_{max}\ [Nm]$ (both wheels)	**6**	**30.5**	**68.5**	**25**	**50**	**88**	**63**	**88**	**126**

Table 13. Overall steering torque for vertical force impact

Parameter	1	2	3	4	5	6	7	8	9
caster trail $e\ [mm]$	0	0	0	20	20	20	50	50	50
scrub radius $r_c\ [mm]$	0	20	50	0	20	50	0	20	50
$\lvert M_z\rvert_{max,}\ [Nm]$ (both wheels)	**0**	**35**	**88**	**17**	**53**	**106**	**44**	**79**	**132**
scrub radius $r_c\ [mm]$	0	-20	-50	0	-20	-50	0	-20	-50
$\lvert M_z\rvert_{max,}\ [Nm]$ (both wheels)	**0**	**35**	**88**	**17**	**18**	**71**	**44**	**8**	**44**

Setup 5 with $e = r_c = 20\ mm$ in the tables above can be – from the current point of view – assumed to describe the suspension setup of the EDV the closest. Generally, the suspension geometry should be set up in such a way that scrub radius and caster trail are reduced as much as possible. However, certain variations due to construction tolerances have to be taken into account.

During vertical wheel motion suspension geometry and parameters can change slightly. This can be considered by assuming a certain variation of scrub radius and caster trail. Thus, from that perspective setup 5 is also favorable and will be considered from now on in the following results and discussion.

5.2 Actuator torque with steering control

The following results are restricted to one specific actuator setup only. The control system is optimized for the actuator described in Table 10. The table lists all parameter used for the following results. Especially the electro-dynamic power requirements can vary a lot depending on the chosen steering actuator. The simulation has been accomplished for setup 5, as described in the previous section.

Figure 35 shows the bode plot for the open-loop response $G(s)$ in comparison with the controlled closed-loop $T(s)$.

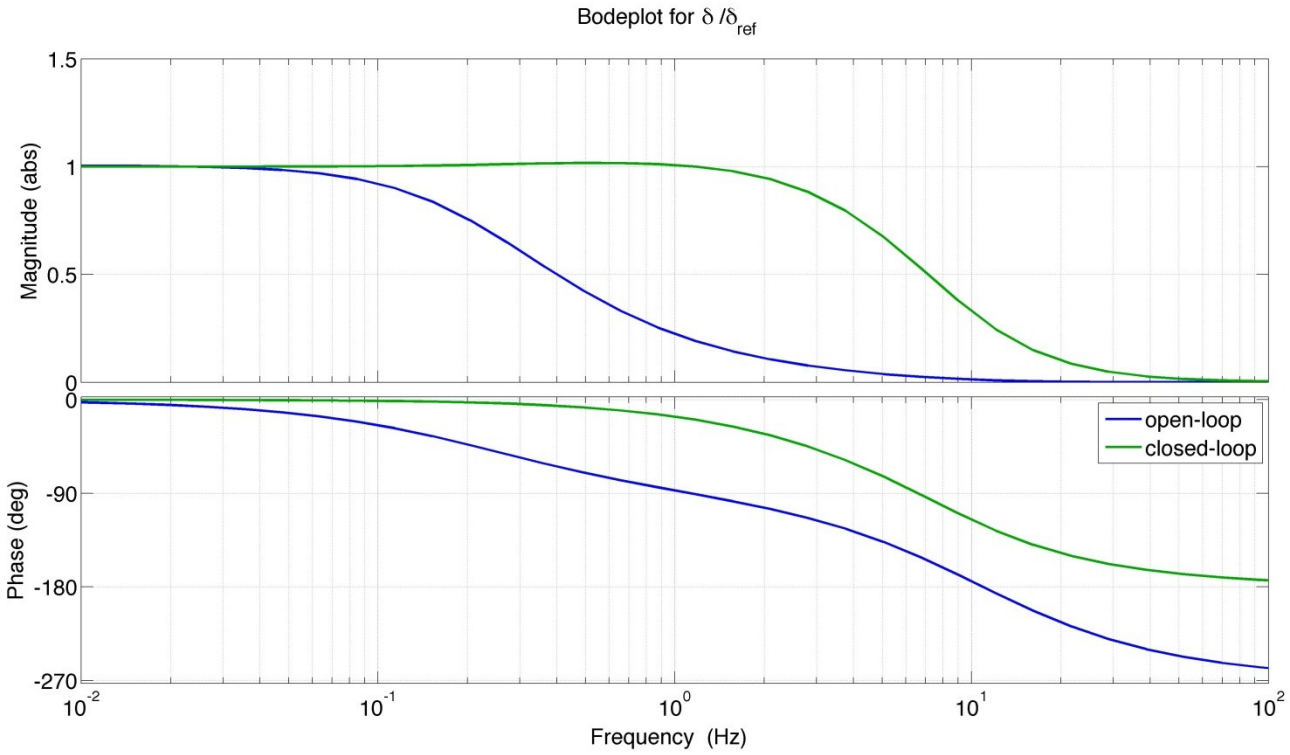

Figure 35. Bode plot for open-loop and closed-loop transfer function of $\frac{\delta(s)}{\delta_{ref}(s)}$

As been mentioned before, the open-loop of the steering system should already show good frequency response behaviour to reduce the required compensation effort of the closed-loop.We can see that the controller shifts the cut-off frequency to $f_c \approx 2.0\,Hz$ and reduces phase lag. The frequency $f_{max} = 2\,Hz$ has been set as critical frequency for the EDV, which is expected to be the maximum frequency of the driver input. For that frequency a phase lag of $\varphi_{max} = 34°$ could be achieved, which equals a time-lag of $t_{max} = 47\,ms$.

Figure 36 on the next page shows the frequency response of alignment torque for both wheels with mechanical trail of $e = 20\,mm$. One can see that dynamic wheel torque due to damping has considerable impact for frequencies $f > 1\,Hz$.

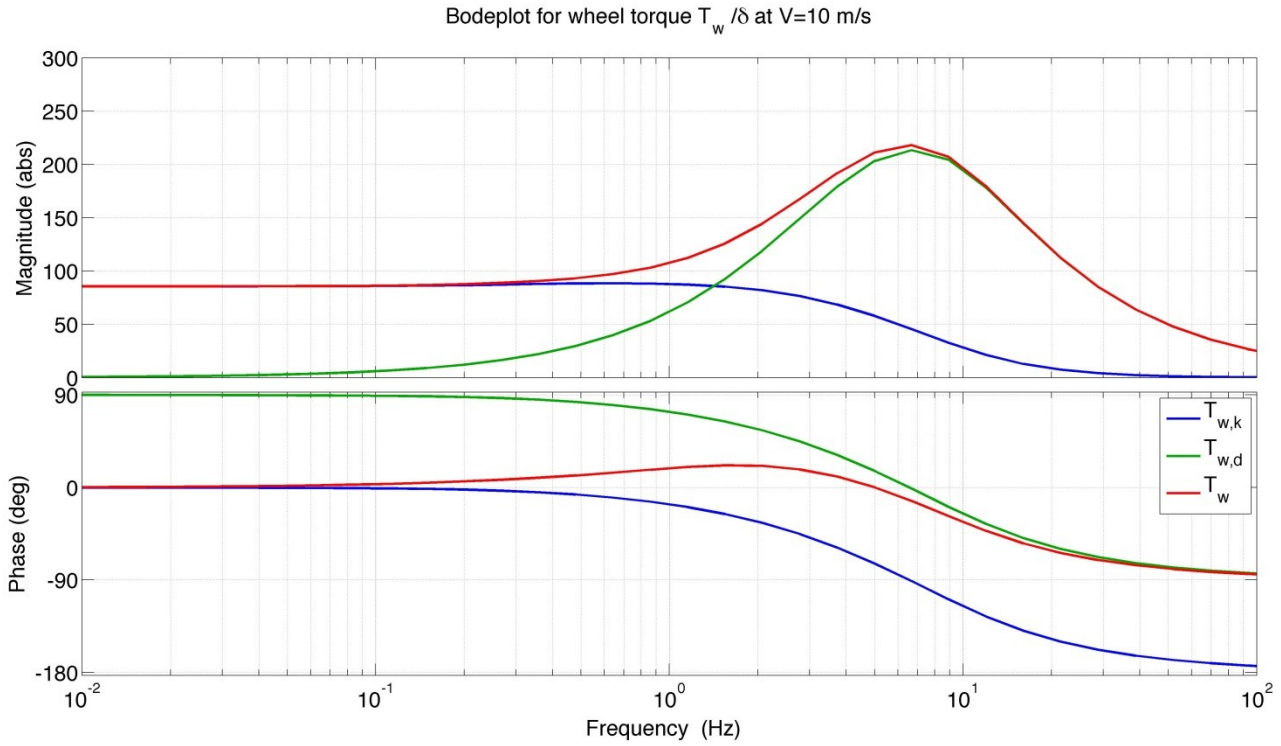

Figure 36. Bode plot of self-alignment torque on both wheel for mechanical trail e=20 mm

The red line in Figure 36 shows the overall wheel torque. The green line shows wheel torque due to damping and blue shows steering effort due to tire friction. We can see that the frequency response for friction forces (blue) is in accordance with the numerical results given in Table 11, Table 12 and Table 13. The friction torque in the closed-loop system decreases with increased frequency due to decreased steering angle amplitude, since the actuator is not able anymore to follow the required steering angle amplitude.

The plots on the following two pages show the time response behavior for the controlled system for sinusoidal steering input and steering step input.

Figure 37 shows the time response to a sinusoidal steering input with amplitude of $\delta = 6\,deg.$, the angle of maximum alignment torque for mechanical trail $e = 50\,mm$. As for a step response, in the beginning rather high torque and power is necessary to react to steering input. The steady-state requirements are lower than. The response behavior for small mechanical trail can be found in APPENDIX E.

Figure 38 shows the time response on a steering angle step. The steering input is modeled not as an ideal step, considering that the driver input will also take a certain amount of time to reach the final step value. As been mentioned before, the steering angle step can be also understood as static torque and jacking torque.

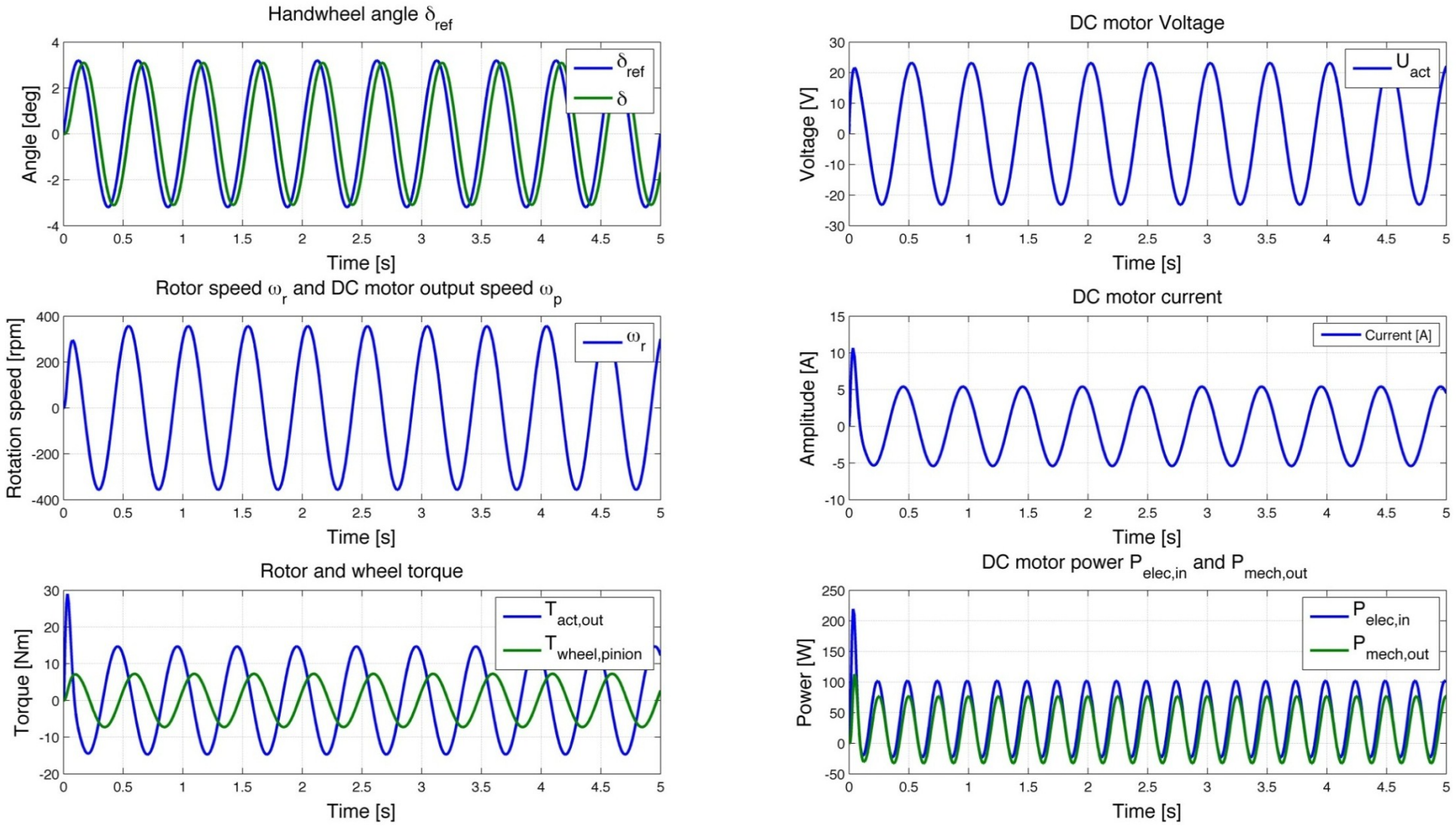

Figure 37. Time response for $f = 2\,Hz$ and $e = 20\,mm$

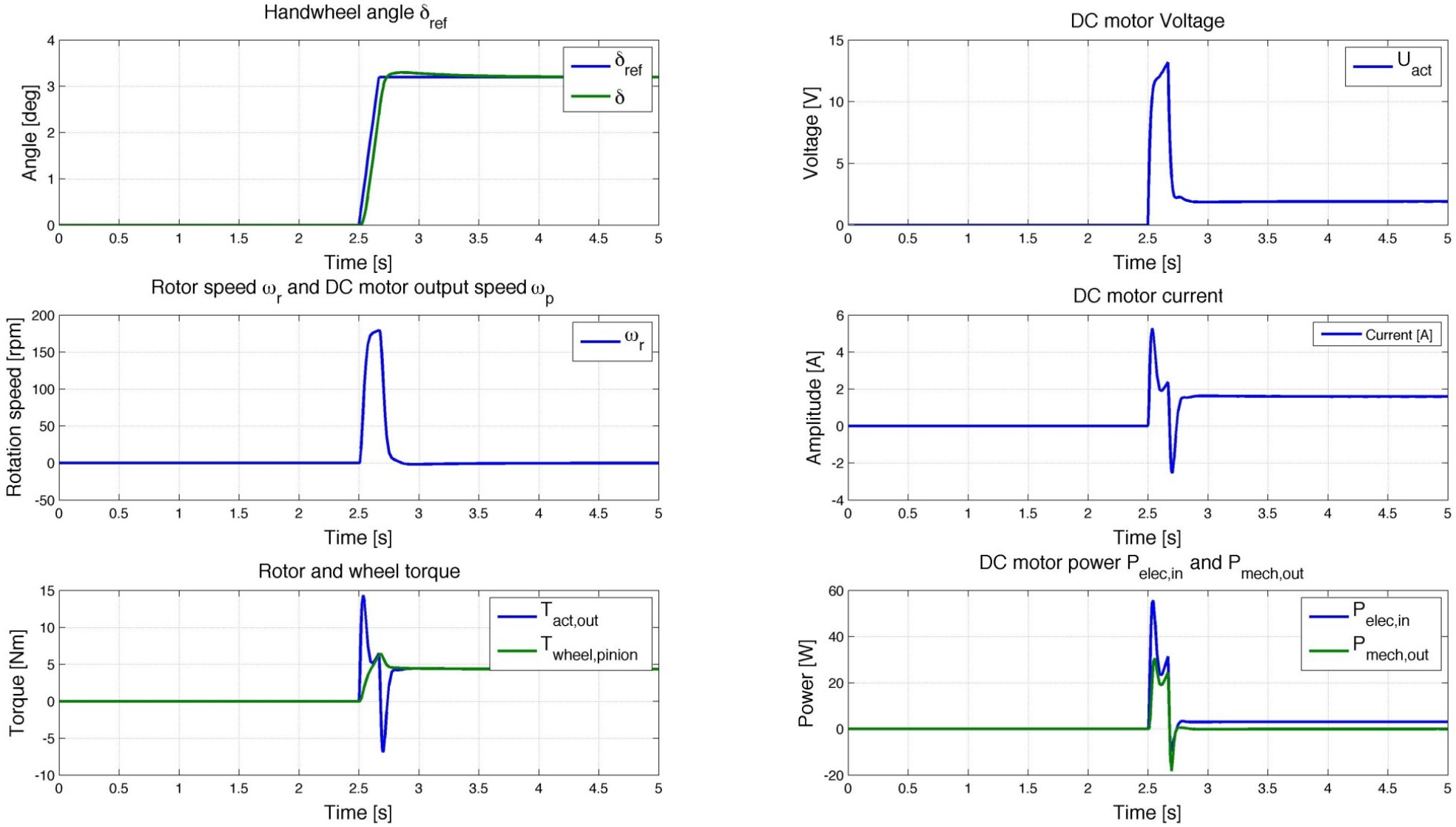

Figure 38. Time response behavior to steering step input $\delta = 3.2\ deg$ ($= \alpha_{max}$ for $e = 20\ mm$) and 0.2 sec rise time

Table 14 shows the evaluation of frequency and time domain analysis for different load case scenarios. It lists the numerical results and the respective peak values estimated for each parameter.

Table 14. Power requirements: Evaluation of frequency and time response

Load case	Torque [Nm]	Rotor speed [rpm]	Voltage [V]	Current [A]	Power [W]
$T_y(e = r_c = 20\ mm)$	30	350	25	10	250
$T_{stat}\ (F_z = 800\ N)$	30	350	25	10	250
$T_z(r_c < 0)$	25	350	25	10	180

If we look now at the frequency response behavior of the vehicle for this specific setup and actuator in Figure 39 we can see that the dynamics and time lag of the vehicle are not crucially affected by the use of a steer-by-wire system. One could also think of some kind of second closed-loop with a yaw rate sensor to improve steering response behavior in comparison to a conventional steered vehicle. The yaw rate response in Figure 39 is based on the steering control behavior in Figure 35.

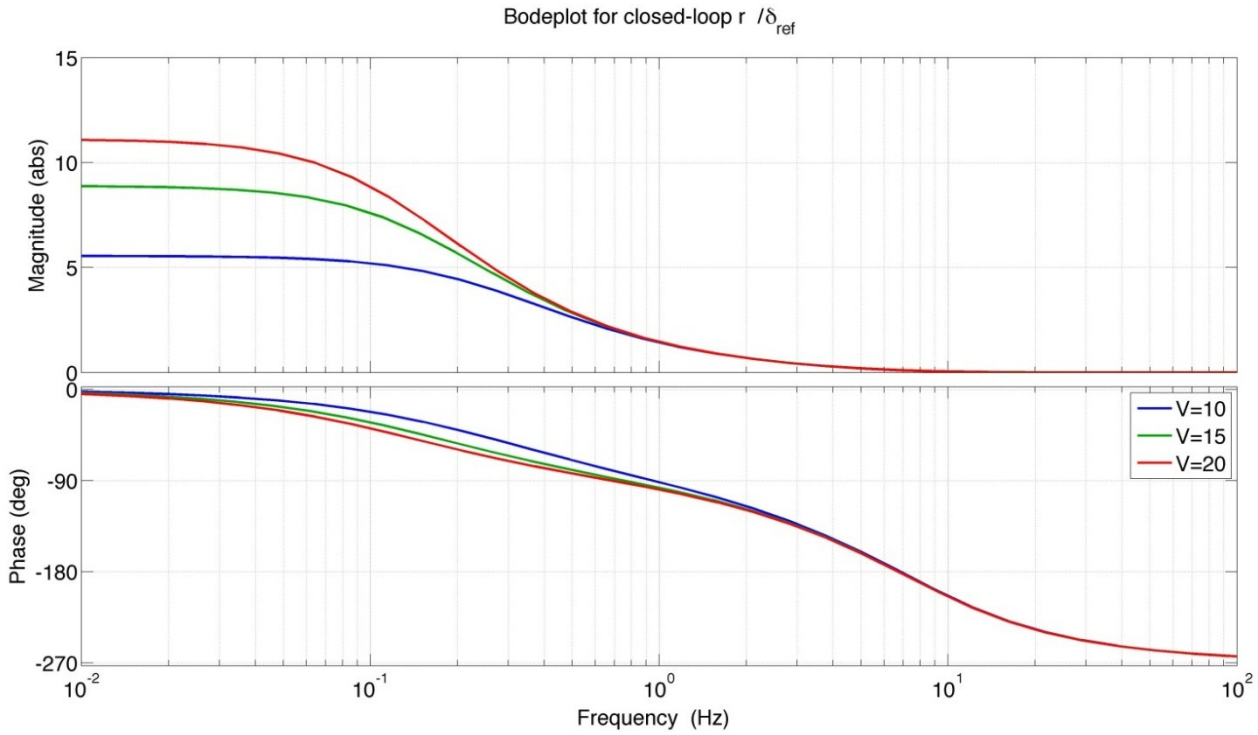

Figure 39. Frequency response behavior of vehicle yaw rate for closed-loop steering control

5.3 Actuator choosing

When searching for suitable actuators one can note fast, that actuators are often only given as "black-box" system with voltage input U and output torque $T_m$and speed ω_r, as mentioned before.

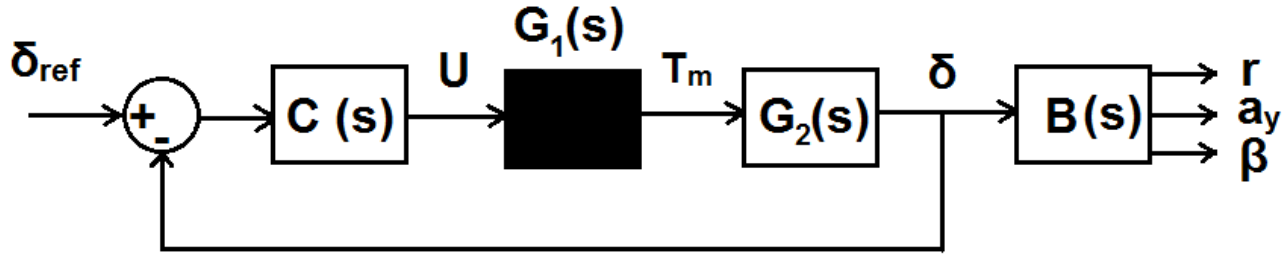

Figure 40. Steer-by-wire control system with unknown actuator transfer function

In order to set power requirements we can set the requirement that the actual steering angle δ equals the intended steering angle δ_{ref} (5-1).

$$\delta = \delta_{ref} = A\sin(\omega t) \quad 5\text{-}1$$

From there the turning velocity $\dot{\delta}$ of the wheels (5-2) and its maximum (5-3) can be defined:

$$\dot{\delta} = A\omega\cos(\omega t) \quad 5\text{-}2$$

$$\left|\dot{\delta}\right|_{max} = |A\omega| \quad 5\text{-}3$$

By using the steering ratio r_s the output speed requirements of the actuator can be defined (5-4).

$$|\omega_r|_{max} = \left|\dot{\delta}\right|_{max} r_s \ [rad/s] \quad 5\text{-}4$$

Table 15 shows the speed requirements for steering ratio of $r_s = 11$.

Table 15. Output speed requirements for actuator

Steer angle velocity	Wheel turn speed[rad/s]	Wheel turn speed[deg/s]	Wheel turn speed [rpm]	Actuator speed [rpm] (rs=11)	Actuator speed[deg/s] (rs=11)
$\left\|\dot{\delta}(5\ deg,\ 1\ Hz)\right\|$	0.55	31	5	55	330
$\left\|\dot{\delta}(10\ deg,\ 2\ Hz)\right\|$	2.2	126	21	231	1386
$\left\|\dot{\delta}(5\ deg,\ 5\ Hz)\right\|$	2.74	157	26	288	1728

Similar considerations can be made on load torque T_m. The wheel torque is described by equation 5-5.

$$T_w(\delta) = K_w\delta + D_w\dot{\delta} + J_w\ddot{\delta} \quad 5\text{-}5$$

Using (5-1) for δ it can be rewritten to (5-6) with the maximum friction torque amplitude $\left|T_{fric,max}\right|$ for steering angle amplitudes $A > 5°$ (5-7).

$$T_w(\omega t) = K_w A\sin(\omega t) + D_w A\omega\cos(\omega t) - J_w A\omega^2\sin(\omega t) \quad 5\text{-}6$$

$$\left|T_{fric,max}\right| = K_w A = 50\ Nm \quad 5\text{-}7$$

$\left|T_{fric,max}\right|$ has been set to the maximum friction torque for the combined braking and steering case, since maximum spin torque $T_{stat} = 88\ Nm$ doesn't fast turning speed and thus, the influence of damping and inertia can be neglected. Lumped damping of the steering system about kingpin axis has been set to $D_w = 225\ [Nms/rad]$ and lumped inertia to $J_w = 5\ [kgm^2]$, as has been explained in section 4.5.

From there, maximum wheel torque $T_{w,max}$ and maximum actuator load torque $T_{m,max}$ can be evaluated. The results are given in Table 16 for sinusoidal driver input with different steering amplitude and frequency.

Table 16. Output torque requirements for actuator

Load case	Wheel Torque [Nm]	Actuator torque [Nm] (rs=25)	Actuator torque [Nm] (rs=16)	Actuator torque [Nm] (rs=11)	Steering rack force [N] (rst=10 mm)
$\left\|\dot{\delta}(30\ deg,\ 0.1\ Hz)\right\|$	88	3.5	5.5	8	880
$\left\|\dot{\delta}(5\ deg,\ 1\ Hz)\right\|$	128	5.1	8	12	500
$\left\|\dot{\delta}(10\ deg,\ 2\ Hz)\right\|$	500	20	32	46	5000
$\left\|\dot{\delta}(5\ deg,\ 5\ Hz)\right\|$	725	29	45	66	7250

In the previous section it could be shown that steering angle step response doesn't show significant torque amplitudes than the sinusoidal response for $f = 2\,Hz$. Thus, the torque requirements in Table 16 can be seen as upper limits. We can see that for great steering angle amplitude $A = 30\,deg.$ and low frequency $f = 0.1\,Hz$ wheel torque equals maximum spin torque amplitude.
For higher frequencies we can see the crucial impact of inertia and damping in the system. As been mentioned before in section 4.5, the precise estimation of inertia and damping can be only accomplished with the ready built EDV. It is recommendable then to identify those parameters experimentally to improve steering control precision.

6 Conclusions

A great deal of importance in this work has been laid on the possibility of adaption of the results to change of parameters. Since by the end of this thesis work the concept of the EDV hadn't been finalized yet, the transferability of results to change in design and components was of crucial importance.

In order to produce trustable results in the analysis for sizing the steering actuator, limiting values in the estimation of unknown parameter had been chosen. This has been accomplished by means of suspension geometry, tire forces and steering dynamics.

The report focusses on the analysis of tire friction forces in relevant driving scenarios and the study of the influence of suspension geometry on steering effort. This could be accomplished in an analytic way. Particular focus in has been laid on the influence of caster trail e and scrub radius r_c on steering effort. The final results are based on the estimation of $e = 20\ mm$ and $r_c = 20\ mm$, which considers already the change of suspension geometry due to vertical wheel motion.

Maximum tire forces have been estimated with respect to physical limitations of the tire. For that purpose a friction coefficient of $\mu = 1.5$ has been assumed throughout this work. This assumption overestimates the actual maximum friction coefficient but serves as a sort of security margin, which means it can be assumed that real tire forces won't be larger than the given results.

Four relevant driving scenarios have been considered as actuator dimensioning driving scenarios, in which maximum steering torque is expected. Those are:

1. Tire spin torque in parking conditions
2. Jacking torque due to high dynamic vertical wheel load
3. Self-aligning torque in high-speed cornering
4. Steering torque for combined braking and steering case during high-speed cornering.

The maximum steering torque due to tire friction of both wheels of the EDV has been identified as $T = 88\ Nm$ for static spin torque.

Tire forces are results of vehicle dynamics. However, in the steering system they have been modelled as static load as function of steering stiffness of steering angle δ about the kingpin axis. Dynamic steering forces due to damping and inertia of the system, necessary to define the actual load torque of the steering system, haven't been analysed in this work, but estimated from reference works ([4], [14], [15]).

For damping of steering rate $\dot{\delta}$ the lumped damping coefficient $D_w = 225\ [Nms/rad]$ about the kingpin axis has been used. For the steering system's inertia about the kingpin axis $J_w = 225\ [Nms/rad]$ has been used. Those two parameters strongly depend on the components of the steering system, such as steering rack and pinion, steering knuckles, tire types. Since they strongly influence the amplitude of steering torque during fast steering motion, it is highly recommended to identify those parameters experimentally for the finalized EDV.

Steering control analysis showed that electro-dynamics of the actuator are of particular importance and analysing of the overall closed-loop response behaviour is necessary to guarantee sufficient control time and precision.

However, this can be particular difficult, since a lot of manufacturers provide their actuators as black-box systems only with information about input voltage and output torque or speed. For that reason power requirements for the steering actuator have been in terms of dynamic load torque, which is a function of steering angle frequency and amplitude, as well as steering ratio r_s. The latter one can be specifically used to adjust the steering system to the actuator characteristic. Since a steer-by-wire

doesn't set requirements to steering ratio it can be set according to the needs, which means that it can either used for decreasing the torque requirements or to increase the speed of steering motion.

With limits of steering angle amplitude $|\delta_{max}| = 10\ deg.$, steer frequency $f_{max}(\delta) = 2\ Hz$ and steering ratio $r_s = 11$ rough performance requirements for the steering actuator have been set to:

1. Actuator output torque $T_{m,max} = 50\ Nm$
2. Actuator output speed $\omega_{m,max} = 230\ rpm$
3. Actuator output power $P_{m,max} = 1.2\ kW$

As proposed in the beginning, the steer-by-wire system can be also accomplished by a setup with linear steering actuator. In this case, the driver steer angle input δ_{ref} is directly transferred into a linear motion, which sets the wheel steering angle δ. For this setup the performance requirements can be set to (assuming steering radius on upright $r_{st} = 10\ mm$):

1. Actuator output force $F_{m,max} = 5\ kN$
2. Actuator output speed $v_{m,max} = 240\ mm/s$
3. Actuator output power $P_{m,max} = 1.2\ kW$

The estimation of energy demand for the actuator has not been done yet at this point since it strongly depends on the final steering system design. For this purpose, it would be also necessary to develop a standardized steering profile for city driving, high-way driving, etc. However, it can be stated at this point, that one of the big advantages of electronic powered steering is, that it can be designed in such a way, that energy is only required during steering motion. Energy for the steering system is not required for $\delta = 0$ [14].

June 2013

7 References

[1] E. Vijayakumar, ”Thesis work: Frame stiffness and mass estimation analysis for electric one-seater prototype,” Volvo Group Truck Technology, Göteborg, Sweden, 2013.

[2] P. H. Winner, Fahrdynamik und Fahrkomfort, Darmstadt: FZD TU Darmstadt, 2011.

[3] N. D. Smith, ”Understanding Parameters Influencing Tire Modeling,” Colorado State University, 2004 Formula SAE Platform, 2004.

[4] P. Yih, "Steer-by-wire: Implications for vehicle handling and safety (Dissertation PhD)," Stanford University, San Francisco, CA, Januar 2005.

[5] T. Rattfelt, ”Thesis work: Preparatory Component Selection for Design of Prototype Electric One-Seater Car,” Volvo Group Truck Technology, Göteborg, 2013.

[6] DIN, ”DIN 70020-1,” DIN, Germany.

[7] Y. G. CHO, "Vehicle steering returnability with maximum steering angle at low speeds," *International Journal of Automotive Technology,* p. 431−439, Vol. 10, No. 4, 2009.

[8] G. Rill, ”First order tire dynamics,” i *III. European Conference on Computational Mechanics*, Lisbon, Portugal, 2006.

[9] R. g. R.s. Sharp, "On car steering torques at parking speeds," *Part D: Journal of Automobile Engineering,* pp. 87-96, 2003.

[10] H. B. Pacejka, Tyre and Vehicle Dynamics, Second Edition, Rotterdam: Butterworth-Heinemann, Oxford, 2006.

[11] A. Tires, ”avonracing.com,” Avon Tires, [Online]. Available: http://www.avonracing.com. [Använd 04 2013].

[12] R. M. Brach, ”Modeling Combined Braking and Steering Tire Forces,” *SAE TECHNICAL PAPER SERIES,* Vol. %1 av %22000-01-0357, 2000.

[13] P. D.-I. R.Nordmann, Mechatronische System im Maschinenbau I, Darmstadt, Germany: TU Darmstadt, 2005.

[14] M. Mitschke, Dynamik der Kraftfahrzeuge, Band B, Schwingungen, Heidelberg: Springer Verlag Heidelberg, 1984.

[15] M. N. P. R. Li LIU, ”On Torque Control of Vehicle Handling and Steering Feel for Avoidance Maneuver with Electric Power Steering,” i *17th World Congress The International Federation of Automatic Control*, Seoul, Korea, 2008.

[16] B.-C. J. a. S.-C. L. Du-Yeol Pang, ”Steering Wheel Torque Control of Electric Power Steering by PD-Control,” i *KINTEX*, Gyeonggi-Do, Korea, 2005.

APPENDIX A Vertical dynamics analysis

A standard model used in vertical dynamics is the *Quarter-Car-Model* (Figure 41), which is given by a 2 DOF two-mass oscillator representing the vertical model of a single wheel. In Figure 41 the two masses are given by the unsprung mass m_W, which is mainly given by the wheel mass, and the sprung mass m_B, the partial body mass loaded on that wheel. c_w and d_w represented stiffness and damping values of the tire and c_B and d_B those of the suspension.

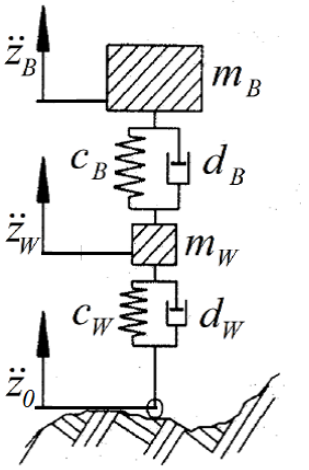

Figure 41. Quarter-Car-Model

The values c_w and d_w are values given by the type of tire chosen. The vertical dynamics analysis using a quarter-car-model can be used to get a first estimation for stiffness and damping adjustment c_B and d_B of front and rear suspension. Purpose of the suspension system is on the one hand to provide road holding at all time and on the other hand to reduce vibrations on car and passenger coming from the road. A 2 DOF system shows two critical Eigen frequencies. Those are the frequencies, at which it comes to resonance, meaning that the impact of road disturbance is the greatest.

$$\begin{bmatrix} m_w & 0 \\ 0 & m_b \end{bmatrix} \begin{bmatrix} \ddot{z}_w \\ \ddot{z}_b \end{bmatrix} + \begin{bmatrix} d_w + d_b & -d_b \\ -d_b & d_b \end{bmatrix} \begin{bmatrix} \dot{z}_w \\ \dot{z}_b \end{bmatrix} + \begin{bmatrix} c_w + c_b & -c_b \\ -c_b & c_b \end{bmatrix} \begin{bmatrix} z_w \\ z_b \end{bmatrix} = \begin{bmatrix} z_0 c_w + \dot{z}_0 d_w \\ 0 \end{bmatrix}$$

$$\Leftrightarrow \; M\ddot{z} + D\dot{z} + Cz = f \qquad 7\text{-}1$$

Equation 7-1 shows the representation of the quarter-car-model. The sprung mass m_B and the unsprung mass m_W are not completely separable. For example, the components of suspension are partly sprung and unsprung. For precise definition of both masses, measurements would be necessary. In most cases, counting half of the connection components (such as wishbones, A-arms, etc.) to sprung and half of it to unsprung mass, is a good approximation.

$$u(x) = \begin{cases} \hat{u}(1 - cos(\frac{2\pi x}{l})), & \text{for } 0 < l < x \\ 0, & \text{else} \end{cases} \qquad 7\text{-}2$$

$$vT = l \Rightarrow \; T = \frac{l}{v};\; \Omega = \frac{2\pi}{T} = \frac{2\pi}{x} l \qquad 7\text{-}3$$

$$u(t) = \hat{u}(1 - cos(\Omega t)) \; for \; 0 \le t \le T \qquad 7\text{-}4$$

Equation 7-4 and Figure 43 show a way to model the road input z_0. As can be seen from Equation 7-3 and Figure 42, is the frequency of the road input z_0 a function of car velocity v and wave length l. We can see that the road input frequency ω_{z0} coincides with the critical Eigenfrequencies of wheel and body at $l = 1\,m$ and $l = 10\,m$ for a car velocity of $v = 36\,km/h$. Thus, the stiffness and damping coefficient of the suspension have to be chosen such that they reduce the vertical movement and acceleration at those critical frequencies. However, the stiffness value c_B also affects the critical Eigenfrequency of the body due to the relation given in equation 7-5.

$$f_{crit,body} = \frac{1}{2\pi}\sqrt{\frac{c_B}{m_b + m_{load}}} \qquad 7\text{-}5$$

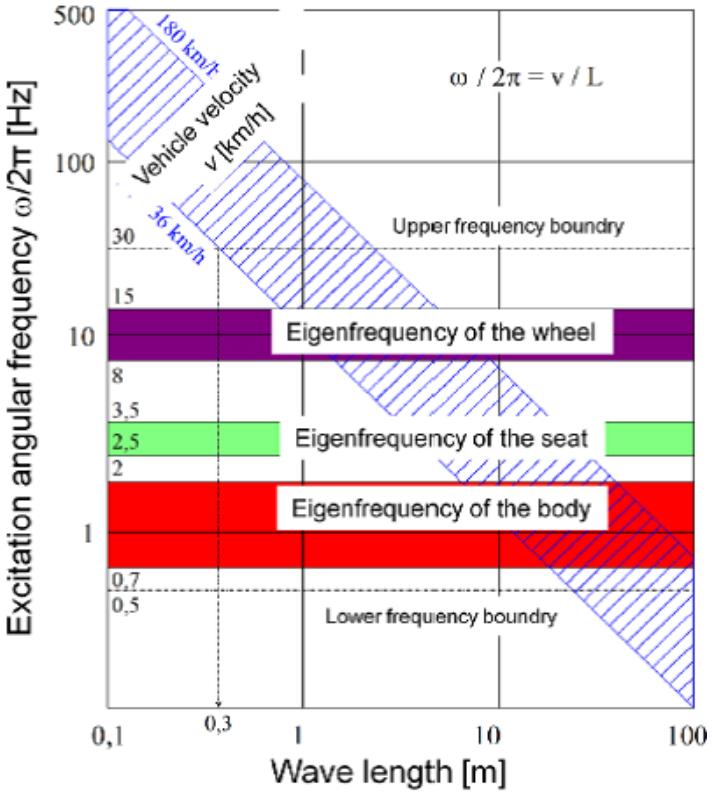

Figure 42. Excitation frequency of road input z_0, [2]

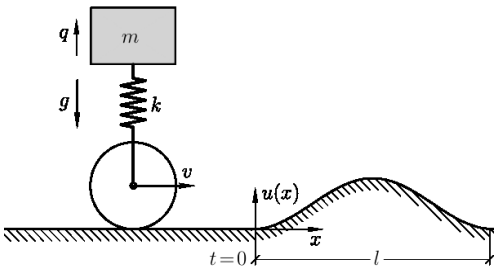

Figure 43. Road bump model [7]

One difficulty is given for road puts with discontinuous characteristics, such as an impulse or step. In this case, the frequency input is almost distributed over the whole range of frequencies, which can cause disastrous failure. Since an ideal impulse doesn't exist in reality, it will always have certain continuity in the excitation and only road inputs with $\frac{dz_0}{dt} < \infty$ will be considered. Nevertheless, it has been taken into account that the frequencies of road irregularities can spread over a wide range of frequencies.

The assessment of the body acceleration $\ddot{z}_b$ and the wheel load F_Z gives good information about ride comfort and endurance strength of the car. Figure 44 shows that an increase of the unsprung mass m_W lowers the second resonance frequency, but on the other side increases the wheel load F_z(and accelerations) and the frequency spectrum becomes wider [2].

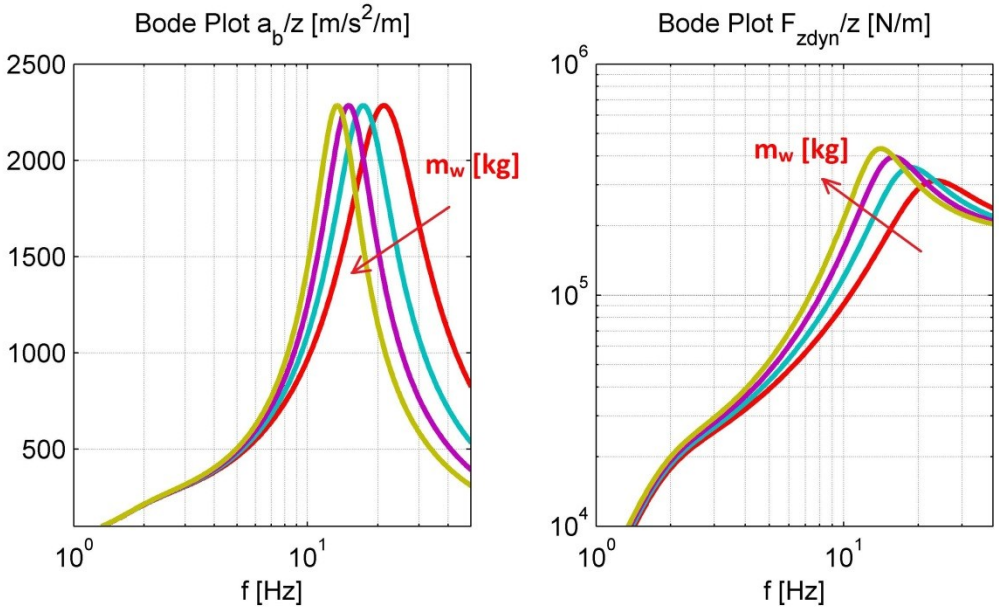

Figure 44. Influence of the unsprung mass m_w [14]

However, in Figure 45 it is possible to see that an increase of the body mass m_B certainly affects the first resonance, the body frequency, but also lowers body acceleration in the second resonance, while the wheel load remains unchanged.

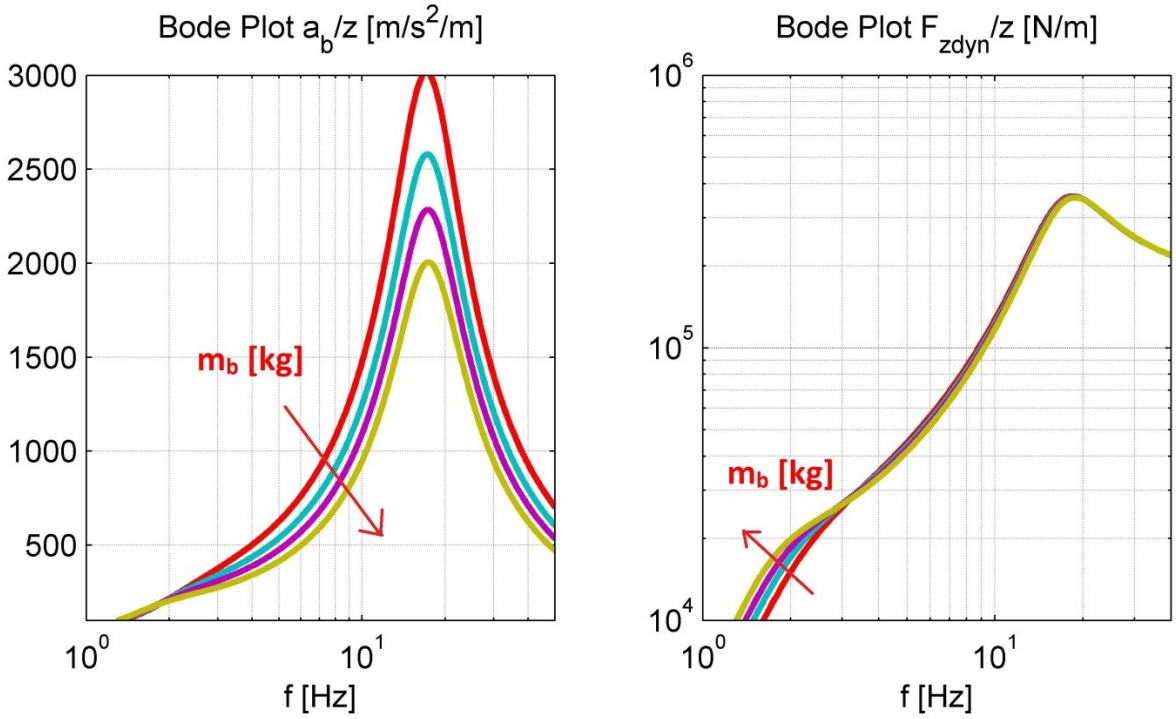

Figure 45. Influence of body mass m_B [14]

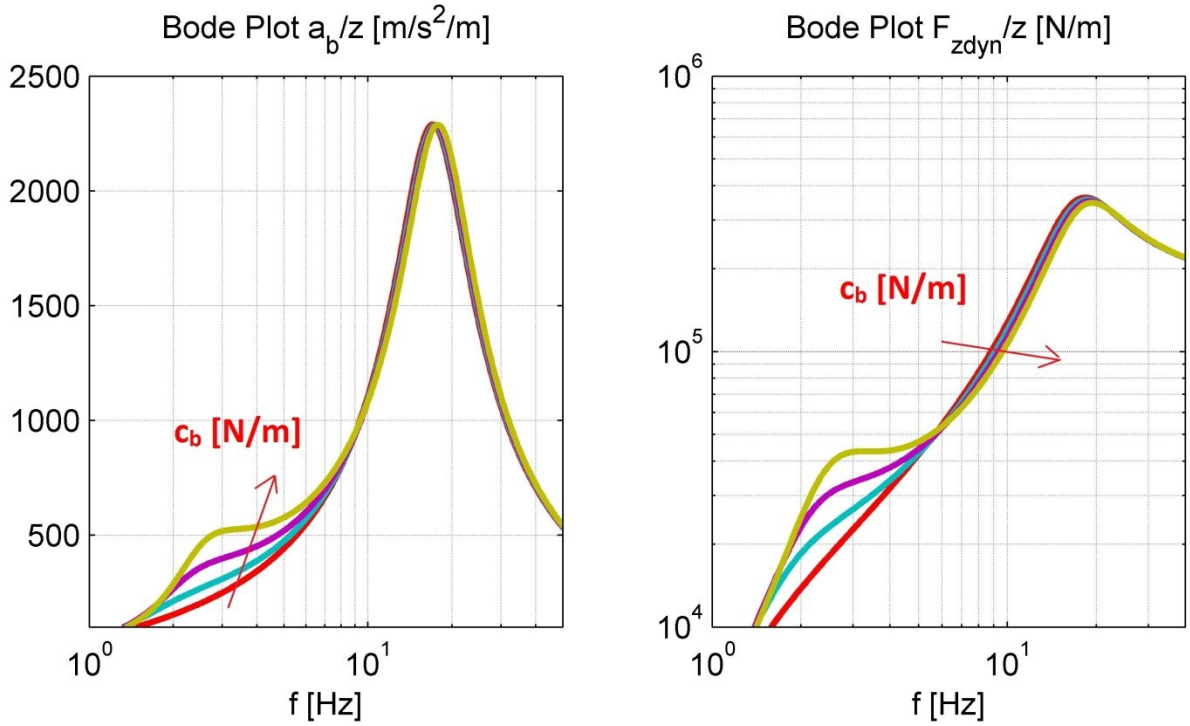

Figure 46. Influence of body stiffness c_B [14]

Since the body stiffness c_B is connected to both, the sprung and the unsprung mass, it affects both resonances, and an increase of the stiffness has positive effects on the wheel load, as can be seen in Figure 46.

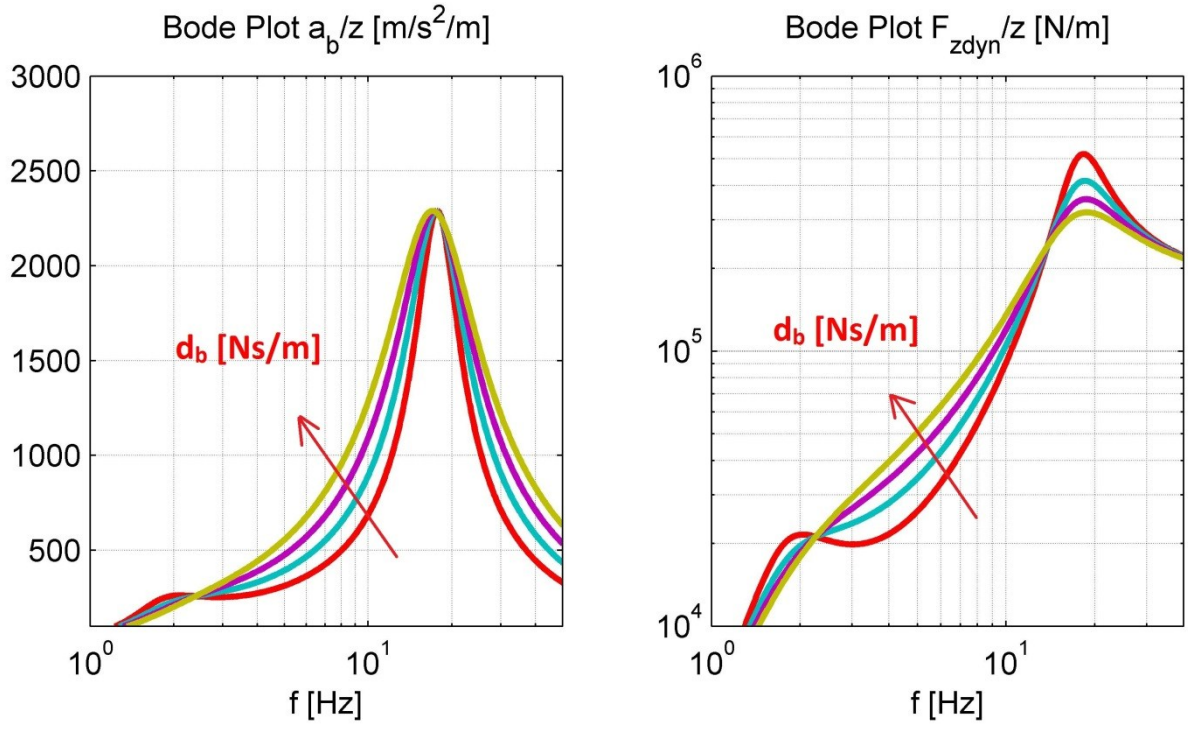

Figure 47. Influence of body damping d_B [14]

Figure 47 shows that the body damping d_B lowers the peaks of the resonances, whereas it has negative effects on the overcritical regions.

The given graphs are showing that, when adjusting the parameters, a compromise between ride comfort (weighted vibration intensity K_{seat}) and driving safety (normalized wheel load fluctuation) has to be found. This can be drawn in a conflict diagram (Figure 48), in which both criteria are laid on top of each other. In one case the damping is changed while the stiffness is kept constant and the other way around. There is a physical boundary curve, which can't be undercut. In the adjustment progress of the solar project the focus will be more on the driving safety than ride comfort. Nevertheless, it has to be guaranteed that there will be no physical damage to the driver [14].

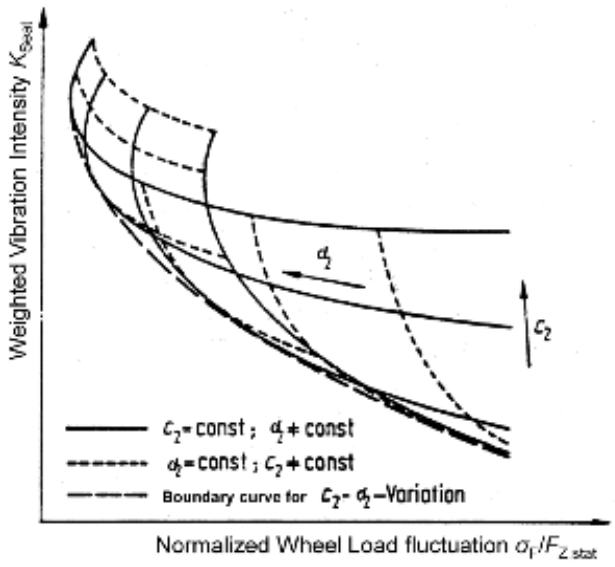

Figure 48. Conflict diagram suspension adjustment [2]

APPENDIX B Spin torque and relaxation length

Due to the elasticity of the tire, lateral forces will not directly build up, but take a certain time. G. Rill [8] presents a model to describe those dynamics tire forces F_y^D as a first-order system (3-1).

$$\underbrace{F_y(v_y + \dot{y}_e)}_{F_y^D} \approx \underbrace{F_y(v_y)}_{F_y^S} + \frac{\partial F_y}{\partial v_y}\dot{y}_e \tag{7-6}$$

$$\frac{\partial F_y}{\partial v_y} = \frac{\partial F_y}{\partial s_y}\cdot\frac{\partial s_y}{\partial v_y} = \frac{\partial F_y}{\partial s_y}\cdot\frac{-1}{r_D|\Omega|} \tag{7-7}$$

$$s_y = \frac{-v_y}{r_D|\Omega|} \qquad \alpha = \arctan s_y \tag{7-8}$$

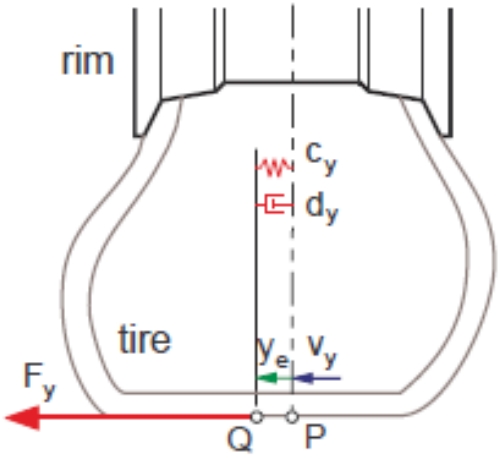

Figure 49. *Lateral tire deflection* [8]

With lateral stiffness c_y and the lateral damping property of the tire d_y the dynamic tire force can be written as function of lateral deflection y_e (7-9). Combined with 3-1 and 3-3 relaxation time constant τ_y (7-11) can be derived and from there relaxation length r_y (7-12). Those two sizes describe the time and distance necessary until a change of slip conditions leads to a steady-state force amplitude as a function of rotation speed Ω of the wheel.

$$F_y^D = c_y y_e + d_y \dot{y}_e \tag{7-9}$$

$$F_y^S + \frac{\partial F_y}{\partial s_y}\cdot\frac{-1}{r_D|\Omega|}\dot{y}_e = c_y y_e + d_y \dot{y}_e \tag{7-10}$$

$$\underbrace{\frac{1}{c_y}\left(d_y + \frac{\partial F_y}{\partial s_y}\cdot\frac{1}{r_D|\Omega|}\right)}_{\tau_y}\dot{y}_e + y_e = \frac{F_y^S}{c_y} \tag{7-11}$$

$$r_y = r_D|\Omega|\tau_y = r_D|\Omega|\frac{1}{c_y}\left(d_y + \frac{\partial F_y}{\partial s_y}\cdot\frac{1}{r_D|\Omega|}\right) = r_D|\Omega|\frac{d_y}{c_y} + \frac{1}{c_y}\frac{\partial F_y}{\partial s_y} \tag{7-12}$$

The force equilibrium in point Q in Figure 14. Lateral tire deflection is then given by

$$F_y = C_{F\alpha}\alpha + D_{F\alpha}\dot{\alpha} = c_y y_e + \left(d_y + \frac{\partial F_y}{\partial s_y} \cdot \frac{1}{r_D|\Omega|}\right)\dot{y}_e \qquad \text{7-13}$$

APPENDIX C Vertical load shift

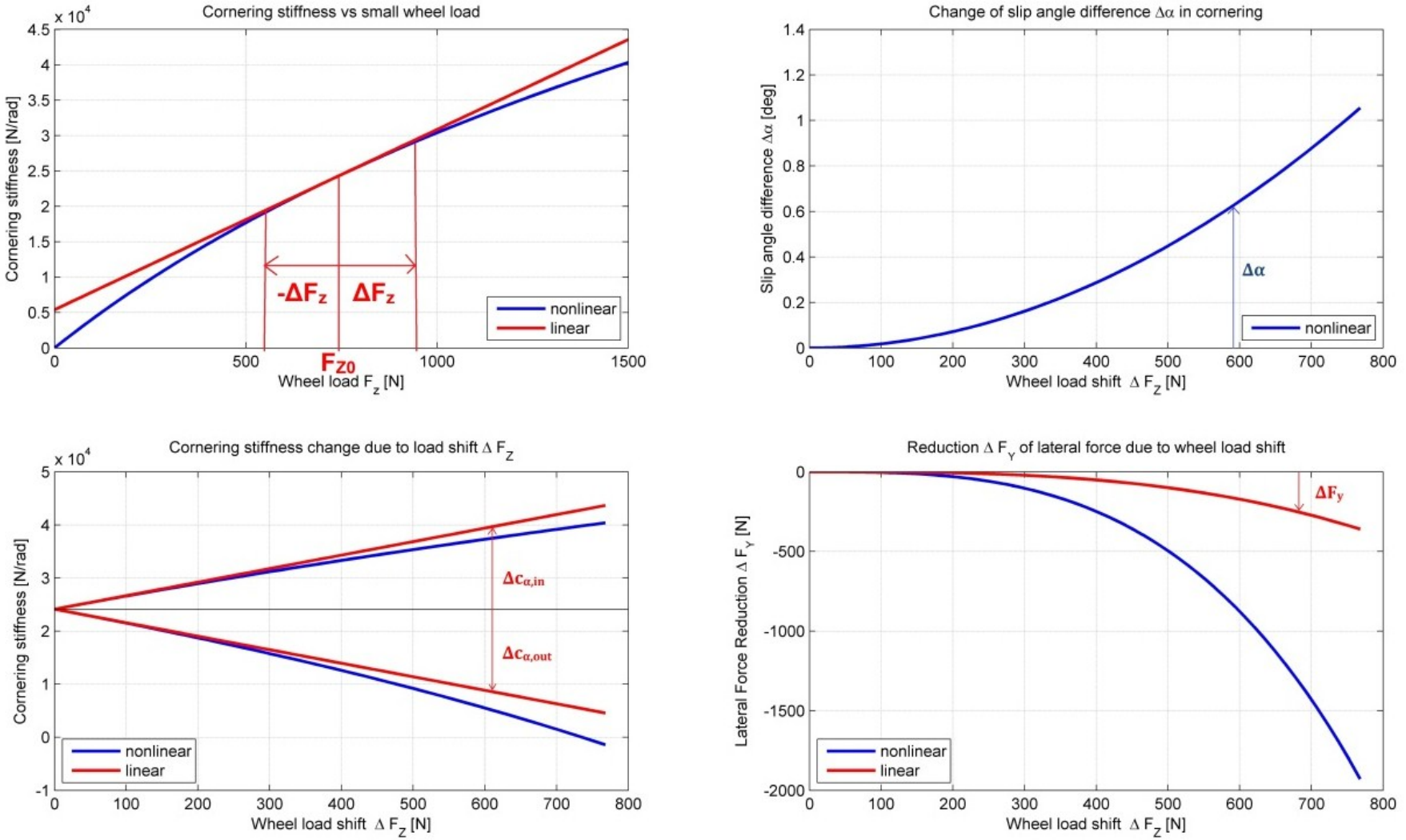

Figure 50. Effects of vertical load shift

APPENDIX D Tire properties

Project:	**RC353STB**		**Size:**	**7.0/20.0-13**		**Camber:**	**1°**
Spec:	**10998**		**Tyre:**	**3 ply Pro Series**		**Pressure:**	**26 P.S.I.**
Tested:	**31/07/01**		**Rim:**	**6 x 13**		**Speed:**	**20 KPH**

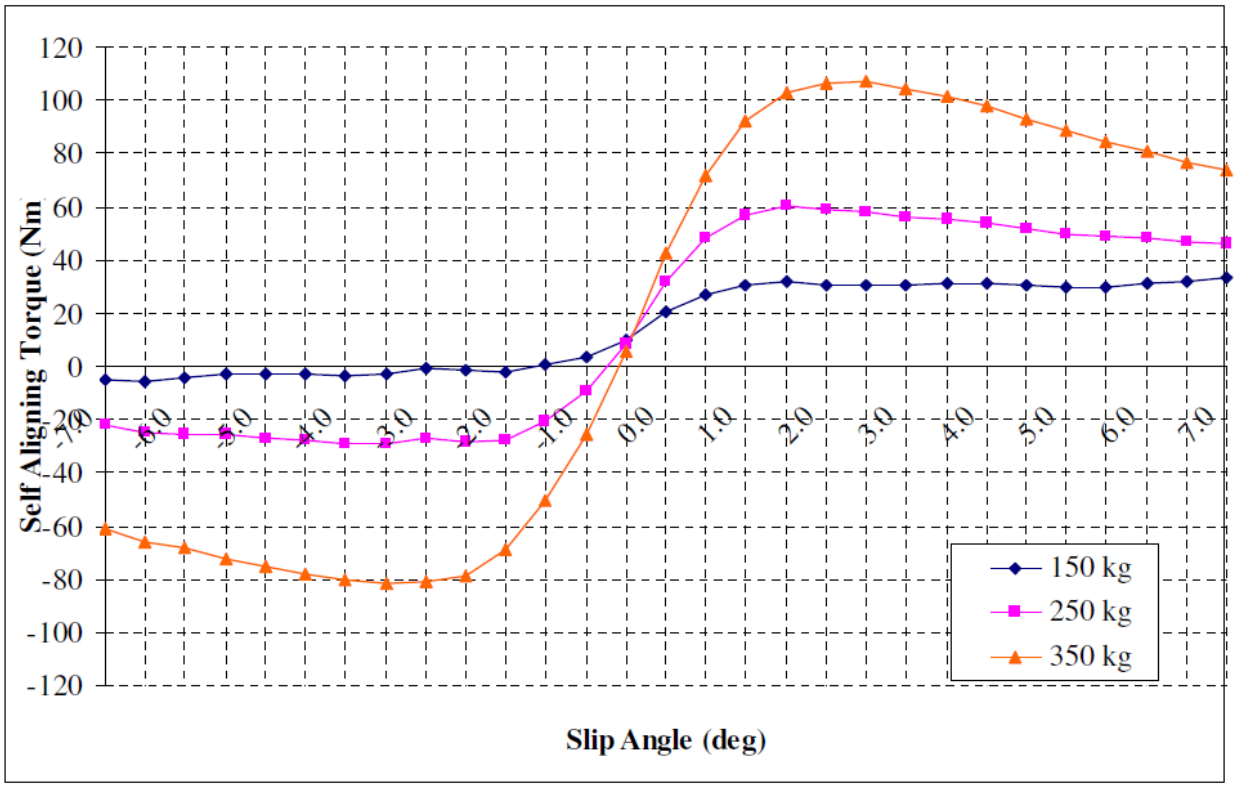

Figure 51. Self-aligning torque vs. slip-angle, from [11]

APPENDIX E Steering control analysis

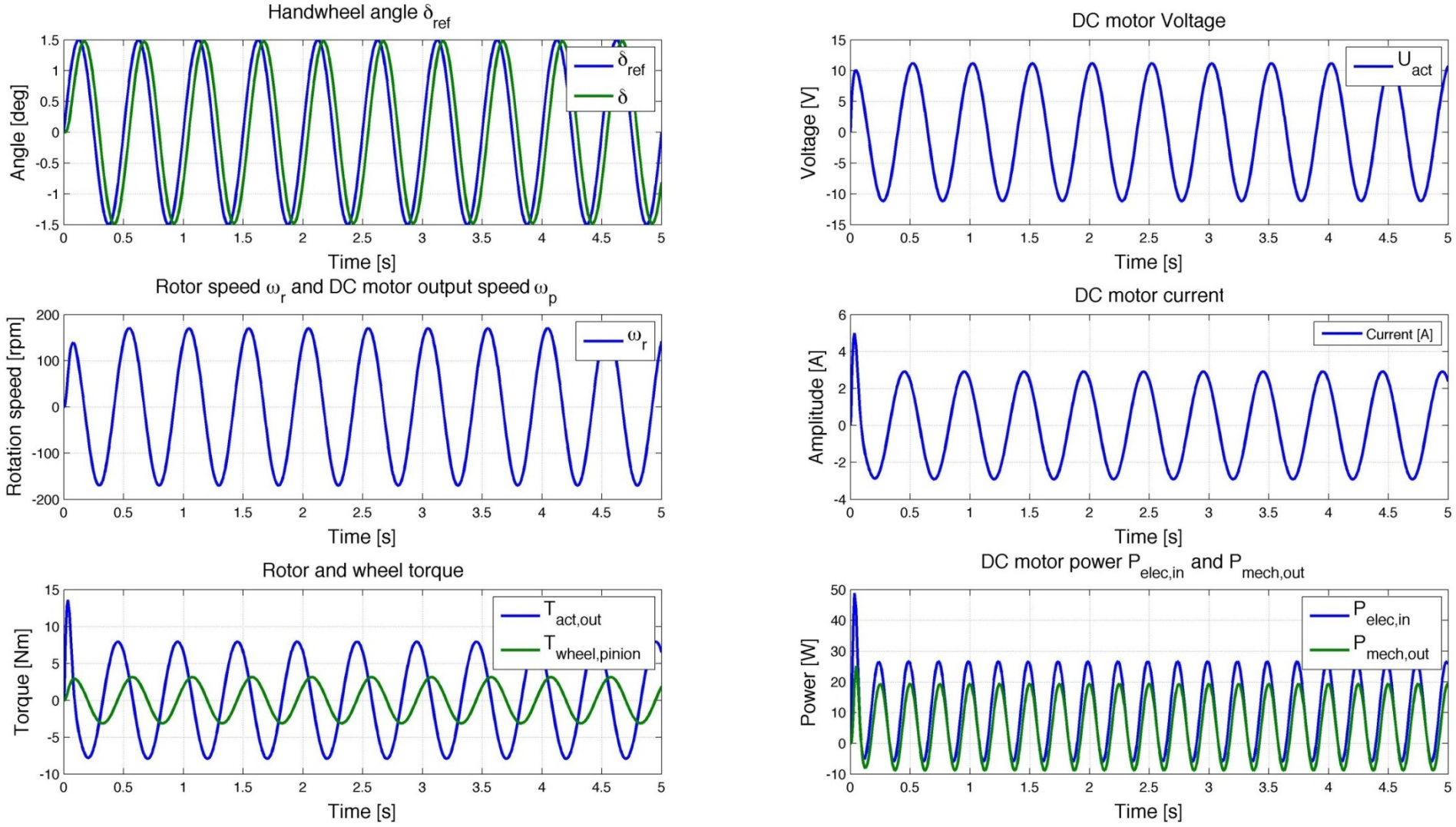

Figure 52. Time response for $f = 2\ Hz$ and $e = 0\ mm$

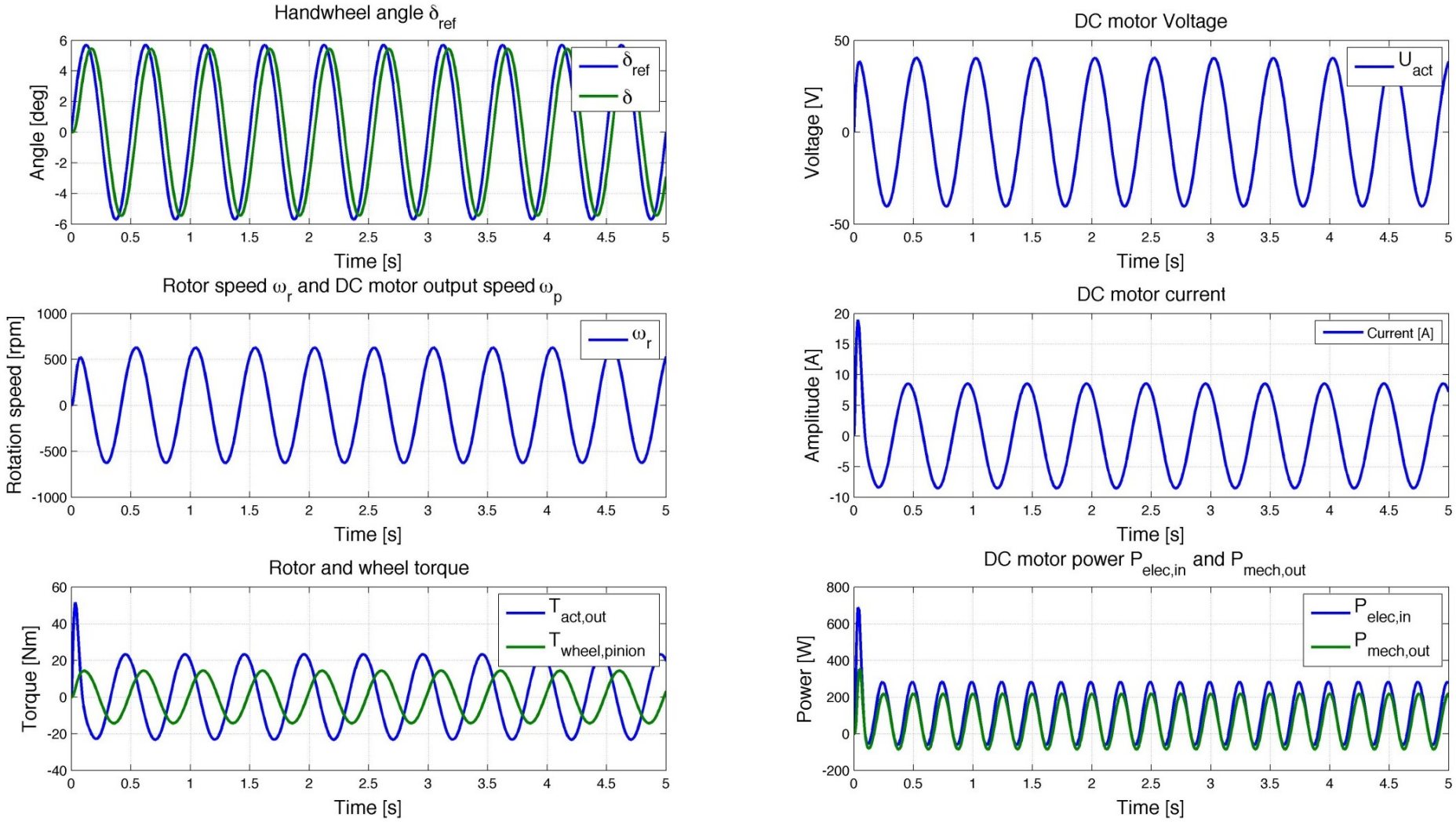

Figure 53. Time response for $f = 2\ Hz$ and $e = 50\ mm$

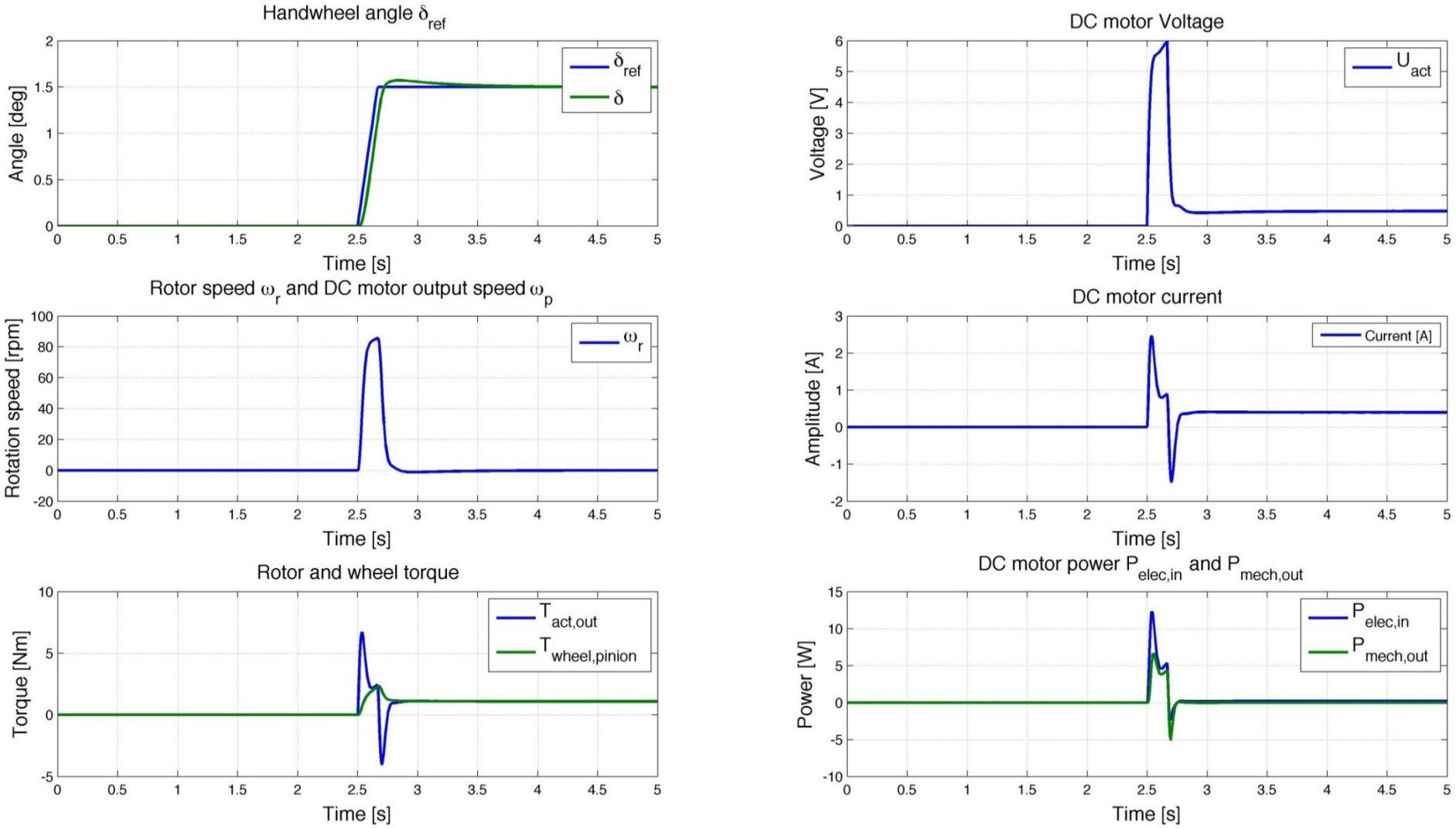

Figure 54. Time response behavior to steering step input $\delta = 1.5\ deg.\ (e = 0\ mm)$ and 0.1 sec rise time

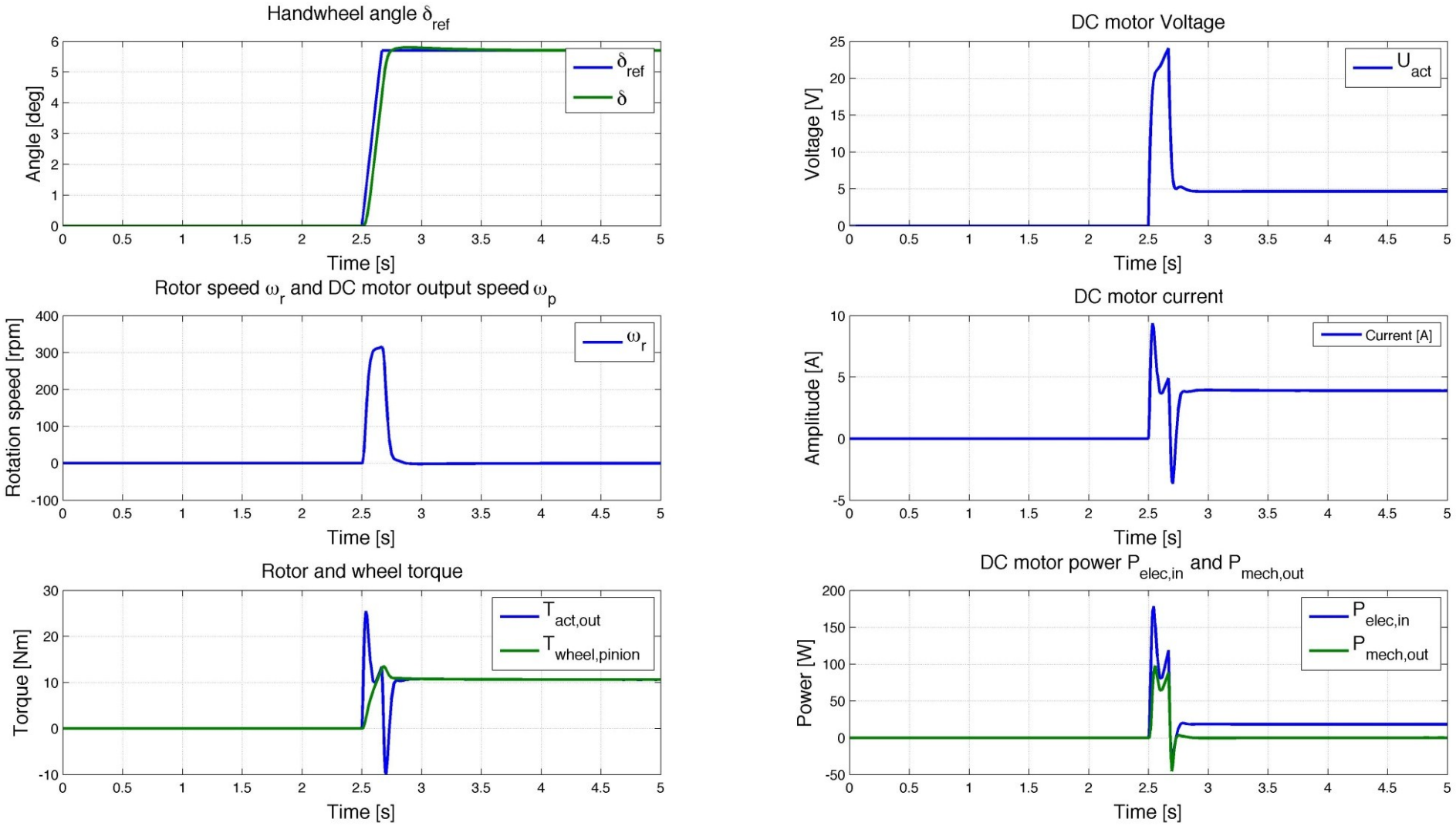

Figure 55. Time response behavior to steering step input $\delta = 6\ deg.\ (e = 50\ mm)$ and 0.1 sec rise time